UNIVERSITAT POLITÈCNICA DE CATALUNYA
BARCELONATECH

Department of Signal Theory and Comunications

Ph.D. Dissertation

Exponentiated Weibull Fading Channel Model in Free-Space Optical Communications under Atmospheric Turbulence

Ricardo Barrios, M.Sc.

Supervised by:
Dr. Federico Dios

Submitted in partial fulfillment of the requirements for the degree of Doctor of Philosophy.

Barcelona, Spain
April 2013

Printed in Barcelona, Spain.

Exponentiated Weibull Fading Channel Model in Free-Space Optical Communications under Atmospheric Turbulence, Ricardo Barrios, Ph.D. Dissertation, Departament de Teoria del Senyal i Comunicacions, Universitat Politècnica de Catalunya. Barcelona, Spain.

This work has been founded by the Spanish Ministry of Science and Innovation under FPI grant BES-2008-003684 and projects TEC2006-12722 and TEC2009-10025.

Cover image: all-free-download.com/
Cover design: Ricardo Barrios.

To those four women in my life.

".... For in this world, time has three dimensions, ... Each future moves in a different direction of time. Each future is real. At every point of decision, whether to visit a woman in Fribourg or to buy a new coat, the world splits into three different worlds, each with the same people but with different fates for those people. In time, there are an infinity of worlds.

.... In such a world, how could one be responsible for his actions? Others hold that each decision must be considered and committed to, that without commitment there is chaos. Such people are content to live in contradictory worlds, so long as they know the reason for each."

Excerpt from
Einstein's Dreams
by *Alan Lightman*

Preface

FREE-SPACE OPTICAL (FSO) communications is drawing increasing attention as a promising technology to overcome bandwidth shortage, of an evermore crowded wireless marketplace. Currently radio-frequency (RF) technology struggles to cope with the ever increasing demand for high-bandwidth data. Moreover, as the number of users increases, the RF spectrum is getting so crowded that there is virtually no room for new wireless services, with the additional inconvenient of limited bandwidth restriction for using a RF band and the license fees that have to be paid for such bands. FSO communications offer clear advantages over other alternatives such as narrower and more secure beams, virtually limitless bandwidth and no regulatory policies for using optical frequencies and bandwidth. Moreover, in the space sector FSO technology is becoming more attractive for satellite communication systems due to the less mass and power requirements—compared to RF.

The major drawback for deploying wireless links based on FSO technology is the perturbation of the optical wave as it propagates through the turbulent atmosphere. Many effects are produced, of which the most noticeable is the random fluctuations of the signal-carrying laser beam irradiance (intensity), phenomenon known as *scintillation* and quantified by the scintillation index (SI). The statistical analysis of the random irradiance fluctuations in FSO links is conducted through the probability density function (PDF), from which one can obtain other statistical tools to measure link performance such as the probability of fade and the bit error-rate (BER). Nowadays, the most widespread models for the irradiance data are, by far, the Lognormal (LN) and Gamma-Gamma (GG) distributions. Although both models comply with actual data in most scenarios neither of them is capable of fitting the irradiance data under all conditions of atmospheric turbulence for finite receiving aperture sizes, i.e. in the presence of aperture averaging. Furthermore, there are several cases where neither the LN or the GG model seem to accurately fit the irradiance data, specially in the left tail of the PDF.

The work presented here is devoted to propose a new model for the irradiance fluctuations in FSO links under atmospheric turbulence, in the presence of aperture averaging; resulting in the exponentiated Weibull (EW) distribution. A physical justification for the appearance of the new model is provided along with numerous test scenarios in the weak-to-strong turbulence regime—including numerical simulations and experimental data—to assess its suitability to model the irradiance data in terms of the PDF and probability of fade. Here, a semi-heuristic approach is used to find a set of equations relating the EW parameters directly to the SI. Such expressions were tested offering a fairly good fitting the actual PDF of irradiance data. Furthermore,

for all the scenarios tested a best fit version of the EW PDF is obtained and always presents itself as an excellent fit to the PDF data. The new model has been compared to the LN and GG distributions proving to cope to the predictions made by those and, in some cases, even outperforming their predictions. Additionally, a new closed-form expression has been derived for estimating the BER performance under EW turbulence, for intensity-modulation/direct-detection (IM/DD) systems using on-off keying (OOK) modulation. Moreover, this expression has been extended to include pointing errors. Finally, the exponentiated Weibull PDF has been proved to be valid with fully and partially coherent beams.

The results presented here suggest that the EW distribution presents the better fit for data under different scenarios, thus, the exponentiated Weibull distribution becomes an excellent alternative to model the PDF of irradiance data under all conditions of atmospheric turbulence in the presence of aperture averaging.

Contents

List of Figures

Page

Chapter 1

Chapter 2

Chapter 3

Chapter 4

Chapter 5

Acronyms

APD	avalanche photodiode
BER	bit error-rate
CDF	cumulative distribution function
DPIM	digital pulse interval modulation
DPPM	differential pulse position modulation
EW	exponentiated Weibull
FCB	fully coherent beam
FFT	fast Fourier-transform
FOV	field of view
FSO	free-space optics (optical)
GG	gamma-gamma
GOF	goodness-of-fit
GSM	Gaussian Schell-model
i.i.d.	independent and identically distributed
IM/DD	intensity-modulation with direct-detection
ISI	intersymbol interference
IPPM	improved pulse position modulation
LN	lognormal
MPPM	multipulse pulse position modulation
MSE	mean squared error
OOK	on-off keying
OPPM	overlapping pulse position modulation

PCB	partially coherent beam
PDF	probability density function
PIN	positive-intrinsic-negative photodiode
PPM	pulse position modulation
PWE	word error-probability
RMSE	root-mean-squared error
rRMSE	relative root-mean-squared error
RV	random variable
SI	scintillation index
SLM	spatial light modulator
WOC	wireless optical communications

Symbols & Notations

A	aperture averaging
A_0	fraction of collected power at optical axis for misalignment fading
a	receiver aperture radius
B	bandwidth
C_n^2	refractive-index structure parameter
D	receiver aperture diameter
D_T	transmitter aperture diameter
$E[x]$	expected value of x
$\mathrm{erf}(x)$	error function
$\mathrm{erfc}(x)$	complementary error function
$\mathscr{F}\{\cdot\}$	Fourier transform operator
${}_pF_q$	generalized hypergeometric function
F_0	phase front radius of curvature of a Gaussian beam at plane $z = 0$
F_T	fade threshold parameter
$F_X(x)$	cumulative distribution function of variate X
$f_X(x)$	probability density function of variate X
$G_{p,q}^{m,n}[\cdot]$	Meijer's G-function
h	global channel induced fading
h_a	atmospheric turbulence induced fading
h_ℓ	atmospheric path loss induced fading
h_p	misalignment induced fading
I	irradiance

i	unit imaginary number
$K_\nu(x)$	Macdonald function of order ν
k	scalar wave number
L	propagation path length
L_0	outer scale of turbulence
l_0	inner scale of turbulence
l_c	coherence length of a partially coherent phase screen
N_0	noise power
n	index of refraction
P_b	bit error-probability
P_{fa}	fade probability
$Q(x)$	Gaussian Q-function
$\Re\{\cdot\}$	real part of a complex number
R	receiver responsivity
R_b	bit rate
r_0	Fried's parameter
r_c	beam centroid displacement
Ts	slot time
T_{sym}	symbol time
W_0	Gaussian beam radius at plane $z = 0$
W_B	Gaussian beam waist
W_L	Gaussian beam radius at plane $z = L$
W_{Leq}	equivalent beam radius for pointing errors
W_{LT}	long term beam radius
W_{ST}	short term beam radius
W_G	Gaussian lens radius
α	shape parameter for the GG and EW distributions
β	shape parameter for the GG and EW distributions
β_0^2	Rytov variance for a spherical wave

$\Gamma(x)$	gamma function
$\Gamma(a, x)$	upper incomplete gamma function
$\gamma(a, x)$	lower incomplete gamma function
Δx	sample interval along x dimension
$\delta(x)$	Dirac delta function
ζ	global coherence parameter
ζ_S	source coherence parameter
η	scale parameter for the EW distribution
θ	beam divergence
θ_s	random phase screen
Θ	curvature parameter of a Gaussian beam at receiver
κ	spatial frequency
λ	wavelength
ρ_0	coherence radius
σ_B^2	Rytov variance for a Gaussian beam
σ_I^2	scintillation index
σ_R^2	Rytov variance for a plane wave
$\sigma_{\ln I}^2$	log-irradiance variance
$\sigma_{\ln X}^2$	large-scale log-irradiance variance
$\sigma_{\ln Y}^2$	small-scale log-irradiance variance
σ_f^2	transverse spatial correlation length of a PCB phase screen
σ_g^2	variance of the autocorrelation of a PCB phase screen
σ_n^2	noise variance
σ_r^2	squared amplitude variation of a partially coherent phase screen
σ_s^2	jitter variance at the receiver due to pointing errors
$\langle\,\rangle$	ensemble average

1

Introduction

THIS CHAPTER gives an overview of the work presented herein. A glimpse on free-space optical communication is given, along with the motivations for the work conducted during this doctoral thesis. The book organization is also presented and some referencing conventions are explained.

1.1 Thesis Motivation

In the past decades a renewed interest has been seen around wireless optical communications (WOC), commonly known as free-space optics (FSO), because of the ever growing demand for high-data-rate data transmission as to a large extent current applications, such as high-definition (HD) contents and cloud computing, require great amount of data to be transmitted, hence, demanding more transmission bandwidth. Nowadays, the last mile problem continues to be the bottle neck in the global communication network. While the fiber-optic infrastructure—commonly called network backbone—is capable of coping with current demand, the end user accesses the network data stream mostly through copper based connections and radio-frequency (RF) wireless services, that are inherently slower technologies. Nevertheless, it has to be said that fiber-to-the-home (FTTH) connections are becoming more frequent, although this kind of services are only profitable in large urban areas. As the number of users increases, the RF spectrum is getting so crowded that there is virtually no room for new wireless services, with the additional inconvenient of limited bandwidth restriction for using a RF band and the license fees that have to be paid for such bands. Regarding cooper-based technologies, with the lower-speed connections offered compared to the backbone, such as DSL (digital subscriber line), cable modems, or T1's (transmission system 1), these are alternatives that make the service providers to incur in extra installation costs when deploying the wired network through the city.

When a fiber-optic link is neither practical nor feasible in the above scenario, FSO systems become a real alternative, since they allow to transfer data with high-bandwidth requirements and the additional advantages of wireless systems [1–3]. Moreover, a wireless optical communication system offers, when compared with RF technology, an intrinsic narrower beam; less power, mass and volume requirements, and the advantage of no regulatory policies for using optical frequencies and bandwidth.

On the other hand, satellite communication systems is a field where FSO is becoming more attractive thanks to the advantages mentioned above, and the additional fact that for *satellite-satellite* links there is no beam degradation due to the absence of atmosphere. Nevertheless, pointing systems complexity is increased as the order of the optical beam divergence is hundreds of μrad, whereas for a RF beam is in the order of tens to hundreds of mrad. The Semi-Conductor Inter Satellite Link EXperiment (SILEX) was the first European project to conduct a successful demo with the transmission of data through an optical link, between the SPOT-4 and Artemis satellites achieving 50 Mbps of transfer rate [4]. The first successful *ground-satellite* optical link was conducted between the ETS-VI satellite and the optical ground station (OGS) in Konegi, Japan [5]. There have also been other experiments such as the Ground/Orbiter Lasercomm Demonstrator (GOLD) [6], the Kirari Optical Communication Experiments (KODEN) [7], and the Kirari's Optical Downlink to Oberpfaffenhofen (KIODO) experiment where a link was established between an OGS in Germany and the OICETS satellite [8]. The Airbone Atmospheric Laser Link (LOLA, for its French initials), which used the Artemis optical payload and an airborne optical transceiver flying at 9000 m, has demonstrated the feasibility of *air-satellite* links.

The major drawback when deploying horizontal (*ground-ground*) wireless links based on FSO technology, where lasers are used as sources, is the perturbation of the

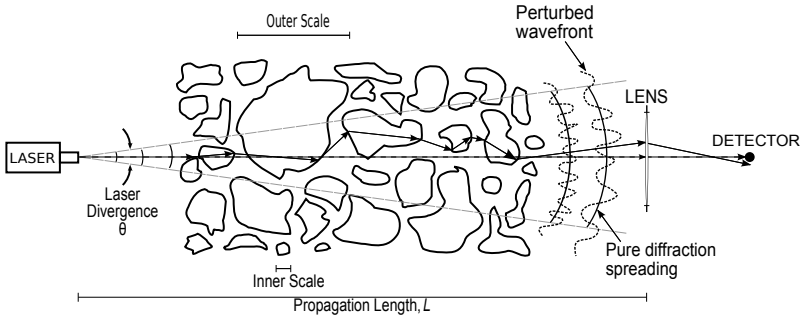

Figure 1.1 Laser beam propagation through the turbulent atmosphere.

optical wave as it propagates through the turbulent atmosphere. Moreover, fog, rain, snow, haze, and generally any floating particle can cause extinction of the signal-carrying laser beam intensity. In a worst case scenario the intensity attenuation can be strong enough to cause link outages, leading to a high bit error-rate that inevitably decreases the overall system performance and limits the maximum length for the optical link.

The turbulent atmosphere produces many effects, of which the most noticeable is the random fluctuations of the traveling wave irradiance, phenomenon known as scintillation. Additionally, there are other effects that perturb the traveling wavefront such as beam wander, that is a continuous random movement of the beam centroid over the receiving aperture plane; angle-of-arrival fluctuations, which are associated with the dancing of the focused spot on the photodetector surface; and beam spreading that is the spreading beyond the pure diffraction limit of the beam radius.

A compound of various perturbations suffered by an optical traveling wavefront is shown in Fig. 1.1. Here, it is depicted how small fluctuations in the atmospheric refractive index produce distortions int he wavefront provoking a random pattern, both in time and space, of self-interference of the beam at the points of the transverse receiver plane, and as a consequence rapid variations of the received power appear. The rays (solid arrows) leaving the laser source are deflected as they travel through the largest air pockets, whose size defines the turbulence outer scale, arriving off-axis instead of what is expected without turbulence, represented in Fig. 1.1 with the straight dashed arrow starting at laser and finishing at the receptor surface. Additionally, the turbulent atmosphere induces an extra spreading of the beam, i.e. the broadening of the beam size beyond of that expected due to pure diffraction, for the case of a laser beam. It is customary to refer as refractive effects to those caused by the outer scale size of turbulence, whereas, the inner scale sizes produce the diffractive effects. As the rays may also be interpreted as the wave vector for the traveling wavefront, the variations in the angle respect to the optical axis at the receiver represent the concept of angle-of-arrival fluctuations. Furthermore, this bouncing of the optical wavefront as it propagates through the atmosphere is also responsible for the beam wander effect as the centroid of the laser beam is displaced randomly at the receiver plane. The effect of placing a collecting aperture, e.g. a lens—as shown in Fig. 1.1—, at the receiver end of the FSO link is to mitigate the turbulence induced fading on the optical power. This phenomenon is known as *aperture averaging*.

The statistical analysis of the random irradiance fluctuations in FSO links is done through the probability density function (PDF), from which one can obtain other statistical tools to measure link performance such as the probability of fade and the bit error-rate (BER). More mathematically complex metrics can be derived from the PDF, such as the expected number of fades per unit time and their mean fade time. Historically, the PDF models that have drawn more attention are the Lognormal (LN) [9, p. 292], Beckmann [10], lognormally modulated exponential [11], Gamma-Gamma (GG) [12], and the K distribution [13]. Nowadays, the most widespread models for the irradiance data are, by far, the LN and GG distributions. Although both models comply with actual data in most scenarios neither of them is capable of fitting the irradiance data under all conditions of atmospheric turbulence for finite receiving aperture sizes [14]. Furthermore, there are several cases where neither the LN or the GG model seem to accurately fit the irradiance data, specially in the left tail of the PDF.

Herein, a new model is proposed for the irradiance fluctuations in FSO links under atmospheric turbulence in the presence of aperture averaging resulting in the exponentiated Weibull (EW) distribution. A physical justification for the appearance of the new model is provided, along with numerous test scenarios to assess its suitability to model the irradiance data in terms of the PDF and probability of fade, whereas new closed-form expressions for the average BER are presented. Moreover, the analysis on the EW distribution is conducted on fully and partially coherent Gaussian beam waves.

1.2 Thesis Overview

The remainder of this book is organized as follows. The next chapter presents a compact yet complete review of the current theory on free-space optical communication through the turbulent atmosphere. It starts by describing the atmospheric turbulence phenomenon and the most common atmospheric power spectrum models. Following with the propagation theory for Gaussian optical beam waves and the effects induced by atmospheric turbulence. A simulation method is described where random phase screens, accounting for the turbulence effects, are obtained either in the frequency domain or the spatial domain directly, using a fractal method. Finally, an analysis of FSO communication links is presented, along with the necessary tools to assess the performance of such links.

Chapter 3 is devoted to introduce the new proposed fading channel model resulting in the exponentiated Weibull distribution. After briefly reviewing the Lognormal and Gamma-Gamma model, the two most widespread fading models for FSO communications, a physical justification for the appearance of the EW model is developed. Furthermore, knowing that for any new PDF model to be accepted and actually be used by the FSO community it must has tractable expressions to estimate the distribution parameters, a set of equations relating the EW parameters directly to the scintillation index is provided, by making use of a semi-heuristic approach. In order to show that the EW distribution is a valid model for the irradiance data in weak-to-strong atmospheric turbulence, simulation results and experimental data are used to assess the new model, and comparisons are made to the LN and GG dis-

tributions. Moreover, a comparison to previously published data from other authors is conducted, including numerical simulation results and experimental data in the moderate-to-strong turbulence regime.

In Chapter 4 the analysis of the probability of fade and bit error-rate performance of a FSO link, when the atmospheric turbulence can be modeled by an exponentiated Weibull distribution, is presented. The BER analysis is conducted assuming a FSO link with intensity-modulation/direct-detection (IM/DD) FSO system using on-off keying (OOK) modulation. New closed-form expressions for the average BER are derived, for the EW and GG models, utilizing the very general special function known as Meijer's G-function. The same data set presented in Chapter 3 is used to evaluate the new expressions. Additionally, the average BER expression, for the proposed EW fading channel model, is extended to account for misalignment fading when pointing errors are included in the analysis. Monte Carlo simulations are conducted to assess this new expression.

The analysis for the exponentiated Weibull fading channel model is extended for partially coherent beams (PCB) in Chapter 5. First, the Gaussian Schell-model introduces the necessary theoretical tools to generate a PCB. Next, a recently developed approach to simulate partially coherent beams is presented. Moreover, this simulation technique is utilized to assess if the exponentiated Weibull model is still valid for a PCB propagating in atmospheric turbulence in the presence of aperture averaging.

Finally, Chapter 6 summarizes the main conclusions of the work developed during this Ph.D. Thesis. The current shortcomings of the proposed exponentiated Weibull model are pointed and the future research lines, envisioned as the next steps in the development of the EW fading channel model—that will help to enlarge the theoretical ground of the new model proposed—, are also presented.

In order to make the reading as agile as possible useful information, but not essential to understand the concepts being explained, has been compiled in the appendix section. In Appendix A a complete list of all the publications derived from the work presented in this thesis is given. Appendix B is a compound of some higher-order transcendental functions, key in applied sciences, needed in the mathematical development carried out throughout this book, specially in Chapter 4. A special notation is used in the text, when referring to some function definition or function relationship, by the capital letter 'B' followed by a sequential number—with sublevels within each function indicated by dots—, always enclosed in parenthesis. For example, the Gamma function $\Gamma(z)$ is defined in Eq. (B.1.1). Note that equations throughout this book are numbered sequentially within each chapter separately.

Lastly, Appendix C gives a complete set of equations to estimate the scintillation index for Gaussian beams, and Appendix D presents the mathematical derivation of different probability density function models in FSO fading channels, including the new exponentiated Weibull model proposed in this book.

2

Free-Space Optical Communications under Atmospheric Turbulence

THE AIM of this chapter is to present a complete review of the current theory on free-space optical communications through the turbulent atmosphere. It encompasses the basic theory of wave propagation in turbulent media, turbulence spectra and simulation techniques. Moreover, an approach to the theory behind the communication systems is presented.

2.1 Introduction

In recent years a large number of studies have been carried out on free-space optical (FSO) communication, some times also called wireless optical communication (WOC), with great interest on investigating the effects of the turbulent atmosphere on the communication link that mostly produces irradiance fluctuations in the received signal, greatly reducing link performance [15–19].

Whereas the most noticeable effect due to atmospheric turbulence is the random fluctuations of the signal-carrying laser beam intensity (irradiance), phenomenon known as *scintillation*, there are other perturbations affecting the traveling wavefront such as *beam wander*, that is a continuous random movement of the beam centroid over the receiving aperture plane; *angle-of-arrival fluctuations*, which are associated with the image jitter at the receiver focal plane; and *beam spreading* that is the spreading beyond the pure diffraction limit of the beam radius.

While the first works on atmospheric turbulence were primarily devoted to the plane and spherical wave propagation problem [20–24], soon the interest was redirected to the study of Gaussian beam waves [17, 25, 26], which is in fact the case for propagation of laser beams through the atmosphere. Hereafter, the analytic expression on the effects of atmospheric turbulence on propagating waves will be focused essentially on those for Gaussian beam.

With the purpose of mitigate the turbulence effects over a propagating Gaussian beam, there are a variety of techniques that have been proposed over the years. The first of these techniques to be applied was the aperture averaging [20], consisting in the use of a collecting lens as large as possible to effectively increase the area of the detector, hence, a larger portion of the incoming wavefront is concentrated into the photodetector. If the collecting lens is larger than the beam diameter at the receiver plane, and neglecting angle-of-arrival fluctuations and lens aberrations effects, then virtually all the intensity fluctuations due to scintillation can be averaged out. Recently, other mitigation techniques have been introduced, such as the use of phase diffusers as inexpensive beam expanders at the transmitter to create a partially coherent laser beam, that is claimed to reduce the scintillation effects [27], and the application of spatial diversity either at the transmitter or the receiver, by setting equally spaced multiple laser sources and receiving apertures, respectively [28]. An almost mandatory mitigation technique in coherent optical communications systems is based on *adaptive optics*, where fast-stearing mirrors are used to correct angle-of-arrival fluctuations, while correcting wavefront distortions is done with deformable mirrors and wavefront sensors [29–31]. Although, adaptive optics presents itself as a major alternative in coherent systems, its implementation on intensity-modulation with direct-detection (IM/DD) systems means a higher complexity burden on the receiver design and it does not represent a major improvement on system performance.

The rest of this chapter is organized as follows. In Sec. 2.2 some power spectrum models to characterize the turbulent atmosphere are addressed. Next, in Sec. 2.3, a short yet complete review of the propagation of optical electromagnetic waves in turbulent media is presented, followed by a brief introduction to the beam split-step method for the simulation of optical waves in Sec. 2.4. Finally, WOC systems are addressed from a communication theory approach where a general system characterization and performance evaluation are made in Sec. 2.5 and Sec. 2.6, respectively.

2.2 Atmospheric Turbulence

All the models used to describe the effects of the atmosphere on an optical traveling wave are based on the study of turbulence, which involves fluctuations in the velocity field of a viscous fluid [32]. These variations in the air of the atmosphere—i.e. the fluid—are firstly due to temperature differences between the surface of the Earth and the atmosphere, and, to the differences in temperature and pressure within the atmospheric layers themselves, thus, producing pockets of air, also known as eddies, that cause the atmospheric turbulence.

The different eddy sizes—i.e. the inertial range—, responsible for the transfer of kinetic energy within the fluid, go from the outer scale L_0 to the inner scale l_0 of turbulence, where typical values of L_0 are between 10 and 20 m, while l_0 is usually around 1–5 mm. Such conditions comprise a continuum where wind energy is injected in the macroscale L_0, transferred through the inertial range and finally dissipated in the microscale l_0. This energy transfer causes unstable air masses, with temperature gradients, giving rise to local changes in the atmospheric refractive-index and thus creating what is called *optical turbulence* as an optical wave propagates. Treating the atmospheric turbulence as a consequence of the fluctuations in refractive-index instead of temperature is the natural way to address wave propagation for optical frequencies. Following this reasoning is a good approach to define a power spectral density for refractive-index fluctuations as a means to express the atmospheric turbulence.

The variations of the atmospheric refractive-index n, which can be considered as locally homogeneous, can be mathematically expressed by

$$n(\vec{r}, t) = n_0 + n_1(\vec{r}, t), \tag{1}$$

where n_0 is the mean value of the index of refraction; $n_1(\vec{r}, t)$ is a random variable with zero mean, representing the changes caused by the atmospheric turbulence, and t indicates the temporal dependence. Nevertheless, under the *Taylor frozen turbulence hypothesis*, the turbulence is regarded as stationary as the optical wave propagates, hence, the time dependence is traditionally dropped in Eq. (1).

The statistical characterization of a locally homogeneous random field is usually done by its structure function, denoted by

$$D_n(\vec{r_1}, \vec{r_2}) = \langle [n(\vec{r_1}) - n(\vec{r_2})]^2 \rangle, \tag{2}$$

where there is no time dependence in the index of refraction.

2.2.1 Refractive-index structure parameter

The atmospheric turbulence can be defined by the strength of the fluctuations in the refractive-index, represented with the refractive-index structure parameter C_n^2 in units of $m^{-2/3}$—which has a direct relation with the structure function presented in Eq. (2). Along the optical propagation distance the value of C_n^2 has small variations for horizontal paths, while for slant and vertical paths these variations become significant. It's very common to assume a constant value in horizontal links, and to measure the path averaged value of C_n^2 from methods that rely on the atmospheric

data *in situ* [15, 33–35], or others that extract the C_n^2 value from experimental scintillation data [20, 36].

On the other hand, when a vertical path is considered, the behavior of C_n^2 is conditioned by temperature changes along the different layers within the Earth's atmosphere, hence, the refractive-index structure parameter becomes a function of the altitude above ground.

Many authors have tried to predict the behavior of the refractive-index structure parameter, and various models have been proposed. However, it should be noted that most of these models are based on fittings from experiments conducted in specific places, which makes difficult their generalization. Table 1 presents a list of different C_n^2 models, namely, the Submarine Laser Communication (SLC) Day model and the Hufnagel-Valley, best suited for inland day-time conditions, the HV-Night for night-time conditions, and the Greenwood model adapted for astronomical tasks on mountaintop locations. A comparative of all four refractive-index structure parameter models is shown in Fig. 2.1, where it is readily seen that day-time models predict higher values of C_n^2 than night-time models, as expected.

Sadot and Kopeika [35] have developed an empirical model for estimating the refractive-index structure parameter from macroscale meteorology measurements *in situ*. The value of C_n^2 depends strongly on the hour of the day. It has a peak value at midday and local minima at sunrise and sunset. Provided that the time elapsed between the sunrise and sunset is different according to seasonal variations, the concept of *temporal hour* (t_h) has been introduced. The duration of a temporal hour is $1/12^{\text{th}}$ of the time between sunrise and sunset. In summer it is more than 60 min and in winter is lower, therefore, it can be seen as a solar hour. The current t_h is obtained by subtracting the sunrise time from the local time, and dividing by the value of one t_h. Thus, in any day of the year $t_h = 00:00$ at sunrise, $t_h = 06:00$ at noon, and

Table 1 Refractive-index structure parameter models as a function of the altitude h above ground. For the HV model, $A = C_n^2(0)$ is the refractive-index structure parameter at ground level, and v is the rms wind speed.

Model	Expression
SLC-Day	$C_n^2(h) = \begin{cases} 1.700\times10^{-14} & 0\text{ m} < h < 19\text{ m} \\ 4.008\times10^{-13}h^{-1.054} & 19\text{ m} < h < 230\text{ m} \\ 1.300\times10^{-15} & 230\text{ m} < h < 850\text{ m} \\ 6.352\times10^{-7}h^{-2.966} & 850\text{ m} < h < 7000\text{ m} \\ 6.209\times10^{-16}h^{-0.6229} & 7\text{ km} < h < 20\text{ km} \end{cases}$
Hufnagel-Valley Day	$C_n^2(h) = Ae^{-h/100} + 5.94\times10^{-53}\left(\frac{v}{27}\right)^2 h^{10}e^{-h/1000} + 2.7\times10^{-16}e^{-h/1500}$
Hufnagel-Valley Night	$C_n^2(h) = 1.9\times10^{-15}e^{-h/100} + 8.16\times10^{-54}h^{10}e^{-h/1000} + 3.02\times10^{-17}e^{-h/1500}$
Greenwood	$C_n^2(h) = \left[2.2\times10^{-13}(h+10)^{-1.3} + 4.3\times10^{-17}\right]e^{-h/1500}$

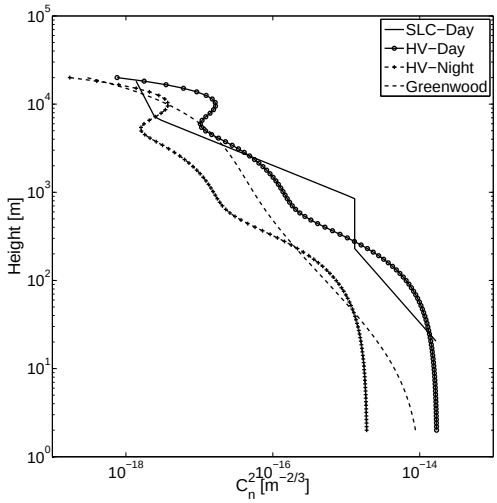

Figure 2.1 Refractive-index structure parameter altitude profile of different models. For HV-day model $A = 1.7 \cdot 10^{-14}\mathrm{m}^{-2/3}$ and $v = 21\mathrm{m/s}$.

$t_h = 12:00$ at sunset. It should be noted that temporal hours are allowed to have negative time hours.

The expression obtained that describes the refractive-index structure constant C_n^2 is based on a polynomial regression model according to

$$\begin{aligned} C_n^2 =& 3.8 \times 10^{-14} W_{t_h} + 2 \times 10^{-15} T - 2.8 \times 10^{-15} \mathrm{RH} + 2.9 \times 10^{-17} \mathrm{RH}^2 \\ & - 1.1 \times 10^{-19} \mathrm{RH}^3 - 2.5 \times 10^{-15} \mathrm{WS} + 1.2 \times 10^{-15} \mathrm{WS}^2 \\ & - 8.5 \times 10^{-17} \mathrm{WS}^3 - 5.3 \times 10^{-13}, \end{aligned} \tag{3}$$

where W_{t_h} denotes a temporal-hour weight (see Table 2), T is the temperature in Kelvins, RH is the relative humidity (%), and WS is the wind speed in ms^{-1}—which is measured as the wind component transverse to the optical path.

An improved version of this model is also presented in Sadot and Kopeika [35], with introduction of the effects of solar radiation and the aerosol loading in the atmo-

Table 2 Weight W_{t_h} parameter as a function of the corresponding temporal hour.

Temporal hour interval			W_{t_h}
	until	-4	0.11
-4	to	-3	0.11
-3	to	-2	0.07
-2	to	-1	0.08
-1	to	0	0.06
Sunrise $\rightarrow$ 0	to	1	0.05
1	to	2	0.10
2	to	3	0.51
3	to	4	0.75
4	to	5	0.95

Temporal hour interval			W_{t_h}
5	to	6	1.00
6	to	7	0.90
7	to	8	0.80
8	to	9	0.59
9	to	10	0.32
10	to	11	0.22
Sunset $\rightarrow$ 11	to	12	0.10
12	to	13	0.08
	over	13	0.13

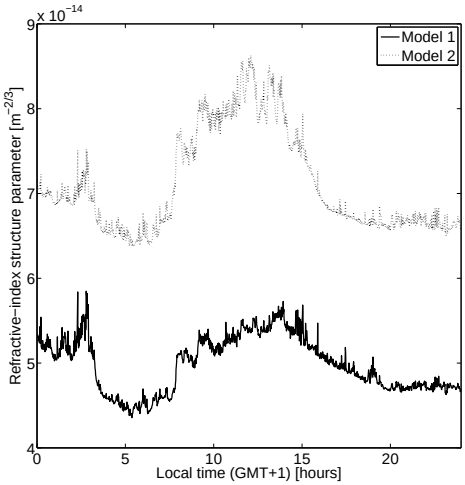

Figure 2.2 Refractive-index structure parameter predicted from macroscale meteorologic and aerosols from data collected in an autumn day in Barcelona, Spain.

sphere, as follows

$$\begin{aligned} C_n^2 =& 5.9\times10^{-15}W_{t_h} + 1.6\times10^{-15}T - 3.7\times10^{-15}\mathrm{RH} + 6.7\times10^{-17}\mathrm{RH}^2 \\ & - 3.9\times10^{-19}\mathrm{RH}^3 - 3.7\times10^{-15}\mathrm{WS} + 1.3\times10^{-15}\mathrm{WS}^2 \\ & - 8.2\times10^{-17}\mathrm{WS}^3 + 2.8\times10^{-14}\mathrm{SF} - 1.8\times10^{-14}\mathrm{TCSA} \\ & + 1.4\times10^{-14}\mathrm{TCSA}^2 - 3.9\times10^{-13}, \end{aligned} \tag{4}$$

where SF is the solar flux in units of kWm^{-2}, and TCSA is the total cross-sectional area of the aerosol particles and its expression can be found in Yitzhaky et al. [37]

$$\begin{aligned} TCSA =& 9.96\times10^{-4}\mathrm{RH} - 2.75\times10^{-5}\mathrm{RH}^2 + 4.86\times10^{-7}\mathrm{RH}^3 \\ & - 4.48\times10^{-9}\mathrm{RH}^4 + 1.66\times10^{-11}\mathrm{RH}^5 - 6.26\times10^{-3}\ln\mathrm{RH} \\ & - 1.37\times10^{-5}\mathrm{SF}^4 + 7.30\times10^{-3}. \end{aligned} \tag{5}$$

A 24-hour data set of macroscale meteorologic measurements taken at the Campus Nord in the Technical University of Catalonia in Barcelona, Spain, collected on the 14$^{\text{th}}$ of November of 2009 was used to generate the plot presented in Fig. 2.2, of the estimated refractive-index structure parameter C_n^2 using Eq. (3) and Eq. (4) for Model 1 and Model 2, respectively.

2.2.2 Atmospheric power spectrum models

The first studies on the atmospheric turbulence effects on propagating light waves were conducted by Tatarski [9] using the Rytov method and considering, as still does nowadays, the Kolmogorov turbulence spectrum [38] which suggests that the inertial range has a degree of statistical consistency, where points in the atmosphere separated certain scale size exhibit statistical homogeneity and isotropy. The use of these

characteristics, along with additional simplifications and assumptions, was essential to develop tractable expressions for an essentially nonlinear phenomenon, as the atmospheric turbulence.

Kolmogorov was the first to derive an expression, which led to the spectrum model

$$\Phi_n(\kappa) = 0.033 C_n^2 \kappa^{-11/3}, \tag{6}$$

where κ is the scalar spatial frequency (in rad/m).

Although Eq. (6) is only valid over the inertial subrange, $1/L_0 \ll \kappa \ll 1/l_0$, often it is assumed that the outer scale is infinite and the inner scale is negligibly small in order to make use of it for all wave numbers. However, in practice, making this assumption can lead to untrustworthy results when using the Kolmogorov spectrum for wave numbers out of the actual inertial range.

To overcome the singularities appearing in Eq. (6) other spectrum models have been proposed. Tatarskii suggested to include the inner scale effects with a Gaussian function, defining a new power spectral density for refractive-index fluctuations in the form

$$\Phi_n(\kappa) = 0.033 C_n^2 \kappa^{-11/3} \exp\left(-\frac{\kappa^2}{\kappa_m^2}\right), \quad \kappa \gg 1/L_0; \quad \kappa_m = 5.92/l_0. \tag{7}$$

The Tatarskii spectrum still presents a mathematical singularity at $\kappa = 0$ in the limiting case $L_0 \to \infty$. A further improvement of the Tatarskii and Kolmogorov spectrum, valid for all wave numbers, called the von Kármán spectrum is given by the expression

$$\Phi_n(\kappa) = 0.033 C_n^2 \frac{\exp(-\kappa^2/\kappa_m^2)}{(\kappa^2 + \kappa_0^2)^{11/3}}, \quad 0 \le \kappa < \infty; \quad \kappa_m = 5.92/l_0, \tag{8}$$

where $\kappa_0 = 2\pi/L_0$.

It should be noted that both Eq. (7) and Eq. (8) reduce to the Kolmogorov power spectrum, when evaluated in the inertial range $\kappa_0 \ll \kappa \ll \kappa_m$.

The spatial power spectral density of refractive-index fluctuations, as being derived from a locally homogeneous random field, is described by its structure function defined by

$$D_n(\vec{r}) = 8\pi \int_0^\infty \kappa^2 \Phi_n(\vec{\kappa}) \left(1 - \frac{\sin \vec{\kappa} \cdot \vec{r}}{\vec{\kappa} \cdot \vec{r}}\right) d\vec{\kappa}, \tag{9}$$

where $\Phi_n(\vec{\kappa})$ is the power spectrum model of interest.

2.3 Propagation Theory

An optical wave propagating through the atmosphere will be altered by refractive-index inhomogeneities that form turbulent eddies of different sizes, where energy is injected in the macroscale L_0 and transfered through ever smaller turbulent eddies and finally dissipated at the microscale l_0 . This energy transfer causes unstable air masses, with temperature gradients, giving rise to local changes in the atmospheric refractive-index and thus inducing perturbations as the optical wave propagates.

These random variations on the amplitude and phase of the traveling wave can be addressed analytically, by solving the wave equation for the electric field and its respective statistical moments. For a propagating electromagnetic wave the electric field is derived from the *stochastic Helmholtz equation*

$$\nabla^2\vec{E} + k^2 n^2(\vec{r})\vec{E} = 0, \tag{10}$$

where $k = 2\pi/\lambda$ is the wavenumber, $\vec{r}$ is a point in space and $n(\vec{r})$ is given by Eq. (1).

In practice, the actual equation to be solved is the *scalar* stochastic Helmholtz equation

$$\nabla^2 U + k^2 n^2(\vec{r})U = 0, \tag{11}$$

which corresponds to one of the three components of the electric field.

To solve Eq. (11) the Born and Rytov approximations have traditionally been used. Additionally, several assumptions are made, namely, backscattering and depolarization effects are neglected, the refractive-index is assumed uncorrelated in the direction of propagation, and the paraxial approximation can be used.

2.3.1 Born approximation

In the Born approximation the solution of Eq. (11) is assumed to be a sum of terms of the form

$$U(\vec{r}) = U_0(\vec{r}) + U_1(\vec{r}) + U_2(\vec{r}) + \cdots, \tag{12}$$

where $U_0(\vec{r})$ represents the unperturbed field, i.e. an optical wave traveling through free-space. While $U_1(\vec{r})$ and $U_2(\vec{r})$ denote first-, second-order, and so on, perturbations caused by inhomogeneities due to the random term $n_1(\vec{r})$ in Eq. (1).

Next, by using the fact that in Eq. (1) $n_o \cong 1$ and $|n_1(\vec{r})| \ll 1$, Eq. (11) reduces to

$$\nabla^2 U(\vec{r}) + k^2\left[1 + 2n_1(\vec{r})\right]U(\vec{r}) = 0, \tag{13}$$

Finally, substituting Eq. (12) into Eq. (13) yields [32]

$$\nabla^2 U_0 + k^2 U_0 = 0, \tag{14}$$

$$\nabla^2 U_1 + k^2 U_1 = -2k^2 n_1(\vec{r})U_0(\vec{r}), \tag{15}$$

$$\nabla^2 U_2 + k^2 U_2 = -2k^2 n_1(\vec{r})U_1(\vec{r}), \tag{16}$$

and so on for higher order perturbations terms.

Solving Eq. (14) gives the unperturbed propagated optical field, whereas solving Eq. (15) and Eq. (16) give the two lower-order perturbed fields. Next, a brief explanation on how to solve this system of equations is given below.

2.3.1.1 Unperturbed field

Let us refer to Fig. 1.1 and consider a Gaussian beam wave propagating in the z direction, where the input plane $z = 0$ of the system is located at the output of the laser, and the output plane is located at the receiver lens position. The initial field can be described by [39]

$$U_0(r, 0) = A\exp\left(-\frac{r^2}{W_0^2}\right)\exp\left(-i\frac{kr^2}{2F_0}\right), \tag{17}$$

where r is the distance from the beam center, and W_0 and F_0 are the beam radius and phase front radius at the transmitter plane, respectively.†

Furthermore, the Gaussian beam can be characterized by the input parameters

$$\Theta_0 = 1 - \frac{z}{F_0}, \tag{18}$$

$$\Lambda_0 = \frac{2z}{kW_0^2}, \tag{19}$$

and by the output parameter in the receiver plane at $z = L$

$$\Theta = 1 + \frac{L}{F} = \frac{\Theta_0}{\Theta_0^2 + \Lambda_0^2}, \tag{20}$$

$$\Lambda = \frac{2L}{kW^2} = \frac{\Lambda_0}{\Theta_0^2 + \Lambda_0^2}, \tag{21}$$

where W and F are the beam radius and phase front radius at the receiver plane, respectively.

The set of parameters defining a Gaussian beam presented above corresponds to the notation used in Andrews and Philips [32]. Nevertheless, other ways of characterizing a Gaussian beam can be utilized, such that used in Ricklin et al. [16].

The solution of Eq. (11) for propagating a Gaussian beam wave a distance z in free-space is given by

$$U_0(r,z) = \frac{1}{\sqrt{\Theta_0^2 + \Lambda_0^2}} \exp\left(-\frac{r^2}{W^2}\right) \exp\left[i\left(kz - \varphi - \frac{kr^2}{2F}\right)\right], \tag{22}$$

where Θ_0 and Λ_0 are non-dimensional parameters defined above, and φ, W, and F are the longitudinal phase shift, beam radius, and radius of curvature after propagating a distance z. These quantities are defined by

$$\varphi = \tan^{-1}\frac{\Lambda_0}{\Theta_0}, \tag{23}$$

$$W = W_0\sqrt{\Theta_0^2 + \Lambda_0^2}, \tag{24}$$

$$F = \frac{kW_0^2}{2}\left[\frac{\Lambda_0(\Theta_0 + \Lambda_0)}{\Theta_0(1-\Theta_0) - \Lambda_0}\right]. \tag{25}$$

2.3.1.2 Perturbations terms

For an optical wave propagating a distance L in the z direction, the first-order perturbation term of the final field is given by

$$U_1(\vec{r}) = 2k^2 \iiint_V G(\vec{r},\vec{s}) n_1(\vec{s}) U_0(\vec{s}) d\vec{s}, \tag{26}$$

†The notation used in this section is taken from Andrews and Philips [32]. Special care has to be taken with this notation, where W_0 is specifically referring to the beam radius at the output of the light source, and it should not be confused with the actual beam waist of a Gaussian beam W_B.

where $U_0(\vec{s})$ and $G(\vec{r},\vec{s})$ are the unperturbed field [see Eq. (22)] and the free-space *Green's function* [40], respectively. Moreover, by applying the paraxial approximation the first Born approximation reduces to

$$U_1(\vec{r},L) = \frac{k^2}{2\pi}\int_0^L dz \iint_\infty^\infty d^2s \exp\left[ik(L-z)+\frac{ik|\vec{s}-\vec{r}|^2}{2(L-z)}\right] \times U_0(\vec{s},z)\frac{n_1(\vec{s},z)}{L-z}. \quad (27)$$

When solving for higher-order perturbation terms in the Born approximation, the following recurrent formula can be used

$$U_m(\vec{r},L) = \frac{k^2}{2\pi}\int_0^L dz \iint_\infty^\infty d^2s \exp\left[ik(L-z)+\frac{ik|\vec{s}-\vec{r}|^2}{2(L-z)}\right] \times U_{m-1}(\vec{s},z)\frac{n_1(\vec{s},z)}{L-z}, \quad (28)$$

where m indicates the order of the perturbation term to be calculated.

2.3.2 Rytov approximation

The Rytov approximation assumes a solution for Eq. (11) formed by the unperturbed field $U_0(\vec{r})$ modified by complex phase perturbations, expressed as

$$U(\vec{r}) = U_0(\vec{r})\exp\left[\psi_1(\vec{r})+\psi_2(\vec{r})+\cdots\right], \quad (29)$$

where $\psi_1(\vec{r})$ and $\psi_2(\vec{r})$ are first- and second-order phase perturbations, respectively. These perturbations are defined by [40]

$$\begin{aligned}\psi_1(\vec{r}) &= \Phi_1(\vec{r}),\\ \psi_2(\vec{r}) &= \Phi_2(\vec{r})-\tfrac{1}{2}\Phi_1^2(\vec{r}),\end{aligned} \quad (30)$$

where the new function $\Phi_m(\vec{r})$ appearing in the system of equations in Eq. (30) are directly related with the Born perturbation terms in the form

$$\Phi_m(\vec{r}) = \frac{U_m(\vec{r})}{U_0(\vec{r})} \quad (31)$$

Historically, the Born approximation was first introduced but its results were limited to conditions of extremely weak scintillation. Afterwards, the second-order Rytov approximation won more acceptance thanks to the good agreement with scintillation data in the weak fluctuation regime.

2.3.3 Statistical moments

The first relevant statistical moment for a traveling optical field is the second-order moment, also known as the *mutual coherence function* (MCF), which is defined as the ensemble average in two points of the field, taken in a plane perpendicular to the propagation direction at a distance L from the source, as follows

$$\Gamma_2(\vec{r_1},\vec{r_2},L) = \langle U(\vec{r_1},L)U^*(\vec{r_2},L)\rangle, \quad (32)$$

where $U(\vec{r})$ is the Rytov approximation solution for Eq. (11), and the brackets $\langle\cdot\rangle$ denote an ensemble average. Vectors $\vec{r_1}$ and $\vec{r_2}$ are transversal vectors without z component, which is chosen as the propagation direction.

Solving Eq. (32)

$$\begin{aligned}\Gamma_2(\vec{r_1},\vec{r_2},L) &= \Gamma_2^0(\vec{r_1},\vec{r_2},L)\exp\left[\sigma_r^2(\vec{r_1},L)+\sigma_r^2(\vec{r_2},L)-T\right]\\ &\quad\times\exp\left[\frac{-1}{2}\Delta(\vec{r},\vec{r},L)\right],\end{aligned} \tag{33}$$

where

$$\Gamma_2^0(\vec{r_1},\vec{r_2},L) = U_0(\vec{r_1},L)U_0^*(\vec{r_2},L)\langle\exp\left[\psi(\vec{r_1},L)+\psi^*(\vec{r_2},L)\right]\rangle, \tag{34}$$

$$\begin{aligned}\sigma_r^2(r,L) &= 2\pi^2k^2L\int_0^1\int_0^\infty \kappa\Phi_n(\kappa)\exp\left(-\frac{\Lambda L\kappa^2\xi^2}{k}\right)\\ &\quad\times\left[I_0(2\Lambda r\xi\kappa)-1\right]d\kappa d\xi,\end{aligned} \tag{35}$$

$$\begin{aligned}\sigma_r^2(0,L) &= 2\pi^2k^2L\int_0^1\int_0^\infty \kappa\Phi_n(\kappa)\exp\left(-\frac{\Lambda L\kappa^2\xi^2}{k}\right)\\ &\quad\times\left\{1-\cos\left[\frac{L\kappa^2}{k}\xi(1-\overline{\Theta}\xi)\right]\right\}d\kappa d\xi,\end{aligned} \tag{36}$$

and $I_0(\cdot)$ is the modified Bessel function of zero order, T is a term denoting the fluctuations of on-axis mean irradiance at the receiver plane caused by atmospheric turbulence [32, Chp. 6.3], and the most-right exponential of Eq. (35) is the complex degree of coherence (DOC).

From the MCF and the DOC some physical effects on the optical traveling wave can be derived, namely the mean irradiance, turbulence-induced beam spreading, angle-of-arrival fluctuations and beam wander.

Actually, the most important effect caused by atmospheric turbulence is the optical scintillation, and it is quantified by the *scintillation index* (SI)

$$\sigma_I^2(\vec{r},L) = \frac{\left\langle I^2(\vec{r},L)\right\rangle}{\left\langle I(\vec{r},L)\right\rangle^2}-1, \tag{37}$$

where $I(\vec{r},L)$ denotes the irradiance of the optical field in the receiver plane.

The mathematical derivation of σ_I^2 relies upon the fourth statistical moment of the optical field $U(\vec{r})$, given by

$$\Gamma_4(\vec{r_1},\vec{r_2},\vec{r_3},\vec{r_4},L) = \langle U(\vec{r_1},L)U^*(\vec{r_2},L)U(\vec{r_3},L)U^*(\vec{r_4},L)\rangle. \tag{38}$$

By setting $\vec{r_1}=\vec{r_2}=\vec{r_3}=\vec{r_4}=\vec{r}$ and evaluating Eq. (32) and Eq. (38) for the same point, yields

$$\langle I^2(\vec{r},L)\rangle = \Gamma_4(\vec{r},\vec{r},\vec{r},\vec{r},L), \tag{39}$$

$$\langle I(\vec{r},L)\rangle = \Gamma_2(\vec{r},\vec{r},L), \tag{40}$$

thus, obtaining an analytic expression for the scintillation index.

A fundamental parameter in the study of optical wave propagation through random media is the Rytov variance σ_R^2, which is in fact the scintillation index for a

plane wave in the weak turbulence regime. The Rytov variance can be derived from Eq. (36), and by setting $\Lambda = 0$ and $\Theta = 1$ in the limiting case of a plane wave, yields

$$\sigma_R^2 = 1.23 C_n^2 k^{7/6} L^{11/6}. \tag{41}$$

A more detailed explanation on the derivation of the solution of Eq. (10), and the statistical moments of the optical field can be found in [32].

2.3.4 Extended Rytov theory

The Rytov approximation is valid only in weak irradiance fluctuations regime, and an extension of the theory is needed to address strong turbulence effects on optical traveling waves. As a wave propagates through the turbulent atmosphere its degree of transverse spatial coherence decreases, this coherence loss is quantified by the *spatial coherence radius*

$$\rho_0 = \begin{cases} \left(\frac{3}{1+\Theta+\Theta^2+\Lambda^2}\right)^{1/2} \left(1.87 C_n^2 k^2 L l_0^{-1/3}\right)^{-1/2}, & \rho_0 \ll l_0 \\ \left(\frac{8}{3\left(a+0.62\Lambda^{11/6}\right)}\right)^{3/5} \left(1.46 C_n^2 k^2 L\right)^{-3/5}, & l_0 \ll \rho_0 \ll L_0, \end{cases} \tag{42}$$

where a is a constant [32, p. 192]. It should be noted that Θ and Λ are dimensionless parameters associated with the Gaussian beam. The expression for ρ_0 in the limiting cases of plane wave ($\Lambda = 0$, $\Theta = 1$), and spherical wave ($\Lambda = 0$, $\Theta = 0$) can be deduced from Eq. (42).

Another parameter to measure the spatial coherence is the *atmospheric coherence width* $r_0 = 2.1\rho_0$, widely known as the Fried parameter. For the limiting case of a plane wave the Fried parameter is given by

$$r_0 = \left(0.42 C_n^2 k^2 L\right)^{-3/5}. \tag{43}$$

Under the extended Rytov theory the refractive-index $n_1(\vec{r})$ in Eq. (1) can be seen as the result of the influence of two terms, i.e., the large-scale inhomogeneities $n_X(\vec{r})$ and the small-scale inhomogeneities $n_Y(\vec{r})$. Thus, as the refractive-index directly influences the turbulence power spectrum, an *effective* power spectral density for refractive-index fluctuations can be expressed by

$$\Phi_{ne}(\kappa) = \Phi_n(\kappa) G(\kappa, l_0, L_0) = \Phi_n(\kappa) \left[G_X(\kappa, l_0, L_0) + G_Y(\kappa, l_0)\right], \tag{44}$$

where G_X and G_Y are amplitude spatial filters modeling the large-scale and small-scale perturbations, respectively.

The effective atmospheric spectrum can be used instead of the classic spectrum to solve the statistical moments of a traveling optical field, thus, allowing to treat the effects of inner-scale size and outer-scale size of turbulence separately throughout the theory.

2.3.5 Physical effects

2.3.5.1 Angle-of-arrival fluctuations

Referring to Fig. 1.1 the rays (solid arrows) leaving the laser source are deflected as they travel through the turbulent atmosphere, some arriving off-axis instead of what

is expected without turbulence, represented with the horizontally straight dashed arrow. As the rays may also be interpreted as the wave vector for the traveling wavefront, the variations in the angle respect the optical axis at the receiver represent the concept of angle-of-arrival fluctuations. The expression for the angle-of-arrival fluctuations, that directly depends on the turbulence strength and the optical path length, is given by

$$\langle \beta_a^2 \rangle = 2.91 C_n^2 L (2W_G)^{-1/3}, \tag{45}$$

where W_G is the soft aperture radius, and it is related to the receiving aperture D by $D^2 = 8W_G^2$.

The main technique to counterbalance the negative effects of receiving the optical wave off-axis, is by the combination of *fast steering mirrors* and adaptive optics algorithms [29–31].

2.3.5.2 Beam wander

The beam wander effect is related to the displacement of the instantaneous center of the beam—defined as the point of maximum irradiance—of the traveling wave over the receiver plane. It is well known that this phenomenon is caused by the large-scale inhomogeneities due to their refractive effects. A Gaussian beam wave after propagating through the turbulent atmosphere is corrupted in such a way that the instantaneous field, at the receiver plane, greatly differs from a Gaussian shape, with the added characteristic that the beam center can exhibit major deviations from the optical axis of the link.

On the other hand, the short-term and long-term fields have a field shape that resembles that of a Gaussian beam. Nevertheless, the optical field in the short-term exposition is skewed from a Gaussian beam profile, while the long-term profile describes a more accurate Gaussian profile and the deviation of the beam center from the optical axis is relatively small, and can be neglected. A computer simulation of a Gaussian beam, shown in Fig. 2.3, was conducted following the method described in Dios et al. [41], where the field profile for different exposure times is presented. For this simulation it was assumed a propagation distance of $L = 2000$ m, $C_n^2 = 6 \times 10^{-15}$ m$^{-2/3}$, $\lambda = 1064$ nm, $W_0 = 2$ cm, and the exposition time of the long-term profile in Fig. 2.3(c) is 34 times of that used for the short-term profile in Fig. 2.3(b).

Fante [42] in his work relates the random displacements of the incoming wavefront center or "hot spot" with the long-term W_{LT} and short-term W_{ST} spot sizes, assuming that the "hot spot" coincides with beam centroid, by the expression

$$\langle r_c^2 \rangle = W_{\mathrm{LT}}^2 - W_{\mathrm{ST}}^2, \tag{46}$$

where W_{LT} is the long-term beam radius and, following the conventional Rytov method, its form is [43]

$$W_{\mathrm{LT}}^2 = W^2 \left[1 + 1.33 \sigma_R^2 \Lambda^{5/6} \right], \quad \Lambda = \frac{2L}{kW^2}, \tag{47}$$

where W is the pure diffraction beam radius at the receiver plane. Furthermore, the

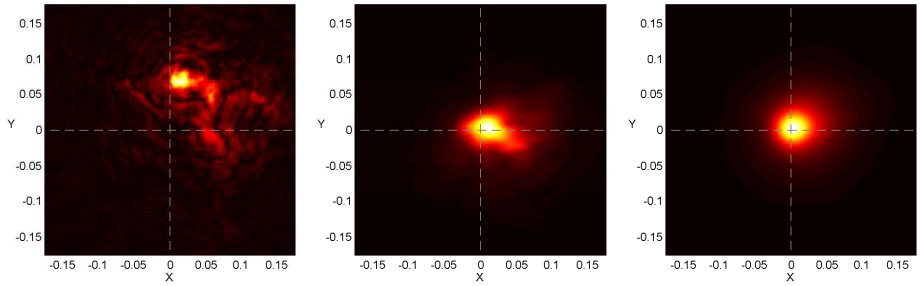

(a) Instantaneous beam. (b) Short-term beam. (c) Long-term beam.

Figure 2.3 Profile of a Gaussian beam with different exposure times, after propagating 2000 m in atmospheric turbulence.

short-term beam radius is given by

$$W_{\mathrm{ST}}^2 = W^2 \left\{ 1 + 1.33\sigma_R^2 \Lambda^{5/6} \left[1 - 0.66 \left(\frac{\Lambda_0^2}{1+\Lambda_0^2} \right)^{1/6} \right] \right\}. \tag{48}$$

It is clear how in Eq. (47) and Eq. (48) the extra beam spreading effect due to the atmospheric turbulence is included through the Rytov variance σ_R^2.

For the sake of simplicity, the *geometrical optics approximation* used by Churnside and Lataitis [44] yields a closed form expression for the beam wander

$$\langle r_c^2 \rangle = 0.97 C_n^2 L^3 W_0^{-1/3}, \tag{49}$$

while taking into account that this expression is valid for an infinite outer scale and a collimated beam, as is mostly assumed.

2.3.5.3 Scintillation

A laser beam propagating through the atmosphere will be altered by refractive-index inhomogeneities. At the receiver plane, a random pattern is produced both in time and space [23]. The irradiance fluctuations over the receiver plane resembles the speckle phenomenon observed when a laser beam impinges over a rugged surface. The parameter that expresses these irradiance fluctuations is the scintillation index (SI)

$$\sigma_I^2 = \frac{\langle I^2 \rangle - \langle I \rangle^2}{\langle I \rangle^2} = \frac{\langle I^2 \rangle}{\langle I \rangle^2} - 1, \tag{50}$$

where $I \equiv I(0, L)$ denotes irradiance of the optical wave observed by a point detector after propagating a distance L.

Classical studies on optical wave propagation have been classified in two major categories, either the weak or strong fluctuations theory. It is customary to discriminate both cases for a given propagation problem by determining the value of the Rytov variance σ_R^2. The weak fluctuations regime occurs when $\sigma_R^2 < 1$, the strong

fluctuations regime is associated with $\sigma_R^2 > 1$, whereas if $\sigma_R^2 \to \infty$ results in the saturation regime.

Different expressions are derived for the SI depending on whether the calculation has to be done in the weak or the strong fluctuations regime, although, when $\sigma_R^2 \sim 1$ both expressions will give similar results. Andrews et al. [17] have developed a set of expressions for the SI of Gaussian-beam waves and claim to be valid in the weak-to-strong fluctuation regime. This work is based on the extended Rytov theory. The idea behind this approach is to separate the influence of the turbulence in two parts, namely, that caused by the small-scale eddies—that are assumed to be diffractive inhomogeneities—on one hand, and, on the other, the effects caused by the large-scale eddies—regarded as refractive inhomogeneities. Mathematically the normalized irradiance is then written as

$$\hat{I} = \frac{I}{\langle I \rangle} = XY, \tag{51}$$

where X and Y are unit mean statistically independent processes arising from the large-scale and small-scale size of turbulence, respectively. Alternatively, the irradiance can be written as $I = A\exp(2\chi)$, where χ is the log-amplitude of the optical wave. Moreover, when χ is normally distributed, the variance of the log-amplitude is related to scintillation index according to

$$\sigma_I^2 = \exp\left(4\sigma_\chi^2\right) - 1 = \exp\left(\sigma_{\ln I}^2\right) - 1, \tag{52}$$

where $\sigma_{\ln I}^2$ is the variance of the log-irradiance, that in turn depends on the large-scale $\sigma_{\ln X}^2$ and small-scale $\sigma_{\ln Y}^2$ variances as follows

$$\sigma_{\ln I}^2 = 4\sigma_\chi^2 = \sigma_{\ln X}^2 + \sigma_{\ln Y}^2. \tag{53}$$

Under the Rytov approximation, the on-axis log-irradiance scintillation index for a point receiver has the integral form

$$\sigma_{\ln I}^2 = 8\pi^2 k^2 L \int_0^1 \int_0^\infty \kappa \Phi_n(\kappa) \exp\left(-\frac{\Lambda L \kappa^2 \xi^2}{k}\right) \left\{1 - \cos\left[\frac{L\kappa^2}{k}\xi(1-\overline{\Theta}\xi)\right]\right\} d\kappa d\xi \tag{54}$$

where $\overline{\Theta} = 1 - \Theta$.

If one uses the simple Kolmogorov spectrum for $\Phi_n(\kappa)$ then the solution of Eq. (54) is only valid in weak turbulence. In this regime the approximation $\sigma_I^2 \cong \sigma_{\ln I}^2$ is valid, and thus the scintillation index for Gaussian beam is given by

$$\sigma_I^2 = 3.86\sigma_R^2 \Re\left\{i^{5/6}{}_2F_1\left(-\frac{5}{6}, \frac{11}{6}; \frac{17}{6}; \overline{\Theta} + i\Lambda\right) - \frac{11}{6}\Lambda^{5/6}\right\}, \tag{55}$$

where $\Re\{\cdot\}$ is the real part operator, and ${}_2F_1(\cdot)$ is a hypergeometric function [See Appendix B.3]. Equation (55) can be approximated by

$$\sigma_I^2 = 3.86\sigma_R^2 \left\{0.40[(1+2\Theta)^2 + 4\Lambda^2]^{5/12} \cos\left[\frac{5}{6}\tan^{-1}\left(\frac{1+2\Theta}{2\Lambda}\right)\right] - \frac{11}{16}\Lambda^{5/6}\right\}, \tag{56}$$

where Θ and Λ are defined by Eq. (20) and Eq. (21), respectively. The expression in Eq. (56) is often regarded as the *Rytov variance for a Gaussian beam wave* σ_B^2.

In order to account for moderate-to-strong turbulence effects the extended Rytov approximation is applied—by means of the effective spectrum in Eq. (44)—, using the large-scale G_X and small-scale G_Y filters defined by

$$G_X(\kappa) = \exp\left(-\frac{\kappa^2}{\kappa_X^2}\right), \tag{57}$$

$$G_Y(\kappa) = \frac{\kappa^{11/3}}{(\kappa^2+\kappa_Y^2)^{11/6}} \exp\left[\frac{\Lambda L\kappa^2(1-z/L)^2}{k}\right],\ \kappa_Y \gg 1, \tag{58}$$

respectively; where κ_X and κ_Y are variables denoting low- and high-pass spatial frequency cutoffs, that eliminate the ineffective scale sizes in the turbulent process for the moderate-to-strong fluctuations regime [32, p. 327]. Nevertheless, it should be noted that Eq. (57) and Eq. (58) do not account for the inner-scale l_0 and outer-scale L_0 of turbulence.

Now using the effective atmospheric spectrum defined above, Eq. (54) can be solved for the large-scale $\sigma^2_{\ln X}$ and small-scale $\sigma^2_{\ln Y}$ variances, separately. Moreover, by inserting Eq. (53) in Eq. (52) the on-axis optical scintillation index of a Gaussian beam for a point receiver is [17]

$$\begin{aligned}\sigma_I^2 &= \exp\left(\sigma^2_{\ln X} + \sigma^2_{\ln Y}\right) - 1 \\ &= \exp\left\{\frac{0.49\sigma_B^2}{\left[1+0.56(1+\Theta)\sigma_B^{12/5}\right]^{7/6}} + \frac{0.51\sigma_B^2}{\left(1+0.69\sigma_B^{12/5}\right)^{5/6}}\right\} - 1.\end{aligned} \tag{59}$$

where σ_B^2 is the Rytov variance for a beam wave, given by Eq. (56).

For a receiving aperture with finite aperture D, the expression of the scintillation index is given by

$$\begin{aligned}\sigma_I^2(D) = 8\pi^2k^2L\int_0^1\int_0^\infty \kappa\Phi_n(\kappa)\exp\left(-\frac{L\kappa^2}{k(\Lambda+\Omega_G)}\left[(1-\overline{\Theta}\xi)^2+\Lambda\Omega_G\xi^2\right]\right) \\ \times\left(1-\cos\left[\frac{L\kappa^2}{k}\left(\frac{\Omega_G-\Lambda}{\Omega_G+\Lambda}\right)\xi(1-\overline{\Theta}\xi)\right]\right)d\kappa d\xi,\quad \Omega_G \geq \Lambda,\end{aligned} \tag{60}$$

where $\Omega_G = 2L/kW_G$ is a non-dimensional parameter defining the beam radius at the collecting aperture element. A tractable expression for Eq. (60) has been derived, based on the large-scale and small-scale variances [32]. Following the same strategy to deduce Eq. (59), and extending for finite apertures

$$\sigma_I^2(D) = \exp\left[\sigma^2_{\ln X}(D) + \sigma^2_{\ln Y}(D)\right] - 1. \tag{61}$$

where large-scale and small-scale log-irradiance variances are given by

$$\sigma^2_{\ln X}(D) = \frac{0.49\left(\frac{\Omega_G-\Lambda}{\Omega_G+\Lambda}\right)^2\sigma_B^2}{\left[1+\frac{0.4(2+\Theta)(\sigma_B/\sigma_R)^{12/7}}{(\Omega_G+\Lambda)\left(\frac{1}{3}-\frac{1}{2}\overline{\Theta}+\frac{1}{5}\overline{\Theta}^2\right)^{6/7}}+0.56(1+\Theta)\sigma_B^{12/5}\right]^{7/6}}, \tag{62}$$

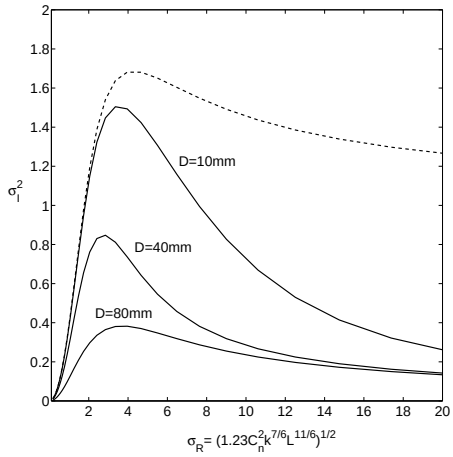

Figure 2.4 Scintillation index for different receiver aperture diameters. As reference the SI for a point receiver is shown (dashed line).

$$\sigma^2_{\ln Y}(D) = \frac{0.51\sigma_B^2(\Omega_G + \Lambda)\left(1 + 0.69\sigma_B^{12/5}\right)^{-5/6}}{\Omega_G + \Lambda + 1.20(\sigma_R/\sigma_B)^{12/5} + 0.83\sigma_R^{12/5}}. \tag{63}$$

It should be noticed that Eq. (59) and Eq. (61) do not account for effects induced by the inner and outer scale of turbulence. In oder to include them additional considerations must be made [See Appendix C].

In Fig. 2.4 a plot of the scintillation index is shown, where different receiving aperture diameters have been used to calculate Eq. (61), and a collimated Gaussian beam has been assumed with wavelength $\lambda = 780$ nm and beam size at the transmitter $W_0 = 1.13$ cm. Additionally, the effects of the inner scale and the outer scale limits of turbulence were neglected.

From the analysis of the Fig. 2.4 it can be concluded that a wireless optical communication link can be classified in one of three well differentiated zones. In the first one, regarded as the weak turbulence regime, the scintillation index increases monotonically as either the optical turbulence, denoted by the refractive-index structure parameter, or the link distance increases. Next, a peak in the scintillation index appears representing the point of maximum atmospheric turbulence. This zone is known as strong turbulence regime. Finally, a third zone called the saturation regime the value of the scintillation index settles to a plateau. The physical reason for the constant level of the SI, irrespective of the increase of the C_n^2 value or the link range, is because after a certain point the atmospheric turbulence completely breaks the spatial coherence of the traveling wavefront and the arriving optical wave behaves as a diffuse source. It becomes evident that the localization of the three turbulence regimes explained before is affected by the size of the receiving aperture size.

2.3.5.4 Aperture averaging

To counterbalance the scintillation effects on the optical link performance, it is desirable to have a large area at the detection plane in order to integrate as much light

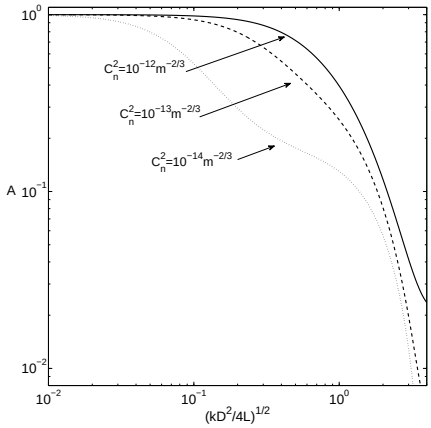

Figure 2.5 Aperture averaging factor for different atmospheric turbulence conditions as a function of the receiving aperture radius $D/2$ normalized to the Fresnel zone $\sqrt{L/k}$.

as possible. The received wavefront can be regarded as a self-interference pattern, produced by atmospheric inhomogeneities of different spatial scale sizes, that is averaged over the entire receiving area, thus, the intensity fluctuations are mitigated. From the ray optics point of view more rays, which all travel through distinct optical paths, can be collected by means of a lens to be integrated on the photodetector and the measured scintillation index will be lesser compared to that of a point receiver. This phenomenon, called aperture averaging, has been extensively addressed [20, 23, 24]. Churnside [23] developed simple closed-form expressions, to easily evaluate aperture averaging under weak fluctuation regime, that were later improved by Andrews [24]. More recently, an aperture averaging expression for Gaussian beams has been developed for the moderate-to-strong turbulence regime [17, 32].

The mathematical expression for the aperture averaging factor A is defined by

$$A(D) = \frac{\sigma_I^2(D)}{\sigma_I^2(0)}, \tag{64}$$

where $\sigma_I^2(0)$ is the SI for a point receiver defined in Eq. (59), while $\sigma_I^2(D)$ is the SI of a receiving aperture with diameter D given by Eq. (61). As far as experimental data is concerned an appropriate way to evaluate the aperture averaging factor is by using an effective point receiver, defined as an aperture much smaller than $\sqrt{\lambda L}$ and the inner scale size l_0 [45]. Note that the lowest possible value of A is desirable, in order to average out signal fluctuations due to atmospheric turbulence.

As it is seen from previous section, Eq. (64) is a rather complicated expression. Nevertheless, it is customary to assume the spherical wave as a good enough approximation for a Gaussian beam at the receiver plane for some rapid estimations [14]. The aperture averaging factor for a spherical wave has a fairly simple closed-

form expression given by [24]

$$A = \left[1 + 0.333 \left(\frac{kD^2}{4L}\right)^{5/6}\right]^{-7/5}, \tag{65}$$

where $k = 2\pi/\lambda$ is the wavenumber, D is the receiving aperture size, and L is the link distance.

In Fig. 2.5 the aperture averaging factor is shown for a Gaussian beam with the same characteristics of those used to plot Fig. 2.4. Additionally, a link distance of 2 km was set. It is clear that for higher turbulence strength the aperture averaging effect becomes less noticeable. Moreover, it is evident that the averaging capability of the receiver system increases as the receiving aperture diameter increases.

2.4 Propagation Simulation

Since its introduction by Fleck et al. [46] the beam split-step method has been widely used to simulate the propagation of electromagnetic waves, where the effects produced by the turbulent atmosphere are simulated by a series of linearly spaced random phase screens. In Fig. 2.6 are depicted the main aspects involved in the beam split-step method, also known as the *beam propagation method* (BPM). First, an initial traveling optical field is set and the path length L is split into a series of N steps, thus, dividing the optical path into N different slabs of turbulent atmosphere of width $\Delta z = L/N$. Each of these slabs is represented by a two-dimensional (2D) random phase screen placed in the middle of such slab. Consequently, the first and last propagation step have length $\Delta z/2$ while all other steps are Δz in length. The propagation of the optical field between every step takes place in the transformed domain, where the field is decomposed into a linear combination of plane waves. After each step the optical wavefront is inverse transformed, to the spatial domain, where a random phase screen is then used to simulate the atmosphere's effects. This process is repeated until the propagation path length is completed.

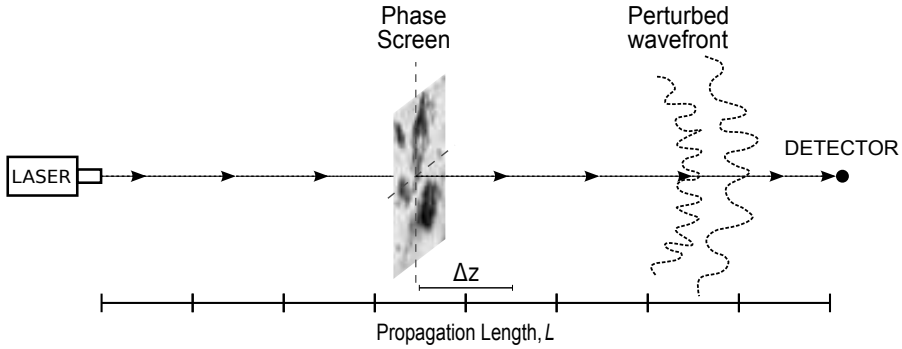

Figure 2.6 General scheme of beam propagation method (BPM) applied to the propagation of light through the turbulent atmosphere.

At the receiver end the detector is a single pixel in the case of a point receiver. When considering a finite size aperture, the optical power in the two-dimensional grid of the traveling wavefront is integrated over the aperture area.

The most widespread technique used to generate the random phase screens is based on the spectral method, in which phase screens are generated in the spectral domain with the selected turbulence power spectrum [47–49]. The fractal method is an alternative approach to reproduce the phase screens directly in the spatial domain by successive interpolations from a set of random numbers that obey the desired structure function associated with the turbulence power spectrum being used [50].

2.4.1 Spectral method

In this method the screens are numerically generated by the use of fast Fourier-transform and assumed to follow a particular turbulence power spectrum, where the most employed one is the Kolmogorov spectrum.

The phase screen is generated in the spectral domain by means of filtering Gaussian white noise with the selected turbulence power spectrum, then an inverse transformation yields the desired random phase screen in the spatial domain, which is given by [48]

$$\theta_s(j\Delta x, l\Delta y) = \sum_{n=0}^{N_x}\sum_{m=0}^{N_y}\left[a(n,m) + ib(n,m)\right] \times \exp\left[2\pi i(jn/Nx + lm/Ny)\right], \qquad (66)$$

where $i = \sqrt{-1}$; Δx and Δy are the grid spacing; N_x and N_y are the number of points in the respective dimension of the screen; and $a(n,m)$ and $b(n,m)$ are random numbers following Gaussian white noise statistics with

$$\langle a^2(n,m)\rangle = \langle b^2(n,m)\rangle = 2\pi k^2 \Delta z \frac{2\pi}{N_x \Delta x}\frac{2\pi}{N_y \Delta y}\Phi_n(\vec{\kappa}, \Delta z), \qquad (67)$$

where k is the wave number, $\Phi_n(\vec{\kappa}, \Delta z)$ is the two-dimensional power spectrum for refractive-index fluctuations as a function of the propagation step Δz, and $\vec{\kappa}$ is the spatial wave number vector in the plane transversal to propagation direction.

However, a major difficulty with this technique is to reproduce the atmospheric large-scale effects owing to the fact that they are related with lowest spatial frequencies of the turbulence spectrum, and, it is precisely around zero where the Kolmogorov spectrum has a singularity. This issue was addressed first by Lane et al. [50] with the addition of subharmonics components to the random phase screen, as a result of which more resolution in the spatial frequencies around zero is obtained. Later, an improved version of this method was introduced by Recolons and Dios [49].

2.4.2 Fractal method

Phase screens generated following a Kolmogorov power spectrum have an important property, namely, that they present a fractal behavior as they look similar regardless of the scale they are viewed. The firsts to propose the use of fractal interpolation for generating phase screens were Lane et al. [50], and later an improved version of this method was introduced [51].

With this method, first, an exact low-resolution phase screen is generated by evaluating its covariance matrix that is obtained directly from the structure function, which for a pure Kolmogorov spectrum—as it is normally assumed—, is given by

$$D(\vec{r_1},\vec{r_2}) = \langle[\theta_s(\vec{r_1}) - \theta_s(\vec{r_2})]^2\rangle = 6.88\left(\frac{|\vec{r_1}-\vec{r_2}|}{r_0}\right)^{5/3}, \tag{68}$$

where $\theta_s(\vec{r_1})$ and $\theta_s(\vec{r_2})$ are the phase evaluated at positions $\vec{r_1}$ and $\vec{r_2}$, respectively, and r_0 is the Fried parameter. The covariance matrix can be obtained from the structure function with the relationship

$$\begin{aligned} C_{\theta_s}(\vec{r_1},\vec{r_2}) \;=\; & -\frac{1}{2}D(\vec{r_1},\vec{r_2}) + \frac{1}{2}\iint D(\vec{r_1}',\vec{r_2})T(\vec{r_1}')dx_1'dy_1' \\ & +\frac{1}{2}\iint D(\vec{r_1},\vec{r_2}')T(\vec{r_2}')dx_2'dy_2' \\ & -\frac{1}{2}\iiiint D(\vec{r_1}',\vec{r_2}')T(\vec{r_1}')T(\vec{r_2}')dx_1'dy_1'dx_2'dy_2', \end{aligned} \tag{69}$$

where $T(\vec{r})$ is a windowing function that has a constant value inside the domain of the phase screens and zero value outside. Next, once the covariance matrix is obtained, an square matrix matching the size of the phase screen is generated from a set of Gaussian random numbers with variance given by the eigenvalues of $C_{\theta_s}(\vec{r_1},\vec{r_2})$ [51]. Nevertheless, it is important to note that if the initial squared phase screen has a size $N \times N$, then the covariance matrix has $N^2 \times N^2$ dimension, making the method applicable to small values of N. Thereby, the use of interpolation techniques rises as mandatory to obtain phase screen with higher resolution. Probably, the most widespread window sizes in the literature are $N = 512$ and $N = 1024$.

When the low-resolution phase screen has been completely generated, successive randomized interpolation steps are executed to produce the final desired grid size. This interpolation method helps to achieves high resolution screens while demanding a relatively small computational effort, although, having the drawback of poorer statistical performance.

2.5 Wireless Optical Communication Systems

Previous sections have been focused on the explanation of the physical phenomena that affect an optical traveling wave in free-space optical links. From the communication systems approach, there are other factors that become critical when evaluating the performance of a wireless optical communications link. A simplified scheme is shown in Fig. 2.7, where the main blocks in a FSO link are presented.

Wireless optical communications rely on a traveling wave generated by a laser source, at a certain average transmitted power level P_T. Aside from the effects suffered by the optical traveling wavefront through the turbulent atmospheric channel, addressed in Sec. 2.3, the average optical power at the receiver plane P_R is influenced by various parameters. The expression for the average optical power detected at a

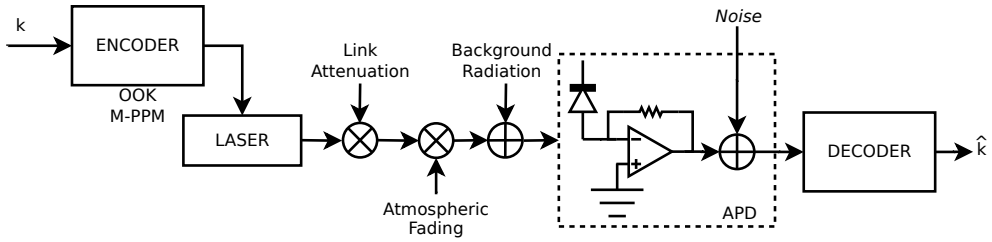

Figure 2.7 Block diagram for a free-space optical communication link.

distance R in a WOC link, is given by

$$P_R(R) = P_T \frac{D_R^2}{D_T^2 + (R\theta)^2} \exp\left(-\frac{\theta_{mp}^2}{(\theta/2)^2}\right) T_a(R) T_R, \tag{70}$$

where θ is the laser beam full-angle divergence, $T_a(R)$ is the transmittance of the atmosphere along the optical path, T_R is the transmittance of the receiver optics, θ_{mp} denotes pointing errors between the emitter and receiver, and, D_T and D_R are the transmitting and receiving aperture diameters, respectively. It should be noted that the pointing errors are not only due to misalignments in the installation process, but also to vibrations on the transmitter and receiver platforms. For horizontal links the vibration comes from transceiver stage oscillations and buildings sway caused by wind, while for vertical links—i.e. ground-satellite links— satellite wobbling oscillations are the main source of pointing errors.

2.5.1 Atmospheric attenuation

A laser beam traveling through the turbulent atmosphere is affected by extinction due to aerosols and molecules suspended in the air. The transmittance of the atmosphere can be expressed by Beer's law as

$$T_a(R) = \frac{P(R)}{P(0)} = e^{-\alpha_a R}, \tag{71}$$

where $P(0)$ is transmitted laser power at the source, and $P(R)$ is the laser power at a distance R. The total extinction coefficient per unit length α_a comprises four different phenomena, namely, molecular and aerosol scattering, and, molecular and aerosol absorption

$$\alpha_a = \alpha_{abs}^{mol} + \alpha_{abs}^{aer} + \beta_{sca}^{mol} + \beta_{sca}^{aer}. \tag{72}$$

The molecular and aerosol behavior for the scattering and absorption process is wavelength dependent, thus, some atmospheric windows appear where the transmission of certain optical wavelengths is more favored. The spectral transmittance of the atmosphere is presented in Fig. 2.8, for a horizontal path of nearly 2 km at mean sea level [52].

Within the atmospheric transmittance windows the molecular and aerosol absorption can be neglected. Molecular scattering is very small in the near-infrared,

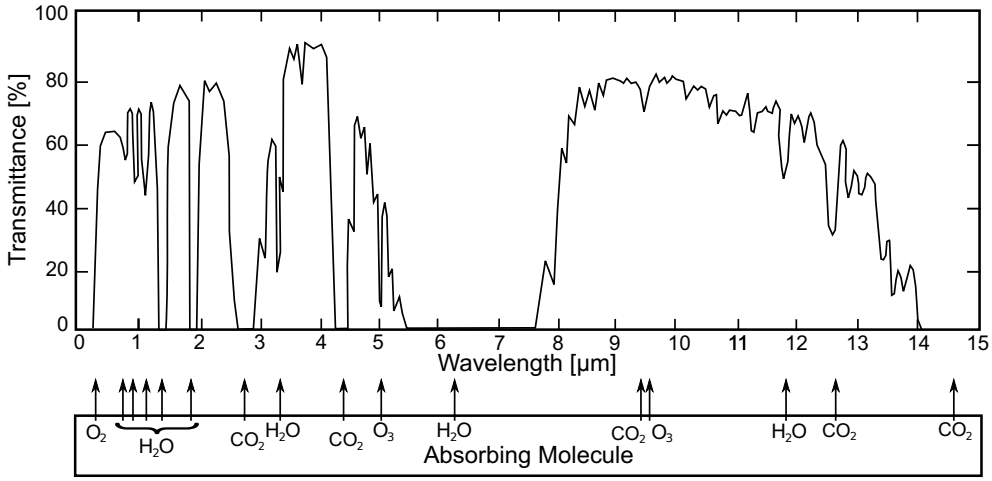

Figure 2.8 Earth's atmospheric transmittance (Adapted from Hudson [52]).

due to dependence on λ^{-4}, and can also be neglected. Therefore, aerosol scattering becomes the dominating factor reducing the total extinction coefficient to [53]

$$\alpha_a = \beta_{sca}^{aer} = \frac{3.91}{V}\left(\frac{\lambda}{550}\right)^{-q}, \tag{73}$$

where V is the visibility in kilometers, λ is the wavelength in nanometers, and q is the size distribution of the scattering particles. Typical values for q are given in Table 3 for high, average and low visibilities.

The attenuation factors that induce the larger penalties are the atmospheric attenuation and the geometrical spreading losses, both represented in Fig. 2.9. It becomes evident from the inspection of their respective behaviors, that the atmospheric attenuation imposes a larger attenuation for poor visibility conditions than the geometrical losses due to the beam divergence of the laser source. Meteorological phenomena as snow and haze are the worst obstacle to set horizontal optical links, and, of course, the clouds in vertical ground-satellite links, which impose the need of privileged locations for deploying the optical ground stations.

For the calculations in Fig. 2.9(a) a light source with wavelength $\lambda = 780$ nm was assumed, and for Fig. 2.9(b) the aperture diameter in transmission and reception was

Table 3 Value of the size distribution of the scattering particles q, for different visibility conditions.

Visibility	q
V >50km	1.6
6km< V <50km	1.3
V <6km	$0.585V^{1/3}$

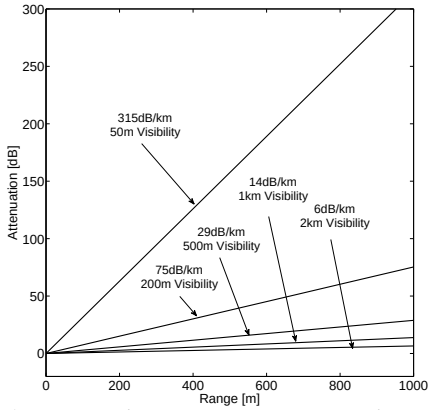

(a) Atmospheric attenuation in decibels for light source with $\lambda = 780$ nm and various visibility conditions.

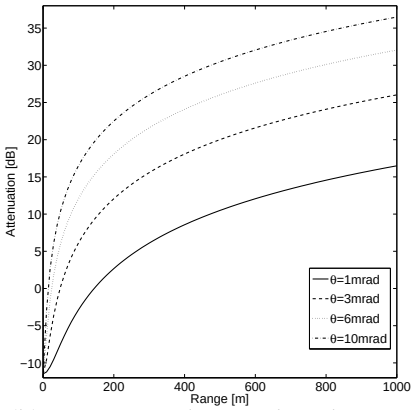

(b) Geometrical spreading loss in dB for various beam full-angle divergences.

Figure 2.9 Attenuation factor dependence on link distance.

set to 4 cm and 15 cm respectively. The negative values of the attenuation in Fig. 2.9(b) imply that the geometrical spreading of the transmitted beam, has not yet exceeded in size the receiving aperture.

2.5.2 Background radiance

In a wireless optical communication link the receiver photodetector is always subject to an impinging optical power, even when no laser pulse has been transmitted. This is because the sun radiation is scattered by the atmosphere, the Earth's surface, buildings, clouds, and water masses, forming a background optical power. The amount of background radiance detected in the receiver depends on the area and the field of view of the collecting telescope, the optical bandwidth of the photodetector, and weather conditions. The most straightforward method to decrease background radiation is by adding an interference filter with the smallest possible optical bandwidth, and the centered at a wavelength matching that of the laser source. Typical values of optical bandwidth these filters are in orders of a few nanometers.

The total background radiation can be characterized by the spectral radiance of the sky that depends on the elevation angle, and changes for day and night operation. In nighttime, the sky emissivity for a nearly horizontal path through the atmosphere is essentially that of a blackbody at the temperature of the lower atmosphere—e.g $8°$C in Fig. 2.10(a). The curves for daytime conditions will be very similar to those of nighttime, with the corresponding change due to higher temperatures, with the addition of scattered sun radiation below 3 μm [52]. The typical behavior of the spectral radiance of the sky is shown in Fig. 2.10(b) for daytime conditions and a horizontal path at noon.

Once the spectral radiance of the sky is known the total optical power at the re-

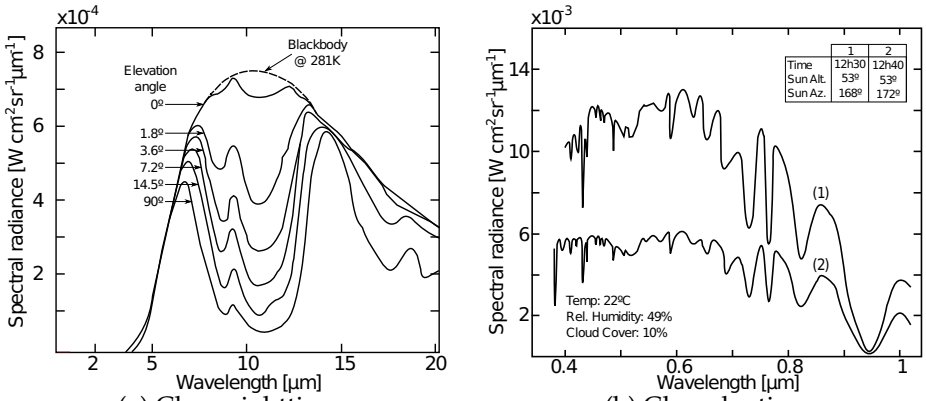

(a) Clear nighttime (b) Clear daytime

Figure 2.10 Spectral radiance of the sky for clear nighttime (Adapted from Bell et al. [54]) and clear daytime (Adapted from Knestrick and Curcio [55]).

ceiver, due to background, can be calculated by

$$P_B = N_B T_R \left(\pi \frac{D}{2} \frac{\text{FOV}}{2}\right)^2 B_{opt}, \tag{74}$$

where N_B is the background spectral radiance, FOV is the field of view of the receiving telescope, and B_{opt} is the optical bandwidth of the interference filter.

Following the method described by Bird and Riordan [56] an estimation of the diffuse irradiance, considering rural environment, for 830 nm would be between 60 and 100 $\text{Wm}^{-2}\mu\text{m}^{-1}$, depending on the elevation angle of the Sun during the day. These values respond to the irradiance received on the ground coming from the sky in all directions without considering the solar crown, and result of the same order that the values extracted from Fig. 2.10. Therefore, special care has to be taken from having direct sunlight into the telescope field of view, situation that may produce link outages due to saturation of the photodetector.

2.5.3 Probability density function for the received optical power

In any communication system the performance characterization is, traditionally, done by evaluating link parameters such as probability of detection, miss and false alarm; threshold level—for a hard-decoder—and fade probability, that demands knowledge of the probability density function (PDF) for the received optical power [14]. Actually, it is rather a difficult task to determine what is the exact PDF that fits the statistics of the optical power received through an atmospheric path.

Historically, many PDF distributions have been proposed to describe the random fading events of the signal-carrying optical beam, leading to power losses and eventually to complete outages. The most widely accepted distributions are the Log-Normal (LN) and the Gamma-Gamma (GG) models, although, many others have been subject of studies, such as the K, Gamma, exponential, I-K and the Lognormal-Rician distributions [57–59].

In the literature, although not always mentioned, the PDF distribution for the received optical power in a wireless link will be greatly influenced whether the receiver has a collecting aperture or it is just the bear photodetector, i.e., a point receiver. Experimental studies support the fact that the LN model is valid in weak turbulence regime for a point receiver and in all regimes of turbulence for aperture averaged data [58, 60]. On the other hand, the GG model is accepted to be valid in all turbulence regimes for a point receiver, nevertheless, this does not hold when aperture averaging takes place [12, 58].

The Log-Normal distribution is given by

$$f_I(I;\mu_{\ln I},\sigma^2_{\ln I}) = \frac{1}{I\sqrt{2\pi\sigma^2_{\ln I}}}\exp\left[-\frac{(\ln I-\mu_{\ln I})^2}{2\sigma^2_{\ln I}}\right], \quad I>0, \tag{75}$$

where $\mu_{\ln I}$ is the mean and $\sigma^2_{\ln I}$ is the variance of the log-irradiance, and they are related to the scintillation index σ_I^2 by

$$\mu_{\ln I} = \ln(\langle I\rangle) - \frac{\sigma^2_{\ln I}}{2}, \tag{76}$$

$$\sigma^2_{\ln I} = \ln\left(\sigma_I^2+1\right). \tag{77}$$

The Gamma-Gamma distribution is used to model the two independent contributions of the small-scale and large-scale of turbulence, assuming each of them is governed by a Gamma process. The GG distribution is then given by

$$f_I(I;\alpha,\beta) = \frac{2(\alpha\beta)^{\frac{\alpha+\beta}{2}}}{\Gamma(\alpha)\Gamma(\beta)} I^{\frac{\alpha+\beta}{2}-1} K_{\alpha-\beta}\left(2\sqrt{\alpha\beta I}\right), \quad I>0, \tag{78}$$

where $K_\nu(x)$ is the Macdonald function of order ν, defined in Eq. (B.2.1), and α and β are parameters directly related to the effects induced by the large-scale and small-scale scattering, respectively [59]. The parameters α and β are related to the scintillation index by

$$\sigma_I^2 = \frac{1}{\alpha}+\frac{1}{\beta}+\frac{1}{\alpha\beta}. \tag{79}$$

It is customary to normalize Eq. (75) and Eq. (78) in the sense that $\langle I\rangle = 1$. Under such assumption, the parameters α and β of the GG distribution can be related to the large-scale and small-scale scintillation, introduced in Sec. 2.3.5.3, in the form [32]

$$\alpha = \frac{1}{\sigma^2_X(D)} = \frac{1}{\exp[\sigma^2_{\ln X}(D)]-1}, \tag{80}$$

$$\beta = \frac{1}{\sigma^2_Y(D)} = \frac{1}{\exp[\sigma^2_{\ln Y}(D)]-1}. \tag{81}$$

2.6 Performance of Wireless Optical Communication

2.6.1 Intensity-modulation direct-detection

One of the fundamental technical decisions for a wireless optical communication systems is the choice of the modulation scheme. Although, many modulation techniques have been proposed, from non-coherent to coherent schemes, there is marked

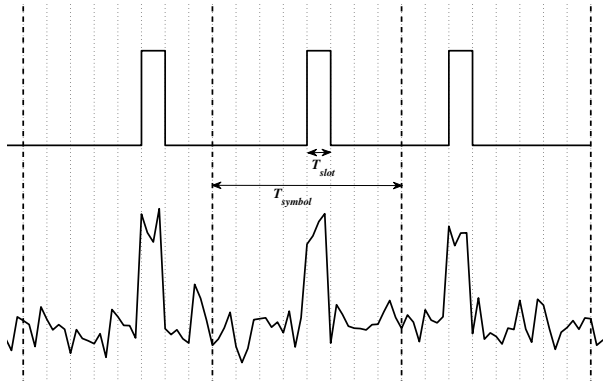

Figure 2.11 Binary sequence 101100010 encoded in 8-PPM (top) and same sequence corrupted by noise (bottom).

trend to favor the use of intensity-modulation direct-detection (IM/DD) scheme because it hides the high-frequency nature of the optical carrier thanks to its equivalent baseband model [61]. Another reason to prefer the IM/DD scheme is the relatively low design complexity of the receiver system, when comparing to coherent systems, and because the photodetector is many times larger than the optical wavelength it exhibits a high degree of immunity to multipath fading [62]. Among the most widespread intensity-modulation schemes for optical communications, there are the on-off keying (OOK) and pulse position modulation (PPM). Chan [63] noted that the PPM scheme is the most suitable for FSO owing to the fact that it does not rely on a threshold value to apply optimal detection.

The PPM format encodes L bits of information into one symbol, or word, of duration T_w that is divided in $M = 2^L$ slots, by transmitting power in only one out of the M possible slots. Therefore, PPM presents itself as an orthogonal modulation scheme. On the receiver side the maximum-likelihood detection is done by choosing the slot that contains the maximum count of photons—i.e. energy—, over a word time after synchronization has been achieved. The waveform for a set of bits encoded in 8-PPM before and after propagation is shown in Fig. 2.11.

A communication system based on PPM modulation groups the input bits, at the transmitter, in blocks of length $L = \log_2 M$, with bit rate R_b, to transmit them at a symbol rate of $R_w = 1/T_w = R_b/\log_2 M$, where T_w is the word or symbol time. Hence, the bandwidth required for transmitting data using M-PPM can be approximated by the bandwidth of a single pulse slot [61]

$$B \approx \frac{1}{T_p} = \frac{1}{T_w/M} = \frac{MR_b}{\log_2 M}, \tag{82}$$

where T_p is the pulse or slot time, and represents a higher requirement in bandwidth compared to that of an OOK modulation scheme, which is $B = R_b$. Table 4 shows the average power and bandwidth requirements for OOK and PPM modulation. The binary phase-shift keying and quadrature phase-shift keying with N subcarriers modulation schemes—BPSK and N-QPSK, respectively—are presented as reference.

On the other hand, regarding the average optical power required for achieving a certain bit error-rate (BER), a PPM waveform needs $1/\sqrt{0.5M\log_2 M}$ less power than OOK. Consequently, for a given bit rate and BER value PPM demands higher bandwidth and less average optical power, when comparing with OOK. Except for the special case of 2-PPM, where the power requirement is exactly the same as for OOK, while the bandwidth is double. Furthermore, many authors have proposed new modulations derived from PPM, in particular differential PPM (DPPM) [64], overlapping PPM (OPPM) [65], improved PPM (IPPM) [66] and multipulse PPM (MPPM) [67], aiming to overcome the excessive bandwidth requirements of PPM modulation.

Demodulating a PPM signal can be done using *hard-decoding* or *soft-decoding*. The latter is preferred as it requires, after slot and symbol synchronization have been achieved, to integrate the power on each slot within a frame and then choose the one with the largest power measure. This way the PPM is highly resistant to background noise and the receiver sensibility is increased with respect to the hard-decoding approach, where a simple threshold detector is used to decide if a pulse has been received.

As the information is conveyed in time for PPM modulation format, a critical issue is the synchronization procedure. Timing recovery of the slot and symbol clock become essential to correctly decode the received noisy waveform. Many strategies have been proposed to aid in the synchronization stage [68–70]. Moreover, variants of PPM have been introduced, such as half-pulse PPM [71] and digital pulse interval modulation (DPIM) [72], in order to simplify the synchronization process.

Table 4 Average power and bandwidth requirements for different modulation schemes for a given bit error-rate (Adapted from Barry [61]).

Modulation Scheme	Average power	Bandwidth
OOK	$P_{OOK} = \sqrt{N_0 R_b}\, erf^{-1}(BER)$	R_b
M-PPM	$\frac{1}{\sqrt{0.5M\log_2 M}} P_{OOK}$	$\frac{MR_b}{\log_2 M}$
BPSK	$\sqrt{2}P_{OOK}$	$2R_b$
N-QPSK	$\sqrt{2N}P_{OOK}$	R_b

2.6.2 Signal-to-noise ratio in an APD photodetector

Several terms of noise have to be taken into account for the evaluation of the signal-to-noise ratio (SNR) in an optical link. Some of them are characteristic of the photodetector device, as the noise associated to the dark current or the noise coming from the intrinsic gain physical mechanism. Other terms come from the amplifier electronics.

The usual expression for the SNR at the receiver output is

$$\text{SNR} = \frac{i_S^2}{\sigma_S^2 + \sigma_B^2 + \sigma_D^2 + \sigma_A^2 + i_n^2} \tag{83}$$

being i_S^2 the generated photocurrent, σ_S^2 the shot noise associated to the received signal, σ_D^2 the dark current noise, σ_B^2 the noise coming from the background optical

power, i_n^2 the thermal noise and σ_A^2 the total equivalent noise input current associated to the amplifier. The photocurrent is calculated as follows

$$i_S = \eta e G \frac{\lambda P_S}{hc} \tag{84}$$

where η is the quantum efficiency, P_S is the received signal optical power, h is the Planck's constant, e is the electron charge, c is the speed of light in vacuum and G is the photo-detector intrinsic gain. The photocurrent can also be expressed by

$$i_S = R_I P_S, \tag{85}$$

where R_I is the current responsivity,

$$R_I = \eta e G \frac{\lambda}{hc} \quad \left[\frac{\mathrm{A}}{\mathrm{W}}\right]. \tag{86}$$

2.6.2.1 Noise sources

To complete the characterization of the signal-to-noise ratio an analysis of the noise sources in the APD has to be done. Some noise terms depend directly on the photodetector physical characteristics, while others are generated by the optical power illuminating the surface of the APD.

The process that detects the optical power impinging on the detector's surface is described by the occurrence of independent random events, modeled by the Poisson distribution, as an optical wave is ultimately formed by *photons* carrying quantized amounts of energy. This randomness in the detection process of any photon illuminating the APD, is what gives rise to the *shot noise* and *background noise*. The shot noise is given by

$$\sigma_S^2 = 2 e i_S B G F = 2 e (R_I P_S) B G F \tag{87}$$

and the background noise by

$$\sigma_B^2 = 2 e i_B B G F = 2 e (R_I P_B) B G F \tag{88}$$

where B is the electrical bandwidth, P_B is the background optical power, and F the excess noise factor. For a PIN photodiode this excess noise factor is the unity, as no internal gain exists. For an APD the general expression is

$$F = k_{eff} G + (1 - k_{eff}) \left(2 - \frac{1}{G}\right), \tag{89}$$

where k_{eff} is the carrier ionization ratio, for which 0.01–0.1 is the typical range of values.

Every photodetector, whether it is a PIN diode or an APD, generates a drift current even when no photons are entering the detector surface. This phenomena is due to the random generation of electron-holes pairs within the depletion area, and charges are attracted by the electric field produced by the polarization voltage. The dark current is the result of two current terms, and it is defined by

$$i_D = i_{DS} + i_{DB} G, \tag{90}$$

where i_{DS} is the surface leakage current, and i_{DB} the bulk noise current (for gain unity). The second term is a function of the gain, as it is affected by the avalanche process. The corresponding noise term is

$$\sigma_D^2 = 2e\left(i_{DS} + i_{DB}G^2F\right)B. \tag{91}$$

In an actual system the photodetector is always followed by an amplifier in order to adequate the signal to next stages, in the receiver chain. The amplifier noise is characterized by means of two noisy sources at the input, namely, an equivalent noise voltage source and an equivalent noise current source. The values of these sources appear as two parameters of the amplifier in the datasheet provided by the manufacturer, most of times even with plots showing their behavior as a function of the modulated signal frequency. A first approximation to the total equivalent noise current of the amplifier can be written as

$$\sigma_A^2 = \left(i_{nA}^2 + \frac{e_{nA}^2}{R^2}\right)B, \tag{92}$$

being R the feedback resistor in the transimpedance amplifier scheme, i_{nA} the amplifier equivalent noise current density, in $\mathrm{A}/\sqrt{\mathrm{Hz}}$, and e_{nA} the amplifier equivalent noise voltage density, in $\mathrm{V}/\sqrt{\mathrm{Hz}}$.

Finally, as in any electronic system there will always exist thermal noise, defined by

$$i_{nR}^2 = \frac{4KTB}{R}, \tag{93}$$

where K is the Boltzmann's constant and T is the absolute temperature in Kelvins.

Normally the manufacturer gives the *noise equivalent power* (NEP), a characteristic noise figure of the photo-detector. This is defined as the minimum optical signal that could be detected by the device, where *minimum signal* is understood as the signal power level for which the SNR equals unity. For a bare APD the NEP is limited by the dark current, whereas for a complete photodetector module other terms must be included, namely, the electronic and the thermal noise. Moreover, it is a common practice to give that parameter for 1 Hz bandwidth, i.e., normalized with respect to the bandwidth which may vary from one application to another. The NEP for a complete photodetector (APD plus preamplifier) is given by

$$\mathrm{NEP} = \left.\frac{P_S}{\sqrt{B}}\right|_{\mathrm{SNR}=1} = \frac{1}{R_I}\sqrt{\frac{1}{B}(\sigma_D^2 + \sigma_A^2 + i_n^2)} \quad \left[\frac{\mathrm{W}}{\sqrt{\mathrm{Hz}}}\right] \tag{94}$$

By using this figure of merit the evaluation of the noise can be abbreviated, as there is no need to calculate all of the terms of noise involved in it. Therefore, the SNR calculation only implies the knowledge of the signal and background power, along with the photodetector NEP, thus

$$\mathrm{SNR} = \frac{i_s^2}{\sigma_s^2 + \sigma_B^2 + R_I^2\mathrm{NEP}^2B}. \tag{95}$$

2.6.3 Bit error-rate performance

In digital communication systems, reliability is commonly expressed as the probability of bit error, best known as bit error-rate (BER), measured at the output of the receiver and depends directly on the received signal level and receiver noise level. The smaller the BER, the more reliable the communication system.

In order to obtain an accurate calculation of the BER, it is necessary to know the probability density function of the receiver output signal. In the case of WOC systems the APD is the preferred choice as photodetector. The output of an APD is modeled by the McIntyre-Conradi distribution [73], although, the Gaussian approximation is sufficient enough when the bulk current is of the order of nanoamperes and the absorbed photons are more than a few hundred within an observation time [74, 75].

For the output of a wireless optical communication link, with an APD as photodetector, there are two possibilities, namely, that a pulse is transmitted or not. In the former situation the APD is detecting optical power corresponding to the signal level and the background radiation, while in the latter only background radiation is received. Assuming a Gaussian distribution given by

$$f(x;\mu,\sigma^2) = \frac{1}{\sqrt{2\pi\sigma^2}} \exp\left[-\frac{(x-\mu)^2}{2\sigma^2}\right], \tag{96}$$

the average current μ_1 and its associated current noise σ_1^2 generated at the APD's output when a pulse has been transmitted are

$$\mu_1 = eG\frac{\eta}{h\nu}(P_S + P_{BG}) + i_{DS} + i_{DB}G, \tag{97}$$

$$\sigma_1^2 = 2B\left(\frac{e^2\eta}{h\nu}FG^2(P_S + P_{BG}) + \frac{2KT}{R_L} + e(i_{DS} + i_{DB}G^2F)\right). \tag{98}$$

On the other hand, when no pulse is transmitted the average current μ_0 and its associated current noise σ_0^2 are

$$\mu_0 = eG\frac{\eta}{h\nu}(\epsilon P_S + P_{BG}) + i_{DS} + i_{DB}G, \tag{99}$$

$$\sigma_0^2 = 2B\left(\frac{e^2\eta}{h\nu}FG^2(\epsilon P_S + P_{BG}) + \frac{2KT}{R_L} + e(i_{DS} + i_{DB}G^2F)\right), \tag{100}$$

where ϵ denotes the laser extinction ratio, generating residual light even when no pulse is being transmitted. All other parameters in Eqs. (97)–(100) were presented in Sec. 2.6.2.1.

2.6.3.1 Probability of error for on-off keying modulation

The simplest signaling format in a digital wireless optical communication system is the on-off keying (OOK), where a binary '1' is represented by a pulse while a binary '0' is represented by the absence of a pulse. The receiver, in this case, is comprised of a threshold detector for deciding which symbol has been received. Assuming that the receiver output noise follows a white Gaussian model, the corresponding PDFs for the cases of a pulse and no pulse being transmitted are shown in Fig. 2.12, where

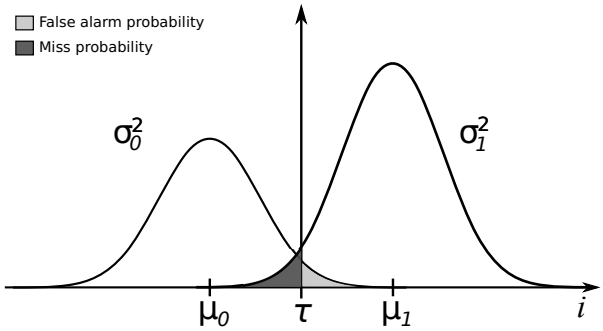

Figure 2.12 Received signal PDF under white Gaussian noise assumption.

τ represents the threshold level applied for comparison, and, the mean and variances are defined in Eqs. (97)–(100).

Let us consider now the word-error probability (PWE), which is compound of two types of errors. If the received signal level is higher than the set threshold τ when no pulse has been transmitted by the source, a false alarm is produced. On the contrary, if a pulse indeed has been transmitted and the received signal level is lower than τ, then, a missed event is generated. Thus, the PWE is given by

$$\text{PWE} = P_{\text{FA}} P_0 + P_{\text{Miss}} P_1, \tag{101}$$

$$P_{\text{FA}} = Q\left(\frac{\tau - \mu_0}{\sigma_0}\right), \tag{102}$$

$$P_{\text{Miss}} = 1 - Q\left(\frac{\tau - \mu_1}{\sigma_1}\right) = Q\left(\frac{\mu_1 - \tau}{\sigma_1}\right). \tag{103}$$

where P_{FA} denotes the probability of false alarm, P_{Miss} is the probability of miss, and $Q(x)$ is the Gaussian Q-function defined as

$$Q(x) = \frac{1}{2\pi} \int_x^\infty e^{-x^2/2} dx. \tag{104}$$

Whenever an equiprobable signaling system is used, the probability of receiving a pulse or not are equal, this is $P_0 = P_1 = 1/2$. For OOK modulation, the bit-error probability P_b is the same as the word-error probability—i.e. $P_b = \text{PWE}$.

The problem of defining the optimum threshold level has been addressed before, and the expression for τ in a maximum-likelihood receiver yields [75]

$$\left(\frac{\sigma_1^2}{\sigma_0^2} - 1\right)\tau^2 + 2\left(\mu_1 - \frac{\sigma_1^2}{\sigma_0^2}\mu_0\right)\tau - \sigma_1^2 \ln\left(\frac{\sigma_1^2}{\sigma_0^2}\right) + \frac{\sigma_1^2}{\sigma_0^2}\mu_0^2 - \mu_1^2 = 0. \tag{105}$$

Nevertheless, as real-time calculation of the mean and variance of the received signal is rather a complex task, a reasonable approach is to set the threshold level to half of the signal average amplitude, which actually approaches the optimum value of τ for high SNR values.

2.6.3.2 Probability of error for M-ary pulse position modulation

Pulse position modulation is a signaling format well suited for laser applications, requiring low average power and is very resistant to background radiation. In M-ary PPM signaling, L binary source bits are transmitted as a single light pulse in one out of $M = 2^L$ possible time slots, once every T_w seconds.

A maximum-likelihood APD based receiver, using M-PPM modulation, has a word-error probability given by [76]

$$\text{PWE} = 1 - \int_{-\infty}^{\infty} \sqrt{\frac{\gamma}{\beta+\gamma}}\phi\left(\sqrt{\frac{\gamma}{\beta+\gamma}}\left(x-\sqrt{\beta}\right)\right)\Phi(x)^{M-1}dx, \tag{106}$$

where $\phi(x)$ is given by Eq. (96) with zero mean and unitary variance, $\Phi(x)$ is the standard Gaussian cumulative distribution function, $\beta = (\mu_1 - \mu_0)^2/\sigma_0^2$ is the symbol signal-to-noise ratio, and, $\gamma = (\mu_1 - \mu_0)^2)/(\sigma_1^2 - \sigma_0^2)$.

In a different approach, a threshold detector can be implemented for demodulating PPM signals. Although, it is not the optimum strategy it can greatly simplify the receiver design, as tight synchronization requirements have not to be pursued as for the optimum receiver. The expression for the word-error probability for a threshold receiver has been derived by Moreira et al. [77], leading to

$$\text{PWE} = 1 - \left[P_1 + \frac{1}{M}P_2 + \sum_{n=2}^{M}\frac{1}{n}P_{3n}\right], \tag{107}$$

where P_1 is the probability of detecting a pulse in the correct position, P_2 is the probability of that no pulse is detected and P_{3n} is the probability of detecting n pulses. These probabilities are defined by

$$\begin{aligned} P_1 &= (1 - P_{\text{Miss}})(1 - P_{\text{FA}})^{M-1} \\ P_2 &= P_{\text{Miss}}(1 - P_{\text{Miss}})^{M-1} \\ P_{3n} &= \binom{M-1}{n-1}(1 - P_{\text{Miss}})P_{\text{FA}}^{n-1}(1 - P_{\text{FA}})^{M-1} \end{aligned} \tag{108}$$

where P_{FA} and P_{Miss} are given by Eq. (102) and Eq. (103), respectively.

Sometimes having the error probability at bit level is desirable. Thus, for a M-ary orthogonal signaling system, the probability of word error can be converted to bit-error probability according to [78]

$$P_b = \frac{M/2}{M-1}\text{PWE} \tag{109}$$

2.6.4 Bit error-rate under atmospheric turbulence

In the presence of optical turbulence, the probability of error is a conditional probability owing to the random nature of the received optical power. Thus, the SNR becomes a random variable and consequently the PWE has to be averaged over all the possible received optical signal levels, according to the proper statistical distribution model of the irradiance I. This yields

$$PWE(\sigma_I^2) = \int_0^{\infty} f_I(I;\sigma_I^2)PWE(I)dI, \qquad I > 0, \tag{110}$$

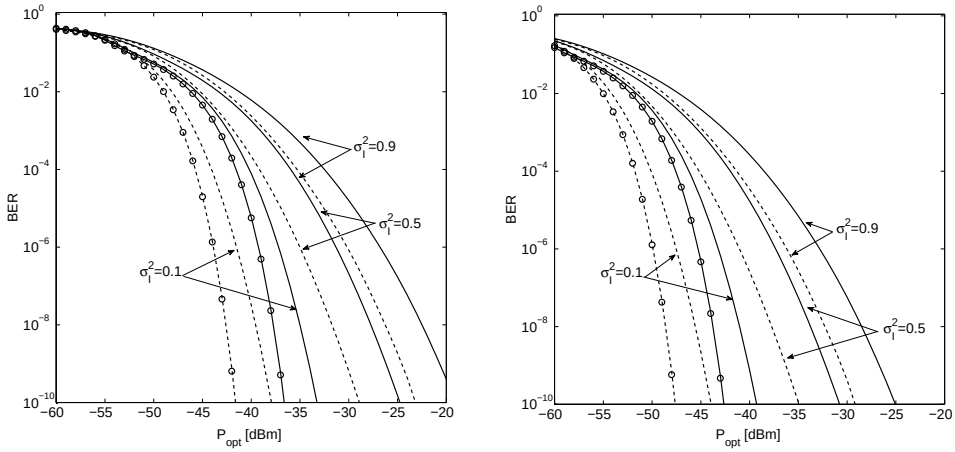

(a) Performance of OOK modulation. (b) Performance of 8-PPM modulation.

Figure 2.13 BER performance vs received optical power, with IM/DD, for fixed threshold (solid line) and optimum threshold (dashed line) receivers. No-turbulence (circles) is presented for reference.

where σ_I^2 is the scintillation index defined in Sec. 2.3, which depends directly on link's parameters such as C_n^2, link distance, laser divergence, and aperture averaging among others.

As stated in Sec. 2.5.3 the Log-Normal model is the most accepted in weak turbulence regimes for receiver points, and in all regimes of turbulence when aperture averaging takes place. Under weak turbulence regime the scintillation index, given by Eq. (52), can be expressed as

$$\sigma_I^2 \cong \sigma_{\ln I}^2, \tag{111}$$

and normalizing the irradiance in the sense that $\langle I \rangle = 1$, Eq. (75) reduces to

$$f_I(I) = \frac{1}{I\sqrt{2\pi\sigma_I^2}} \exp\left[-\frac{\left(\ln I + 0.5\sigma_I^2\right)^2}{2\sigma_I^2}\right]. \tag{112}$$

Some examples of the performance of a wireless optical communication system, with intensity-modulation and direct-detection, for OOK and PPM modulation with fixed and optimum threshold are shown in Figs. 2.13(a) and (b), respectively, and for different levels of scintillation index. It should be noted that the SI includes all the parameters such as laser wavelength and beam divergence, aperture averaging, the refractive-index structure parameter, link distance, transmitting and receiving aperture diameters, among others. It is readily seen, from Fig. 2.13, the tremendous impact of atmospheric turbulence in wireless optical communication systems regardless of the modulation scheme being used, although, a PPM system in general performs better than OOK with respect to the average optical power needed for achieving a desired bit error-rate level. For example, both for OOK and 8-PPM, there is roughly a 7 dB power penalty for a BER $= 10^{-6}$ with fixed threshold receiver (solid lines) and $\sigma_I^2 = 0.5$ with respect to the case of no turbulence, i.e. free-space conditions.

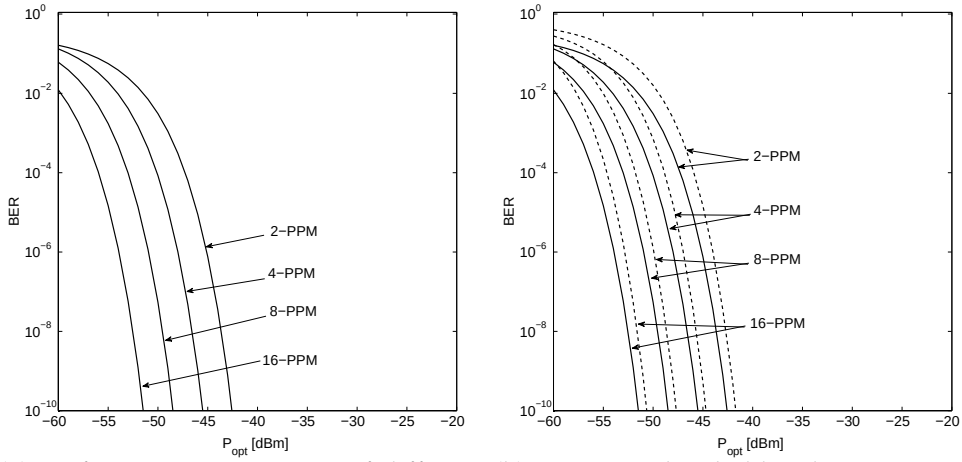

(a) Performance comparison of different orders of PPM modulation.

(b) Optimum threshold and maximum-likelihood receiver.

Figure 2.14 Performance of a PPM optimal threshold receiver (dashed line) and maximum-likelihood receiver (solid line) vs received average optical power under no-turbulence conditions.

Figure 2.14 is presented for a more comprehensive analysis of a pulse position modulation receiver. The performance of PPM maximum-likelihood receiver with modulation orders up to 16 is shown in Fig. 2.14(a), where it becomes evident that when increasing the PPM modulation order to the next permitted one there is an improvement of 3 dB with respect to the average optical power needed to achieve a certain BER. Figure 2.14(b) is presented as a mean of comparison between the performance of a maximum-likelihood receiver and an optimum threshold receiver for PPM modulation. The penalty incurred for using the optimum threshold receiver instead of the maximum-likelihood receiver is about 1 dB for BER $< 10^{-4}$. Nevertheless, this penalty increases for higher values of bit error-rate, although, a typical communication system with no forward error correction (FEC) code implemented will be designed to have a BER lower than 10^{-4}.

For the calculations in Fig. 2.13 and Fig. 2.14 background radiation was omitted in the analysis and it was assumed an APD's current gain $G = 70$, carrier ionization ratio $k_{eff} = 0.094$, quantum efficiency $\eta = 0.77$ and NEP $= 55$ fW/Hz. The light source was set to $\lambda = 780$ nm, pulse time $T_p = 1$ ns and extinction ratio $\epsilon = 0.001$.

3

The Exponentiated Weibull Fading Channel: An Alternative

THIS CHAPTER is focused on presenting the new proposed exponentiated Weibull (EW) fading channel model, the development of its physical justification, and the derivation of expressions for the parameters governing the EW distribution. Simulation and experimental data are used to assess its suitability to model the PDF of irradiance data in FSO links. Moreover, data previously published by other authors are used for completeness of the analysis.

3.1 Introduction

For many decades the scientific community, dedicated to the study of the atmospheric turbulence effects in free-space optical (FSO) communication link, has been in the search for a probability density function (PDF) capable to model the fluctuations of the signal-carrying laser beam intensity. Many distributions have been proposed over the years, all with different degrees of success. Historically, the models that drawn more attention were the lognormally modulated Rician distribution—also known as the Beckmann distribution—[10], the lognormally modulated exponential distribution [11], and the I-K distribution introduced by Andrews and Phillips [79] as a generalization of the well-known K distribution [13]. But, nowadays, the two most widely accepted models are the Lognormal (LN) and Gamma-Gamma (GG) distributions [12].

The major difficulty continues to be finding a single distribution to model the PDF of the irradiance fluctuations, valid in all regimes of turbulence strength and under all aperture averaging conditions. Many authors report that the LN model is valid in weak turbulence regime for a point receiver and works well in all regimes of turbulence for aperture averaged data [58, 60]. On the other hand, the GG model is accepted to be valid in all turbulence regimes for a point receiver, nevertheless, the GG model does not hold when aperture averaging takes place [12, 58, 59].

Nowadays, the search for a distribution capable of accurately model the PDF of irradiance data under all conditions of atmospheric turbulence in the presence of aperture averaging still drives a large amount of theoretical work, as well as efforts in simulation and experimental work.

Herein, the exponentiated Weibull (EW) distribution [80] is presented as an alternative model to describe the distribution of the irradiance PDF in FSO links. This distribution was first introduced by Mudholkar & Srivastava [81] as a generalization of the well-known Weibull distribution, with the addition of an extra shape parameter. The Weibull distribution—initially appearing in the field of reliability engineering [82]—has been extensively used in physics and engineering to model the wind speed distribution [83], particles size distribution [84], a specific type of clutter [85], and, in wireless communications where some channels are modeled with Weibull fading [86–88]. Moreover, very recently Chatzidiamantis et al. [89] proposed a double-Weibull process, to describe the PDF of the optical irradiance fluctuations, in the moderate-to-strong turbulence regime.

The next section covers a brief explanation of the classic FSO fading channel models based on the Lognormal and Gamma-Gamma distributions. In Sec. 3.3 the proposed exponentiated Weibull fading channel model is introduced, departing from physical assumptions, and Sec. 3.4 provides expressions to estimate its distribution parameters directly from atmospheric parameters. Section 3.5 is devoted to assess the suitability of the EW model with simulation results and experimental data. Moreover, Sec. 3.6 extends the analysis using already published data by other authors. The study conducted for every scenario includes a direct comparison of the exponentiated Weibull distribution with the LN and GG models. A detailed explanation of the mathematical derivation of each fading model presented in this chapter can be found in Appendix D.

3.2 Classic FSO Fading Models

In this section the two most widely accepted models the Lognormal and Gamma-Gamma distributions are introduced, including the physics behind their appearance in FSO fading channels. For both models the probability density function and the cumulative distribution function (CDF) are presented. Furthermore, the expressions to deduce their corresponding distribution parameters in terms of atmospheric parameters, through the scintillation index, are also given.

3.2.1 Lognormal fading

The lognormal distribution is the most commonly used PDF under weak irradiance fluctuations. To derive this model the first-order Rytov approximation is used to express the irradiance of an optical wave traveling in atmospheric turbulence as

$$I = \exp\left(2\chi_1\right), \tag{1}$$

where $\chi_1 = \frac{1}{2}\left(\psi_1 + \psi_1^*\right)$ is the first-order log-amplitude of the the field, and ψ_1 is the first-order phase perturbation term in the Rytov approximation [See Eq. (29) in Chapter 2]. By definition the log-amplitude χ_1 is Gaussian distributed [90, p. 65], and by making the transformation of variables $\chi_1 = \frac{1}{2}\ln(I)$, and using standard statistical procedures, the PDF of the irradiance can be obtained as [91, Appx. B.1]

$$f_I(I) = \frac{1}{I\sqrt{2\pi\sigma_{\ln I}^2}} \exp\left[-\frac{\left(\ln I + \frac{1}{2}\sigma_{\ln I}^2\right)^2}{2\sigma_{\ln I}^2}\right], \tag{2}$$

where the irradiance is normalized in the sense that $\langle I \rangle = 1$, and the variance of the log-irradiance $\sigma_{\ln I}^2$ is related to the scintillation index (SI) by [9, p. 293]

$$\sigma_{\ln I}^2 = \ln\left(\sigma_I^2 + 1\right). \tag{3}$$

The cumulative distribution function of a random variable I described by the Lognormal distribution is defined by

$$F_I(I) = \frac{1}{2} - \frac{1}{2}\operatorname{erf}\left[\frac{\ln I - 0.5\sigma_{\ln I}^2}{\sqrt{2\sigma_{\ln I}^2}}\right]. \tag{4}$$

Recently it has been suggested that the PDF of the irradiance fluctuations in weak turbulence is not truly Lognormal, when the second-order phase perturbation term is accounted for in the Rytov approximation [92], resulting in a skewed LN distribution. Experimental results [57] and simulation data [57, 93] seem to support this claim.

3.2.2 Gamma-Gamma fading

In order to find a PDF capable of modeling the irradiance fluctuations in the weak-to-strong turbulence regime many distributions have been proposed before [10, 13, 79].

But, the most accepted model to date is the Gamma-Gamma distribution first proposed by Al-Habash et al. [12]. This heuristic model was developed under assumption that the resulting irradiance fluctuations are due to a modulation process between the large-scale X and small-scale Y irradiance

$$I = XY, \tag{5}$$

where X and Y are independent identically distributed (i.i.d.) Gamma random variables.

Note that a Gamma random variable X can be derived as the summation of m negative exponential (NE) variates as

$$X = \sum_{j=1}^{m} X_j, \tag{6}$$

where $X_1, X_2, \ldots, X_m$ are i.i.d. negative exponential variates. Recall that a NE distribution is obtained by assuming that the received optical field is a zero mean circular complex Gaussian random field $U = u + iv$, with variance σ^2; where $i^2 = -1$. Then, the irradiance $X_j = |U|^2 = u^2 + v^2$ of such optical wave follows a negative exponential distribution [See Appendix D.2].

Through standard statistical procedures and setting $m = \alpha$, where α is a real valued parameter, it can be proved that the PDF of the variate X, described by Eq. (6), is given by [See Appendix D.3]

$$f_X(x) = \frac{\alpha(\alpha x)^{\alpha-1}}{\Gamma(\alpha)} \exp\left(-\alpha x\right), \tag{7}$$

where $\Gamma(\cdot)$ is the gamma function, defined in Eq. (B.1.1).

Now, knowing that the PDF of the large-scale X and small-scale Y irradiances are both described by Eq. (7), then the probability density function of a double stochastic process with variate I, defined by Eq. (5), yields

$$f_I(I;\alpha,\beta) = \frac{2(\alpha\beta)^{\frac{\alpha+\beta}{2}}}{\Gamma(\alpha)\Gamma(\beta)} I^{\frac{\alpha+\beta}{2}-1} K_{\alpha-\beta}\left(2\sqrt{\alpha\beta I}\right), \quad I > 0, \tag{8}$$

where $K_\nu(x)$ is the Macdonald function of order ν, defined in Eq. (B.2.1), and α and β represent the effective number of large-scale and small-scale eddies. In Appendix D.4 a detailed derivation of the Gamma-Gamma distribution is presented.

The parameters of the GG distribution can be related to the large-scale and small-scale scintillation, introduced in Sec. 2.3.5.3, in the form

$$\alpha = \frac{1}{\sigma_X^2(D)} = \frac{1}{\exp(\sigma_{\ln X}^2(D)) - 1}, \tag{9}$$

$$\beta = \frac{1}{\sigma_Y^2(D)} = \frac{1}{\exp(\sigma_{\ln Y}^2(D)) - 1}. \tag{10}$$

Moreover, the parameters α and β are related to the scintillation index by

$$\sigma_I^2 = \frac{1}{\alpha} + \frac{1}{\beta} + \frac{1}{\alpha\beta}. \tag{11}$$

The CDF of a random variable I having the Gamma-Gamma distribution is defined by [12]

$$F_I(I;\alpha,\beta) = \frac{\pi \csc(\pi(\alpha-\beta))}{\Gamma(\alpha)\Gamma(\beta)} \left[\frac{(\alpha\beta I)^{\beta}}{\beta\Gamma(\beta-\alpha+1)} {}_1F_2(\beta;\beta+1,\beta-\alpha+1;\alpha\beta I) - \frac{(\alpha\beta I)^{\alpha}}{\alpha\Gamma(\alpha-\beta+1)} {}_1F_2(\alpha;\alpha+1,\alpha-\beta+1;\alpha\beta I) \right], \quad (12)$$

where $\csc(x) = 1/\sin(x)$; and ${}_1F_2(\cdot)$ is a generalized hypergeometric function, defined in Eq. (B.3.1) .

The GG model has been proved to provide good fits to both simulation results and experimental data in the weak-to-strong turbulence regime [59, 86, 91, 94, 95]. Nevertheless, data suggests that the GG model is not capable of accurately reproduce the PDF of irradiance fluctuations when aperture averaging takes place [14, 94].

3.3 New Fading Model

After formally presenting the Lognormal and Gamma-Gamma models in FSO fading channels, here a new model is proposed aiming to describe the irradiance fluctuations in free-space optical links, resulting in the exponentiated Weibull distribution. The reasoning followed to derive such model is a combination of previous proposals by other authors, plus particular assumptions added. Similar physical assumptions to those used to derive the exponentiated Weibull model can be found in the work of Yacoub [96], Abdi et al. [97] and Jurado-Navas et al. [98].

First, a simple fading channel model is derived based on the Weibull distribution. Finally, this simple model is extended to a more versatile one resulting in the exponentiated Weibull fading channel model for free-space optical communications.

3.3.1 Weibull fading

Let us first assume a very simple fading model. An optical wave propagating in the turbulent atmosphere, can be regarded as a circular complex Gaussian random field $U = X_1 + iX_2 = X\exp(-i\varphi)$ [88]. Considering that X_1 and X_2 are zero-mean Gaussian processes with variance σ^2, then, the random phase $\varphi = tan^{-1}(X_2/X_1)$ is uniformly distributed in $[0, 2\pi)$, and the amplitude of the optical wave $X = \sqrt{X_1^2 + X_2^2}$ is Rayleigh distributed, with probability density function [See Appendix D.2]

$$f_X(x;\Omega) = \frac{2x}{\Omega}\exp\left(-\frac{x^2}{\Omega}\right), \quad (13)$$

where $\Omega = E[x^2]$ is a scale parameter; and $E[\cdot]$ denotes the expected value. Now let the received irradiance to be obtained from a nonlinear function of the squared modulus of the wave's amplitude X. Such a nonlinearity is manifested in terms of a power parameter $\beta > 0$, so that the received signal intensity is the result of not simply the squared modulus of X, but this squared modulus to a certain power [96]. Therefore, the received random signal is $Y = U^{2/\beta} = X^{2/\beta}\exp(-i2\varphi/\beta)$, and the

corresponding PDF of the irradiance $I = X^{2/\beta}$ follows a Weibull distribution defined as

$$f_I(I;\beta,\eta) = \frac{\beta}{\eta}\left(\frac{I}{\eta}\right)^{\beta-1} \exp\left[-\left(\frac{I}{\eta}\right)^{\beta}\right], \tag{14}$$

where $\beta > 0$ is a shape parameter, and $\eta > 0$ is a scale parameter, that depends on β, and is related to the mean value of the irradiance. For the special cases of $\beta = 2$ and $\beta = 1$, Eq. (14) reduces to the Rayleigh and negative exponential PDF, respectively.

The cumulative distribution function of a random variable I having the Weibull distribution is defined by

$$F_I(I;\beta,\eta) = 1 - \exp\left[-\left(\frac{I}{\eta}\right)^{\beta}\right]. \tag{15}$$

It is easily proved that the n-th irradiance moment of the Weibull PDF is given by [See Appendix D.5.1]

$$\langle I^n \rangle = \eta^n \Gamma\left(1 + \frac{n}{\beta}\right), \tag{16}$$

where the brackets $\langle \cdot \rangle$ denote expectation, and $\Gamma(\cdot)$ is the gamma function.

Based on the scintillation index definition [See Eq. (50) in Chapter 2]

$$\sigma_I^2 = \frac{\langle I^2 \rangle}{\langle I \rangle^2} - 1, \tag{17}$$

and combining with Eq. (16), the shape parameter β can be derived in terms of the scintillation index by [99, Eq. (6-15)]

$$\sigma_I^2 = \frac{\Gamma(1+2/\beta)}{\Gamma(1+1/\beta)^2} - 1 \approx \beta^{-11/6}. \tag{18}$$

For the derivation of the scale parameter η, without loss of generality, the irradiance data is normalized in the sense that $\langle I \rangle = 1$, and setting $n = 1$ in Eq. (16), yields

$$\eta = \frac{1}{\Gamma(1+1/\beta)}. \tag{19}$$

3.3.2 Exponentiated Weibull fading

Models in which the fading is characterized by a single PDF are only valid for stationary conditions, where the statistics of the channel are somehow invariant over the observation time period. On the other hand, if the process of interest is non-stationary and the signal statistics vary significantly over the interval of interest, a mixture of model is better suited, where a weighted summation of several statistical distributions can be used [97].

Let us now extend the simple Weibull fading channel model. Assume an optical wave propagating in the turbulent atmosphere, with multiple scatterers and random refractive-index variations. As the wave travels through this medium, multipath scattering components start to appear and cause irradiance random fluctuations of

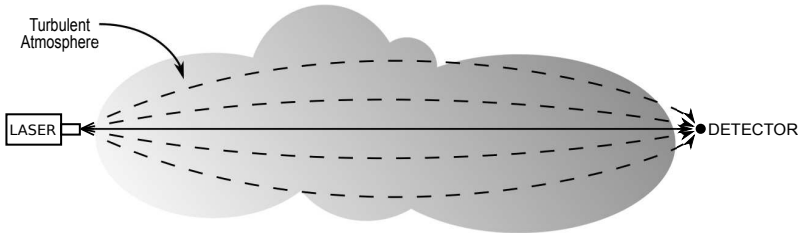

Figure 3.1 Propagation model of a laser beam through the turbulent atmosphere. The received field is decomposed in an on-axis component (solid line), and various weakly scattered off-axis terms (dashed lines).

the signal-carrying laser beam. Then, the observed field at the receiver is, thus, composed by an on-axis component and a weak multipath term, composed by scattered components via different independent off-axis paths. The physical reason for this partition of the received optical field is supported by the high directivity inherent to laser beams sources. Figure 3.1 depicts the on-axis component as a solid line, from the source to the detector, while the dashed-lines represent the weakly scattered off-axis terms. This propagation model is very similar to that proposed by Jurado-Navas et al. [98], but here the term coupled with the on-axis component is dropped.

Considering the above physical justification, the observed field irradiance I is assumed to be a weighted summation of several mutually independent irradiance random variables. Taking into account that the number of separable or independent components is unknown, and even the degree of correlation of such terms, a simple summation is not valid as this would imply that different traveling waves are mutually coherent, i.e. correlated. Thus, in order to provide the necessary degrees of freedom to the mathematical model to account for uncorrelated terms a generalized average is used as follows

$$I^p = \sum_{j=1}^{m} w_j I_j^p, \tag{20}$$

where I_j are Weibull random variables, and w_j are weighting factors accounting for the mean attenuation of each path. This factors are normalized such that $\sum w_j = 1$. The on-axis component is denoted by I_1, and there are $m-1$ off-axis terms. Moreover, instead of a summation of linear components it is assumed the existence of a nonlinear relationship—as in the Weibull fading model— manifested in terms of a power parameter $p > 0$. Recall that a similar, but much simpler, approach is used to derive the Gamma model. Refer to Appendix D.3 for a more detailed explanation.

Now, supported by the fact that the on-axis term is on average greater than the multipath component one can try to make an approximation of the summation in Eq. (20). The naive alternative would be to drop all the off-axis terms, but this would lead to the simple Weibull fading model derived in the previous section. Then, in order to approximate such summation to the on-axis component, but still considering the off-axis terms the maximum function can be introduced as

$$I = \lim_{p\to\infty} \left[\sum_{j=1}^{m} w_j I_j^p \right]^{1/p} = \max\left\{ I_1, I_2, \ldots, I_m \right\}, \tag{21}$$

where $I_1, I_2, \ldots, I_m$ are independent and identically distributed Weibull random variables of the irradiance data terms. Therefore, the cumulative distribution function of I_j is given by Eq. (15), and using the property of ordered statistics for the maximum of a sample the CDF of the irradiance is $F(I) = [F_{I_j}(I)]^m$ [100, Eq. (5.3b)]. These types of distributions are referred to in the literature as exponentiated distributions, were m is a nonnegative integer number.

Furthermore, it is a natural assumption to define $\alpha > 0$ as the real valued extension of m. This allows for a less stringent model, where noninteger values may account for nonzero correlation among the components of different propagation paths [96]. Therefore, the parameter α can be interpreted as the average number of on-axis plus off-axis components effectively intervening in a given observation period.

Physical intuition tells us that the α parameter should be low for weak turbulence, as there are few scatterers decreasing the probability of off-axis components to appear, increasing to a maximum value somewhere in the moderate turbulence regime, as the number of scatterers increases too. Nevertheless, when approaching the strong turbulence regime this value should decrease as—although, there is a higher number of scatterers in the optical path—the off-axis components easily deviate in such a way that the probability of missing the receiver increases. Moreover, the value of α can be lower than unity denoting deep fading events, during the observation time period, meaning that on average even the on-axis component could not reach the receiver.

Then, the PDF and CDF of a random variable I described by the exponentiated Weibull (EW) distribution are given by

$$f_I(I;\alpha,\beta,\eta) = \frac{\alpha\beta}{\eta}\left(\frac{I}{\eta}\right)^{\beta-1}\exp\left[-\left(\frac{I}{\eta}\right)^{\beta}\right]\left\{1-\exp\left[-\left(\frac{I}{\eta}\right)^{\beta}\right]\right\}^{\alpha-1}, \tag{22}$$

and

$$F_I(I;\alpha,\beta,\eta) = \left\{1-\exp\left[-\left(\frac{I}{\eta}\right)^{\beta}\right]\right\}^{\alpha}, \tag{23}$$

respectively; where $\beta > 0$ and $\alpha > 0$ are shape parameters, and $\eta > 0$ is a scale parameter, which is related to the mean value of the irradiance. It is noteworthy that Eq. (22) includes other distributions, such as the Weibull ($\alpha = 1$), Rayleigh ($\alpha = 1, \beta = 2$), and the negative exponential ($\alpha = 1, \beta = 1$).

The n-th irradiance moment of the exponentiated Weibull PDF has recently been derived for any α, both real and integer, and has the form [101]

$$\langle I^n \rangle = \alpha\eta^n\Gamma\left(1+\frac{n}{\beta}\right) g_n(\alpha,\beta). \tag{24}$$

where $g_n(\alpha,\beta)$ was introduced to simplify the notation, and is defined by

$$g_n(\alpha,\beta) = \sum_{j=0}^{\infty}\frac{(-1)^j\Gamma(\alpha)}{j!(j+1)^{1+\frac{n}{\beta}}\Gamma(\alpha-j)}. \tag{25}$$

Equation (25) is easily computed numerically as the series converges rapidly, and usually as much as ten terms or less are sufficient for the series to converge.

3.4 EW Distribution Parameters Derivation

For any PDF model proposed it is very desirable to find expressions for the distribution parameters directly related to atmospheric parameters. In fact, the lack of such expression for the Beckmann distribution was one of the major impediments for the distribution to be widely accepted. Although, this model has been found to be in close agreement with various type of data [12].

Traditionally, in the literature concerning FSO communications, the parameters of the PDF of the irradiance data have been directly related to atmospheric parameters through the scintillation index using Eq. (17). Now, inserting Eq. (24), the exponentiated Weibull distribution parameters are related with the SI as

$$\sigma_I^2 = \frac{\Gamma(1+2/\beta)g_2(\alpha,\beta)}{\alpha\left[\Gamma(1+1/\beta)g_1(\alpha,\beta)\right]^2} - 1. \tag{26}$$

The analytic derivation of the EW parameters is rather a complex task, as it is readily seen from Eq. (26). Therefore, a semi-heuristic approach was used to obtain a relationship between the EW parameters and the scintillation index.

For the semi-heuristic study a wave-optics code was set in order to obtain the probability density function for different turbulence strengths and several receiving apertures. The detailed explanation of the simulation scenario is given below, in Sec. 3.5.1, and can also be found in [80, 102].

Using simulation data the probability density function was obtained for each receiving aperture and Rytov variance σ_R^2 value—i.e. different turbulence strengths. Next, the exponentiated Weibull distribution was fitted to the simulation PDF, using the Levenberg-Marquardt least-square fitting algorithm [103, 104], to obtain a best-fit estimation of the EW distribution parameters. After a exhaustive data mining process, it was found that the shape parameter β closely follows the power rule $\beta \simeq a(\alpha\sigma_I^2)^{-b} + c$; where a, b and c are real nonnegative constants. After applying standard curve fitting methods, the shape parameter β was found to be

$$\beta \simeq 1.012(\alpha\sigma_I^2)^{-13/25} + 0.142. \tag{27}$$

Predicted values of the parameter β for the exponentiated Weibull distribution are presented in Fig. 3.2(a). Here, simulation results values $\beta_{\rm sim}$ are shown by crosses, and the estimated values $\beta_{\rm fit}$, using Eq. (27), are shown by a solid line. It is readily seen how the power law expression found provides an excellent fit to the β values obtained from simulation data.

Performing exhaustive data mining procedures, as for the β parameter, a first approximation for the second shape parameter in the EW distribution was found to approximately be given by [80]

$$\alpha \simeq 3.931(D/\rho_0)^{-0.519}; \tag{28}$$

where $\rho_0 = (1.46C_n^2k^2L)^{-3/5}$ is the atmospheric coherence radius and D is the receiving aperture diameter. Nevertheless, this expression was found to work only in some particular cases. Furthermore, the power law expression in Eq. (28) is in contradiction of the physical expected behavior for the shape parameter α, as discussed in the previous section.

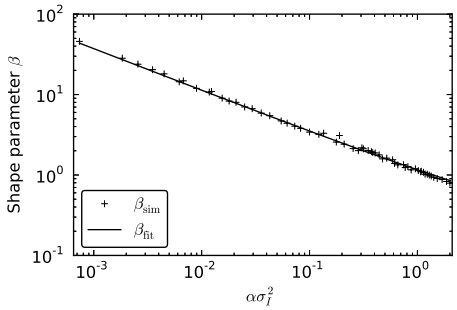

(a) Crosses denote values from simulation data, and the solid line is the predicted values using Eq. (27).

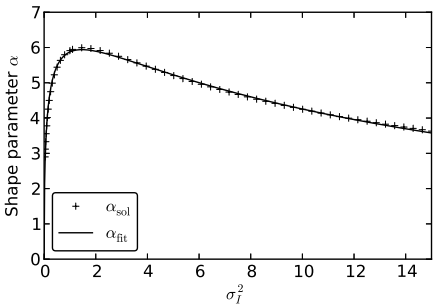

(b) Crosses denote values by solving Eq. (26), and the solid line is the predicted values using Eq. (29).

Figure 3.2 Curve fitting for the shape parameters α and β of the exponentiated Weibull distribution.

Therefore an alternative procedure is undertaken. Thus, Eq. (27) is inserted in Eq. (26) to graphically solve for α in terms of the scintillation index. This method was chosen as the numerical methods tried to solve nonlinear equations resulted in unstable solutions. The values of the shape parameter obtained with this method, denoted as α_{sol}, are shown in Fig. 3.2(b) with crosses. Next, after applying standard curve fitting methods, the shape parameter α was found to approximately follow

$$\alpha \simeq \frac{7.220\sigma_I^{2/3}}{\Gamma\left(2.487\sigma_I^{2/6} - 0.104\right)}, \tag{29}$$

and the estimated values using this expression are also presented in Fig. 3.2(b) with a solid line, and labeled as α_{fit}. It is readily seen how the expression in Eq. (29) provides an excellent fit to the α_{sol} values.

Finally, once the shape parameters α and β are obtained, for the derivation of the scale parameter η, without loss of generality, it is assumed that $\langle I \rangle = 1$, and setting $n = 1$ in Eq. (24), yields

$$\eta = \frac{1}{\alpha\Gamma(1 + 1/\beta)g_1(\alpha, \beta)}. \tag{30}$$

It is easily verified that for fixed values of the shape parameter β and the scale parameter η, the shape parameter α controls the left-tail steepness of the PDF—when data is visualized in a logarithmic scale. This is an attractive property of the EW distribution as, in any communication system, it is precisely the left-tail of critical importance because it defines the error-rate and fade probability.

3.5 Data Analysis

Simulation results and experimental data are used to study the suitability of the exponentiated Weibull distribution to model the probability density function of the received optical power in FSO communication links [80, 105].

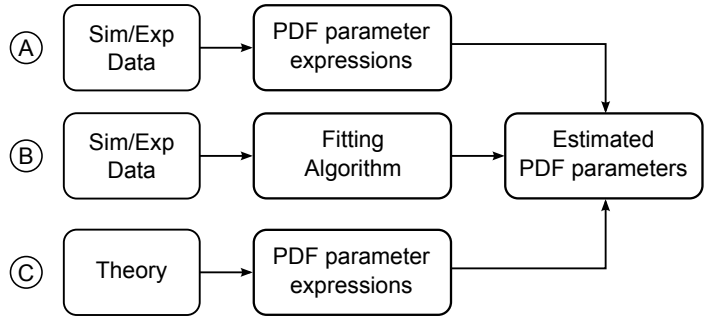

Figure 3.3 Estimation methods for the PDF distribution parameters.

For the analysis the PDF data is compared to the EW, LN and GG models. Hereafter, three different methods, presented in Fig. 3.3, are used to estimate the distribution parameters for each one of the PDF models tested. Method A uses data directly extracted from simulations or experiments to estimate the distribution parameters through the corresponding expressions. Method B estimates the parameters using the Levenberg-Marquardt least-squares fitting algorithm [103, 104]. Whereas, method C utilizes the scintillation index predicted by the theory to estimate the distribution parameters using the corresponding expressions for each PDF model.

In Sec. 3.5.1 and Sec. 3.5.3 method A is used to estimate the distribution parameters for the LN and EW models. Therefore, the LN parameter is estimated using the scintillation index extracted directly from the simulation or experimental data in combination with Eq. (3), while the expressions presented in Sec. 3.4 are used to estimate the parameters of the EW distribution. To estimate the GG distribution parameters method B is preferred over A, as it produces better fits to the actual PDF data [14, 94, 106]. Additionally, the EW PDF parameters are also estimated following method B. Finally, in Sec. 3.5.2, method C is used for comparison of all three PDF models to simulation results, as all the link variables can be controlled allowing for a better consistency between the theoretical predictions and the actual data.

The parameter values used to plot each distribution are presented in tables, to allow for better readability of the figures. For the sake of clarity some parameters have the subscript 'fit' or 'data', meaning that their values are extracted from the fitting process or the data itself, respectively. If no subscript is found, then, the value of such parameter is estimated with the corresponding expression.

3.5.1 Simulation results

To study the PDF of the received optical power in free-space optical links, a simulation scenario was set in order to obtain the probability density function for several receiving apertures. The wave optics code used to perform the numerical simulations is based on the fractal method, using the Kolmogorov spectrum of turbulence, where the phase screens are directly reproduced in the spatial domain by first generating an exact low-resolution screen, by means of the covariance method [51], of 16×16 points. Next, successive interpolations, using the method by Lane et al. [50], were executed to produce the desired grid size of 512×512 points. The final grid spacing Δx for the

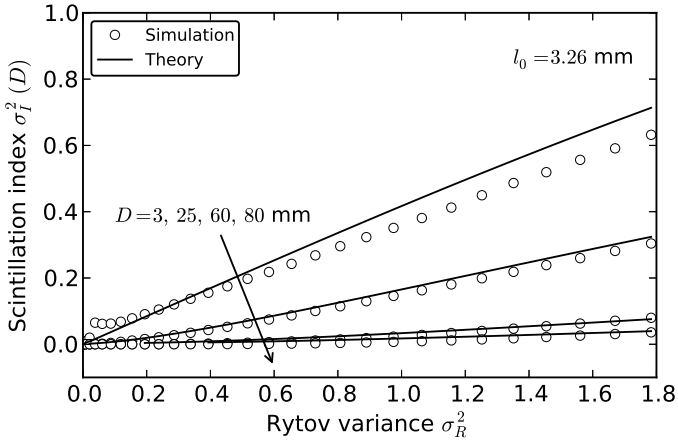

Figure 3.4 Scintillation index predicted by simulation data (circles) and theory (solid line) for $C_n^2 = 2.1 \times 10^{-14}$ m$^{-2/3}$, and different receiving aperture sizes.

propagation window is 1.63 mm.

All the simulations for a Gaussian beam were conducted setting a link distance of 1425 m using 29 random phase screens, a refractive-index structure constant $C_n^2 = 2.1 \times 10^{-14}$ m$^{-2/3}$ was used, the wavelength and the half-angle beam divergence were set to $\lambda = 780$ nm and $\theta = 37$ μrad, respectively. The initial beam radius is given by $W_0 = D_T/(2\sqrt{2})$, where $D_T = 3.2$ cm is the transmitter aperture. The simulation parameters reproduce conditions of weak to moderate turbulence, with Rytov variances $\sigma_R^2 = 1.23 C_n^2 k^{7/6} L^{11/6}$ from 2×10^{-3} to 1.78. A total of 30000 realizations were run to reduce the statistical uncertainties in the numerical simulations of the irradiance.

Receiving apertures of 3, 25, 60 and 80 mm were used to analyze the effects of aperture averaging. Under the simulation conditions used the 3 mm receiving aperture behaves as a point-like receiver, as it is always smaller than the atmospheric coherence radius ρ_0 [94].

In Fig. 3.4 the scintillation index values obtained from the simulation results are compared with the theory presented in Sec. 2.3.5.3 of the previous chapter. It is readily seen how the simulation data complies with the analytic predictions. One effect of using a finite grid is that, although a Kolmogorov spectrum is used, the minimum effective scale size that produces scintillation is not zero, but rather it is determined by twice the grid spacing Δx owing to Fourier spectral considerations [107]. The outer scale of turbulence is still considered to be unbounded, and its effects on the total SI negligible. Thus the simulated data had to be compared with a theoretical curve including the effects of a nonzero inner scale size $l_0 = 3.36$ mm. The expression used to calculate the solid lines in Fig. 3.4 can be found in Appendix C.3. The difference between the SI predicted by theory and simulation for the smallest receiving aperture, i.e. $D = 3$ mm, can be explained due to the fact that the propagation window is discretized in steps of 1.63 mm making difficult to accurately represent the circular area for $D = 3$ mm, resulting in an area slightly larger than expected.

The simulated PDF was obtained by sorting the normalized irradiance data into a histogram of 80 bins of equal width, and the count of each bin was associated with

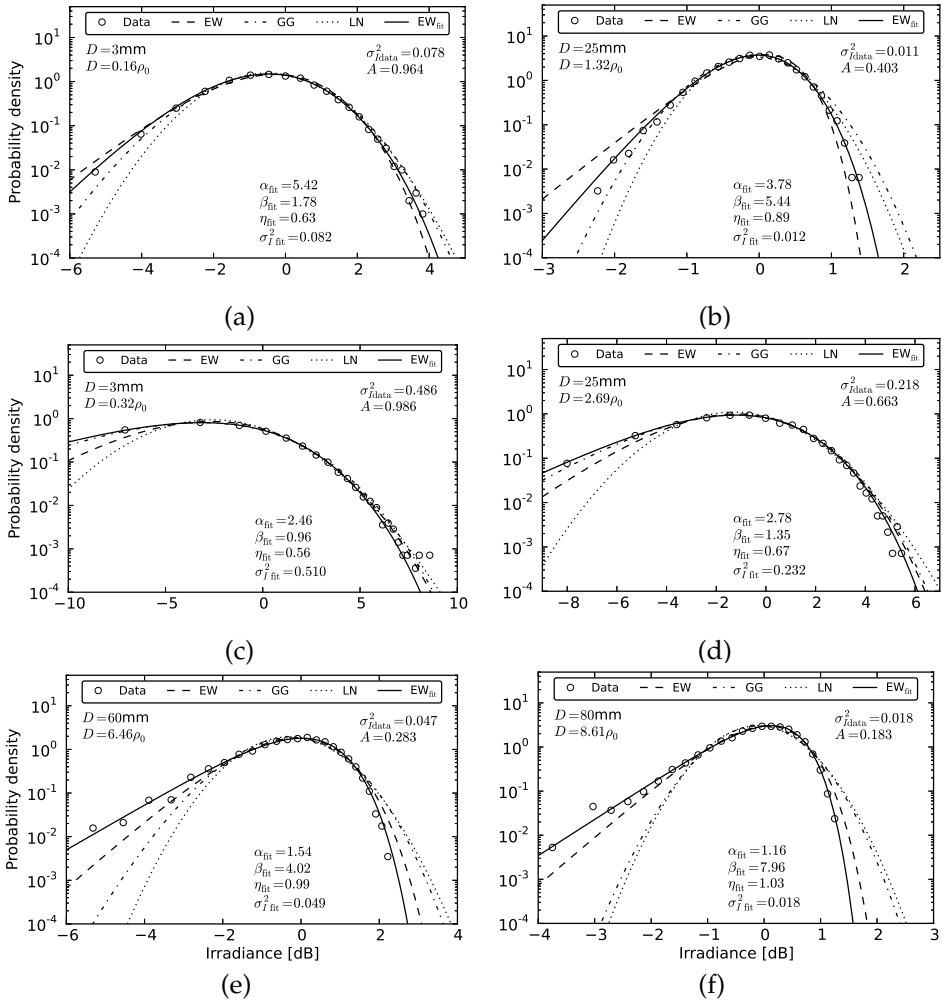

Figure 3.5 Simulation data PDF for (a)(b) $L = 325$ m and $\rho_0 = 18.89$ mm; and (c)–(f) $L = 1225$ m and $\rho_0 = 9.27$ mm. The best fit curve for the EW distribution (solid line) is shown along with its parameters values.

the midpoint of its respective bin width. When a zero-count bin is found its width is merged with the next bin to the right, thus, unequal bins were used whenever needed.

To demonstrate the suitability of the exponentiated Weibull distribution in the weak and moderate turbulence regime Fig. 3.5 is presented, and Table 1 lists all the parameters needed to reproduce the PDF plots. The $\sigma^2_{I\text{data}}$ value is used to deduce the LN (dotted line) and EW (dashed line) parameters, using the estimation method A described in the previous section. For the GG model (dash-dotted line) the parameter values are obtained from the fitting algorithm applying the estimation method B. Furthermore, in Table 1 link defining parameters are also listed, such as the receiving

aperture size D, the Rytov variance σ_R^2 and the aperture averaging factor A given by [24]

$$A = \left[1 + 0.333\left(\frac{kD^2}{4L}\right)^{5/6}\right]^{-7/5}, \tag{31}$$

where $k = 2\pi/\lambda$ is the wavenumber. Figure 3.5 includes the best fit—using method B—of the exponentiated Weibull distribution (solid line) to the PDF data and the corresponding fitted parameter values are embedded in each plot, as well as the scintillation index determined from such parameters.

In the weak turbulence regime the PDF for the two smallest apertures of 3 mm and 25 mm tested at a distance $L = 375$ m is shown in Figs. 3.5(a) and (b), respectively. It is clearly seen how the GG model (dash-dotted line) is valid for the smaller aperture—i.e. the point-like apertures—as expected. Nevertheless, in Fig. 3.5(b) the GG is not capable of effectively reproducing the right-tail shape of the PDF data, and presents a slight deviation in the left-tail. On the other hand the EW distribution appears as a valid model, where the best fit (solid line) closely follows the PDF data. The EW model—obtained from the estimation method A—has an excellent fit in Fig. 3.5(a); while it fails to reproduce the left-tail in Fig. 3.5(b). The Lognormal distribution, although valid for the right-tail in Fig. 3.5(a), does not fit the data in both cases. In the weak turbulence regime the PDF for the 60 and 80 mm apertures is not shown due to the fact that the histogram is completely concentrated in a bin of 1 dB width or less.

For the moderate turbulence regime all the four receiving apertures are tested for $L = 1225$ m, and the corresponding plots are shown in Figs. 3.5(c)–(f). Here, the exponentiated Weibull distribution keeps giving the best fit for all the receiving apertures tested. It is evident how the GG model and the EW distribution have a fit very close to the simulation PDF in Fig. 3.5(c) and (d), although, the EW distribution has a better fit for the Fig. 3.5(e) and (f) receiving apertures. Moreover, the EW obtained from method A outperforms the best fit GG model, for the 60 and 80 mm apertures. In the moderate turbulence cases, the LN model fails by a large amount, except in Fig. 3.5(c); where it can be regarded as a good fit. Nevertheless, the Lognormal distribution always presents the worst fit to the PDF data.

Table 1 Parameters for the LN, GG and EW distributions used to generate PDF curves in Fig. 3.5. The general conditions of the simulations, and the estimated scintillation index for the GG and EW distributions are also shown.

Aperture	Conditions			LN	Gamma-Gamma			Exponentiated Weibull			
D [mm]	$\sigma^2_{I\text{data}}$	σ_R^2	A	$\sigma^2_{\ln I}$	α_{fit}	β_{fit}	$\hat{\sigma}^2_{I\text{fit}}$	α	β	η	$\hat{\sigma}_I^2$
3.0	0.078	0.154	0.964	0.075	24.21	24.21	0.084	3.53	2.13	0.76	0.078
25.0	0.011	0.154	0.403	0.011	143.02	143.02	0.014	1.71	8.07	1.00	0.012
3.0	0.486	1.351	0.986	0.396	5.22	3.07	0.579	5.45	0.76	0.30	0.487
25.0	0.218	1.351	0.663	0.198	4.77	25.84	0.256	4.68	1.15	0.51	0.219
60.0	0.047	1.351	0.283	0.046	22.63	171.62	0.050	2.98	2.98	0.85	0.047
80.0	0.018	1.351	0.183	0.018	171.62	84.68	0.015	2.07	5.78	0.97	0.018

3.5.2 Analytical PDF of the irradiance data

In the previous section the Lognormal and the exponentiated Weibull distributions were plotted using the expression presented in Sec. 3.2.1 and Sec. 3.4, respectively; while using the scintillation index value directly extracted from the simulation data, denoted as $\sigma^2_{I\text{data}}$. Additionally, the Gamma-Gamma distribution was fitted to the PDF data using a least-squares algorithm, as well as for the EW model. The corresponding parameters for each PDF plot were given in Table 1.

In this section, the distribution parameters for the LN, GG and EW models are estimated directly from the scintillation index values $\sigma^2_{I\text{th}}$ predicted from the expressions presented in Appendix C. For this analysis, the same simulation data set used in Sec. 3.5.1 is employed. The resulting PDF curves are plotted in Fig. 3.6 and the corresponding parameter values are listed in Table 2. On the one hand, the SI predicted by Eq. (C.9) is used to estimate the distribution parameters for the LN and EW models. On the other hand, the GG model parameters are estimated using Eq. (9) and Eq. (10), in combination with Eq. (C.10) and Eq. (C.14), respectively. Again, the inner scale of turbulence is set to $l_0 = 3.26$ mm, and the outer scale of turbulence is assumed to be unbounded.

This analysis permits to directly compare the predictions made by each model, when relying only in link parameters. In other words, this allows to assess the suitability of each model when predicting the probability density function of irradiance, when link conditions are known beforehand.

The PDF from simulation data (circles) in Fig. 3.6 is exactly the same as in Fig. 3.5. Nevertheless, the PDF for the LN (dotted line), GG (dashed line) and EW (dashed line) models are plotted by estimating their respective parameters from the scintillation index theory. Again, Fig. 3.5(a) and (b) correspond to weak turbulence conditions with $\sigma^2_R = 0.15$, and Fig. 3.5(c)–(f) correspond to the moderate turbulence regime with $\sigma^2_R = 1.35$. It is immediately evident how in weak turbulence the EW distribution offers the better prediction for the PDF's left-tail, but fails in the right-tail shape where the LN and GG present better fits, specially in Fig. 3.5(b). Note that the EW parameter expressions found directly depend on the SI, and for values close to zero these expressions appear to have poorer performance.

In moderate turbulence conditions the EW offers the better fit, with particular interest on the left-tail of the PDF data. As expected the GG offers an excellent fit for the smallest aperture $D = 3$ mm, and a good fit for $D = 25$ mm. It is noteworthy that

Table 2 Parameters for the LN, GG and EW distributions used to generate PDF curves in Fig. 3.6. The general conditions of the simulations, and the estimated scintillation index for the GG and EW distributions are also shown.

Aperture	Conditions			LN	Gamma-Gamma			Exponentiated Weibull			
D [mm]	$\sigma^2_{I\text{th}}$	σ^2_R	A	$\sigma^2_{\ln I}$	α	β	$\hat{\sigma}^2_I$	α	β	η	$\hat{\sigma}^2_I$
3.0	0.065	0.154	0.964	0.063	28.74	33.91	0.065	3.33	2.40	0.80	0.065
25.0	0.014	0.154	0.403	0.014	194.61	117.91	0.014	1.85	7.05	0.99	0.014
3.0	0.555	1.351	0.986	0.441	3.66	4.52	0.555	5.56	0.71	0.28	0.555
25.0	0.237	1.351	0.663	0.213	7.57	10.77	0.237	4.77	1.10	0.48	0.238
60.0	0.052	1.351	0.283	0.050	41.78	36.87	0.052	3.08	2.79	0.84	0.052
80.0	0.027	1.351	0.183	0.026	111.12	56.60	0.027	2.42	4.37	0.93	0.027

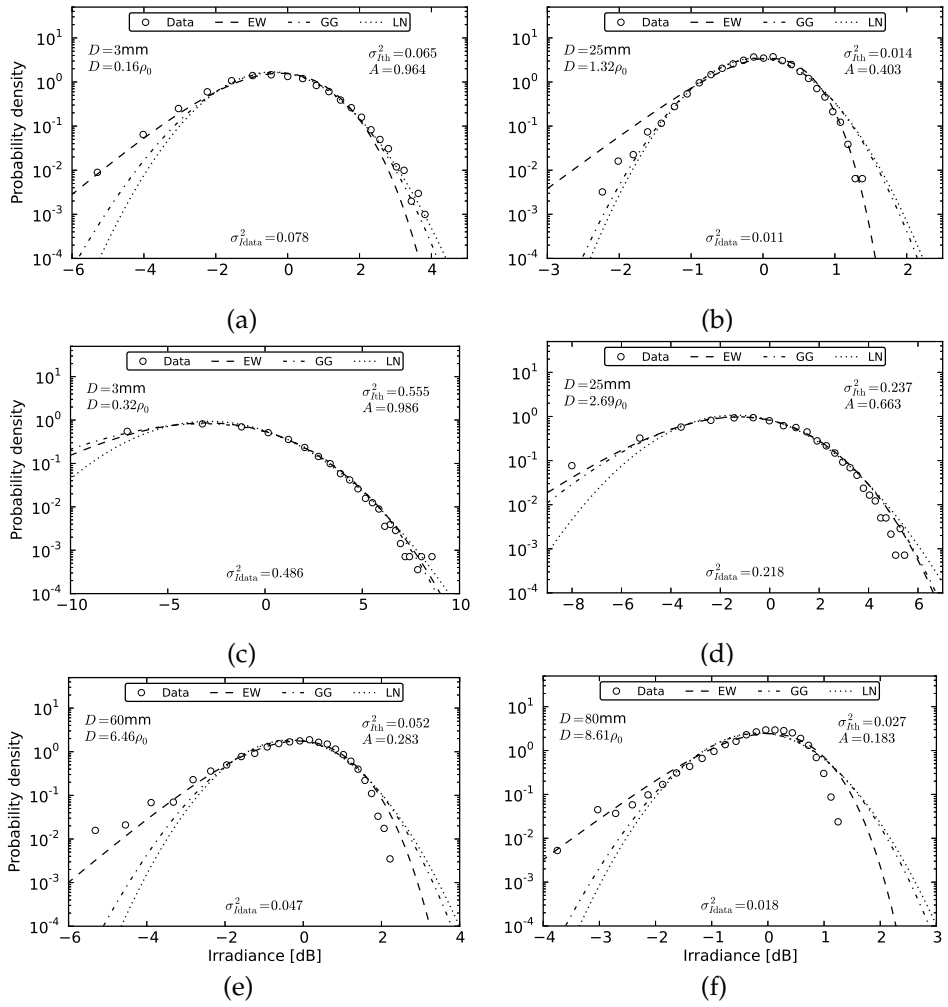

Figure 3.6 Simulation data PDF for (a)(b) $L = 375$ m and $\rho_0 = 18.89$ mm (weak turbulence); and (c)–(f) $L = 1225$ m and $\rho_0 = 9.27$ mm (moderate turbulence).

EW distribution replicates the GG model behavior in Fig. 3.5(c), and outperforms in Fig. 3.5(d)–(f). The LN distribution is the worst of all the models tested, albeit it approaches the predictions made by the GG distribution in weak turbulence conditions. Recall that the Lognormal model has been proved valid before [93, 99], although new evidence suggests that the PDF data is not truly LN distributed [57, 93], specially when the light source is a Gaussian beam [14, 94].

Analyzing Fig. 3.6 it can be concluded that the predictions made by the exponentiated Weibull model, when utilizing the theoretical scintillation index, can reproduce the predictions of the Gamma-Gamma distribution for a wide range of aperture averaging conditions, and even outperforms the GG model for large receiving apertures, i.e. when $D > \rho_0$. Nevertheless, the expressions to estimate the EW parameters, de-

duced in Sec. 3.4, appear to have a poor behavior when $\sigma_I^2 < 0.03$, see for example Fig. 3.6(a) and (f).

3.5.3 Experimental data

The experiments were conducted at Barcelona, Spain, between the rooftops of two buildings along a medium density residential terrain. A 780 nm continuous-wave diode laser at 15 mW (12 dBm) from LISA Laser (HL25/MIII), with built-in collimator, was used. A beam expander of diameter 32 mm was mounted with the laser to produce a beam divergence of 37 μrad. The testbed selected for the experiments consisted in a nearly horizontal 1.2 km optical path with the transmitter and receiver at either side of the optical path. At the receiver side the light was detected using a 15 cm focal length Fresnel lens, along with a bandpass interference filter with a 3 dB bandwidth of 10 nm to remove the out-of-band background radiation. A set of diaphragms was used to allow measurements for different aperture diameters. A complete description of the experimental setup can be found in [102].

The irradiance data were collected at the receiver side with a PIN photodetector, and the detected signal was captured at 10 kHz of sampling rate. Data were taken in individual runs for the receiving apertures of 5 min each, hence, 3×10^6 samples were available to calculate the experimental probability density function. The diaphragms used for the experiments had aperture diameters of 3, 25, 60 and 80 mm. The estimated value for the refractive-index structure constant during the experiments was found to be $C_n^2 = 2.1 \times 10^{-14}\ \mathrm{m}^{-2/3}$ [102].

Figure 3.7 shows the probability density function obtained from experimental data, and Table 3 lists all the parameters needed to reproduce the PDF plots. The same procedure presented in Sec. 3.5.1 to estimate the PDF was applied to the experimental data set. Again, the best fit of the exponentiated Weibull distribution (solid line) to the PDF data and the corresponding fitted parameter values are embedded in each plot, as well as the scintillation index determined from such parameters. The scintillation index $\sigma^2_{I\mathrm{data}}$ value—directly extracted from the experimental data—is used to plot the LN (dotted line) and EW (dashed line) distributions. The GG model (dash-dotted line) is plotted using the parameter values obtained from the fitting algorithm, as in Sec. 3.5.1.

It can be seen how both versions of the exponentiated Weibull distribution offer an excellent fit to experimental data under all of the aperture averaging conditions tested. In Fig. 3.7(a) and (b) the EW distribution has the ability to reproduce the shape

Table 3 Parameters for the LN, GG and EW distributions used to generate PDF curves in Fig. 3.7. The general conditions of the experiments, and the estimated scintillation index for the GG and EW distributions are also shown.

Aperture	Conditions			LN	Gamma-Gamma			Exponentiated Weibull			
D [mm]	$\sigma^2_{I\mathrm{data}}$	σ_R^2	A	$\sigma^2_{\ln I}$	α_{fit}	β_{fit}	$\hat{\sigma}^2_{I\mathrm{fit}}$	α	β	η	$\hat{\sigma}_I^2$
3.0	0.477	1.301	0.986	0.390	6.39	3.69	0.470	5.44	0.76	0.31	0.478
25.0	0.212	1.301	0.659	0.192	5.25	57.94	0.211	4.65	1.17	0.52	0.213
60.0	0.058	1.301	0.279	0.056	19.51	171.62	0.057	3.19	2.61	0.82	0.057
80.0	0.023	1.301	0.180	0.023	171.62	60.56	0.022	2.29	4.84	0.94	0.023

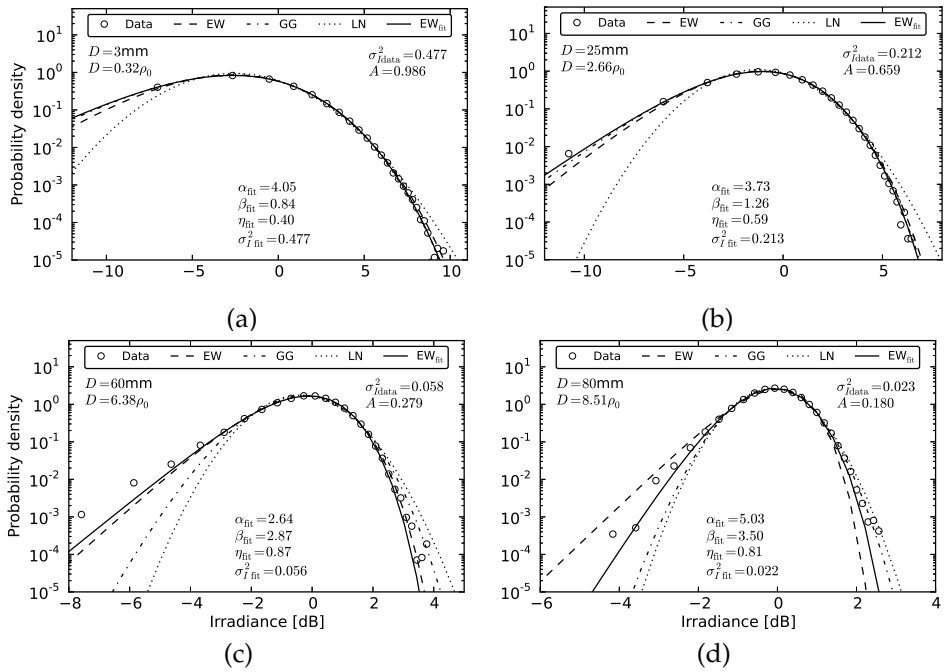

Figure 3.7 Experimental data PDF for $L = 1200$ m, $\rho_0 = 9.40$ mm and different receiving aperture sizes in moderate turbulence conditions. The best fit curve for the EW distribution (solid line) is shown along with its parameters values.

of the Gamma-Gamma model—both the EW best fit and EW predicted by the expressions from Sec. 3.4—, and it gives a better fit for all other cases. Again, the models have been tested through a wide range of aperture averaging conditions. Nevertheless, the EW model predicted with the estimation method A still presents a poor behavior when $\sigma_I^2 < 0.1$, slightly overestimating the left-tail and underestimating the right-tail of the PDF data in Fig. 3.7(d). It should be noted that the Gamma-Gamma distribution is confirmed as a valid model for the PDF data when $D < 5\rho_0$, i.e. the receiving aperture diameter is comparable or smaller than the atmospheric coherence radius (see Figs. 3.5–3.7).

3.6 Data from other Authors

In this section already published data is used to assess the proposed exponentiated Weibull distribution when modeling the PDF of irradiance data in FSO links. Moreover, a comparison of this model to the Gamma-Gamma and Lognormal distributions is also made, as the two most widely accepted models nowadays.

For completeness of this study numerical simulation results as well as experimental data are used. The simulation data was extracted from Vetelino et al. [94], while the experimental data used can be found in Wayne et al. [14]. Note that, in some figures, the original axes limits are changed aiming to a better resolution allowing for a

straight forward comparison of the different PDF curves plotted.

The parameter values used to plot each distribution are presented in Table 4 and Table 5. Here, the same subscript convention for variables names as in Sec. 3.5 is followed.

3.6.1 Simulation data

The numerical simulation data presented in Vetelino et al. [94] was intended to reproduce the experimental results of a testbed where a 1550 nm continuous-wave laser, with 0.46 mrad full-angle divergence, was used. The beam was launched in a 1500 m horizontal path and, at the receiver plane, the optical power was detected using three simultaneous photodetectors of 1, 5, and 13 mm with no collecting lenses. For the simulation the smallest aperture used is 1.8 mm instead of 1 mm [94].

The simulation was conducted with an optics wave code based on the spectral method of the split-step technique, in which phase screens are generated in the spectral domain by means of filtering Gaussian white noise with the second-order statistics of the selected turbulence power spectrum [47–49]. The power spectrum chosen is the Kolmogorov spectrum, therefore the inner and outer scale of turbulence are ignored. In this case the turbulence strength C_n^2 used corresponds to the value inferred from the experimental data.

The probability density function of the irradiance fluctuations is generated from 40,000 realizations for each case, and then plotted as a function of the normalized log-irradiance. It should be noted that the PDF values for the GG and LN distributions are obtained by the transformation [94]

$$f_X(z) = f_X(I)\frac{dI}{dz}\bigg|_{I=e^z} = e^z f_X(e^z), \tag{32}$$

where $f_X(\cdot)$ is given by either Eq. (2) or Eq. (8), and $z = \ln I$ is the natural logarithm of the normalized irradiance.

The simulation data PDFs shown in Fig. 3.8 correspond to those presented in Fig. 3 of Vetelino et al. [94]. In Table 4 all the defining parameters of the three PDFs being studied are listed, along with the other parameters as in Sec. 3.5.

Note that the scintillation index $\sigma^2_{I\text{data}}$ was calculated directly from the simulation data, and the $\sigma^2_{\ln I}$ parameter in the LN model was obtained from Eq. (3). The

Table 4 Parameters for the LN, GG and EW distributions used to generate PDF curves in Fig. 3.8. The general conditions of the simulations, and the estimated scintillation index for the GG and EW distributions are also shown.

Aperture	Conditions			LN	Gamma-Gamma			Exponentiated Weibull			
D [mm]	$\sigma^2_{I\text{data}}$	σ^2_R	A	$\sigma^2_{\ln I}$	α_{fit}	β_{fit}	$\hat{\sigma}^2_{I\text{fit}}$	α	β	η	$\hat{\sigma}^2_I$
1.8	1.230	2.7	0.997	0.80	1.49	3.00	1.228	5.93	0.50	0.14	1.227
1.8	3.550	19.2	0.997	1.51	0.88	0.88	3.564	5.57	0.36	0.05	3.547
5.0	1.190	2.7	0.985	0.78	1.83	2.42	1.185	5.92	0.51	0.14	1.187
5.0	3.150	19.2	0.985	1.42	0.96	0.96	3.168	5.66	0.37	0.06	3.146
13.0	1.010	2.7	0.928	0.70	2.38	2.38	1.017	5.88	0.55	0.17	1.008
13.0	2.160	19.2	0.928	1.15	1.28	1.28	2.173	5.87	0.41	0.08	2.154

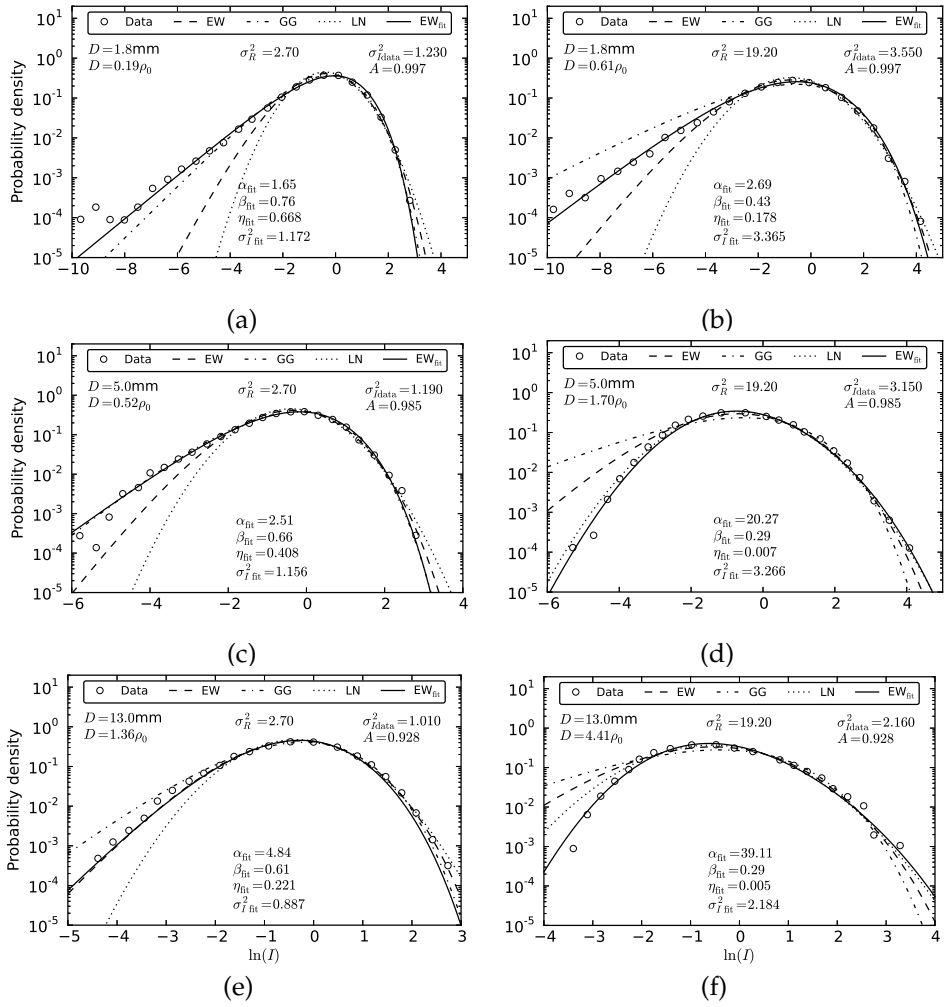

Figure 3.8 Simulation data PDF from Vetelino et al. [94] in comparison with the EW distribution. The curves are plotted using the parameters from Table 4. The best fit curve for the EW distribution (solid line) is shown along with its parameters values.

α_{fit} and β_{fit} parameters, presented in Table 4, are those found by a fitting process in Vetelino et al. [94], and the corresponding $\hat{\sigma}^2_{I\text{fit}}$ was calculated using Eq. (11), for the GG distribution.

On the other hand the α, β and η parameters for the proposed EW model, were obtained from the equations presented in Sec. 3.4, and are also listed in Table 4. These parameters along with Eq. (26) are used to calculate the scintillation index $\hat{\sigma}^2_I$ for the EW distribution. Additionally, all the plots in Fig. 3.8 include the best fit of the exponentiated Weibull distribution to the PDF data and the estimated parameter values are embedded in each plot, as well as the scintillation index determined from such

parameters.

3.6.2 Experimental data

The data presented in Wayne et al. [14] correspond to an experimental setup, consisting in a 532 nm continuous-wave solid-state laser (4 mrad full-angle divergence) followed by a defocused beam expander, which produces an approximately spherical wave at the receiver plane. The laser was launched in a 1 km long testbed, and the receiver telescope was a 6 in. (1 in. $= 2.54$ cm) diameter refracting lens. All the data were collected in two minutes runs by means of a 24 bits digitizer operating at 51.25 kS/s, producing a total of 6.15×10^6 samples to construct the experimental PDF for each run. The probability density function was generated by sorting the data using unequal bin widths, thus, avoiding the appearance of zero-count bins in the PDF.

The PDFs plots in Fig. 3.9 correspond to the receiving aperture diameters 4, 20.6 and 154 mm from Figs. 3 and 4 in Wayne et al. [14]. In Table 5 all the defining parameters of the three PDF models being studied are listed. For the experimental data case the $\sigma^2_{\ln I\text{fit}}$ parameter in the LN model as well as the α_{fit} and β_{fit} parameters for the GG model were determined in [14] by doing a best fit of the PDF data. The rest of the parameters in Table 5 were filled following the same approach as in Table 4. Again, all plots in Fig. 3.9 include the best fit version of the exponentiated Weibull distribution to the PDF data, along with the corresponding fitted parameter values as well as the scintillation index determined from such parameters.

Table 5 Parameters for the LN, GG and EW distributions used to generate PDF curves in Fig. 3.9. The general conditions of the experiments, and the estimated scintillation index for the GG and EW distributions are also shown.

Aperture	Conditions			LN	Gamma-Gamma			Exponentiated Weibull			
D [mm]	$\sigma^2_{I\text{data}}$	σ^2_R	A	$\sigma^2_{\ln I\text{fit}}$	α_{fit}	β_{fit}	$\hat{\sigma}^2_{I\text{fit}}$	α	β	η	$\hat{\sigma}^2_I$
4.0	4.570	10.3	0.964	2.00	1.30	1.30	2.130	5.33	0.34	0.04	4.572
4.0	2.250	2.5	0.964	1.78	1.60	1.60	1.641	5.85	0.41	0.08	2.244
20.6	1.500	11.1	0.619	1.16	2.10	2.10	1.179	5.94	0.47	0.11	1.495
20.6	0.840	2.1	0.619	0.73	3.00	3.00	0.778	5.81	0.59	0.19	0.839
154.0	0.140	7.0	0.029	0.15	7.60	95.50	0.143	4.19	1.49	0.62	0.140
154.0	0.050	1.9	0.029	0.06	34.50	34.50	0.059	3.04	2.86	0.84	0.050

3.6.3 Discussion

In this section, the Lognormal and the Gamma-Gamma distributions have been compared to the new proposed model, the exponentiated Weibull distribution. In order to conduct this study already published data have been used, corresponding to numerical simulations [94] and experiments [14]. In both scenarios the respective authors reach the same conclusion, neither distribution—i.e. the LN and GG models—can model the probability density function of the irradiance fluctuations under all aperture averaging conditions and every atmospheric turbulence regime.

It has become customary in the literature to use as a decision criterion, to determine whether the LN or the GG distribution is adequate to model the irradiance PDF,

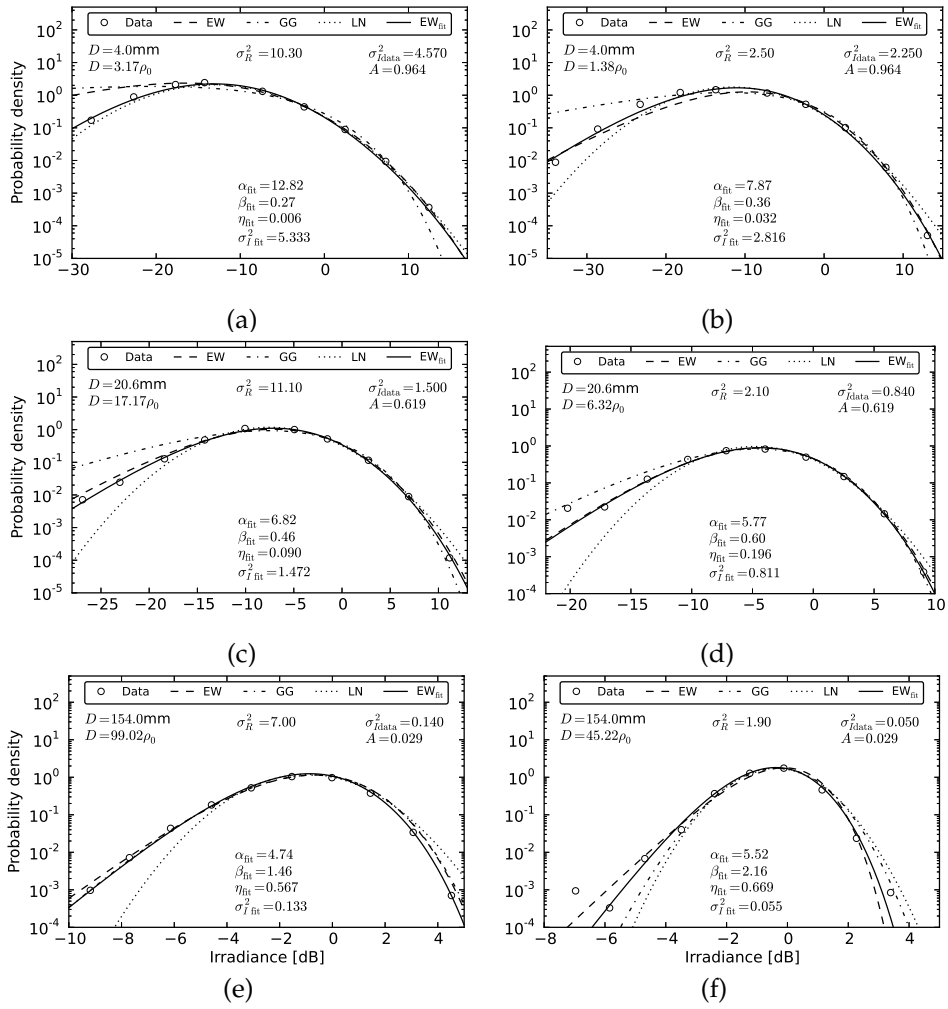

Figure 3.9 Experimental data PDF from Wayne et al. [14] in comparison with the EW distribution. The curves are plotted using the parameters from Table 5. The best fit curve for the EW distribution (solid line) is shown along with its parameters values.

the ratio between the receiving aperture diameter D and the atmospheric coherence length $\rho_0 = (1.46C_n^2k^2L)^{-3/5}$. Basically, it is accepted—in the moderate-to-strong turbulence regime—that if $D \ll \rho_0$ the receiving aperture is unable to average the atmospheric effects and under this condition the Gamma-Gamma distribution presents the best fit to PDF of the received irradiance data. On the contrary, if $D \gg \rho_0$ a fair amount of aperture averaging takes place and the PDF of the data is better described by a Lognormal distribution [58, 60, 106]. While, in the region of $D \sim \rho_0$ there is not a definitive answer and the best distribution to model the irradiance PDF can be either the LN or the GG distribution.

Although this is the general consensus, there are many situations where neither the LN or GG distribution can be said to accurately model the PDF of the irradiance data in numerical simulations and experimental data, specially when aperture averaging takes place. Take for example Figs. 3.8(b), (e), (f), and Figs. 3.9(b), (c), (d), (f). Here, it is readily seen that, although the fitting of the right-tail is almost always achieved, the left-tail of the PDF is the hardest section to be properly fitted by these two distributions.

However, in those situations where the LN and GG distributions both fail, the proposed exponentiated Weibull distribution presents an excellent fit to the probability density function of the irradiance data. This is particularly appreciable in the left-tail of the PDF, which is of maximum importance as it defines the error-rate and fade probability. In both Figs. 3.8 and 3.9, the best fit version of the exponentiated Weibull distribution to the PDF data arises as the closest fit. Note that the estimated scintillation index $\sigma^2_{I\text{fit}}$ from the best fit EW parameters is always within a 10% of error, except for Fig. 3.8(e) and for Figs. 3.9(a) and (b) where the errors are 12.15, 16.70 and 25.15%, respectively.

It is noteworthy that the approximation given in Eq. (27) holds—within a 10% of error— when using the shape parameters α_{fit} and β_{fit} of the EW distribution estimated by the fitting algorithm, although, Eq. (29) does not cope to the values of α_{fit} predicted by the fitting algorithm suggesting the need for a better approximation. It is the author's belief that the shape parameter α for the EW distribution is somehow affected by the ratio D/ρ_0, as previously suggested [80], and/or the Rytov variance σ^2_R.

On the other hand, the shape of the exponentiated Weibull distribution predicted by the expressions derived in Sec. 3.3.2 presents a good fit for the right-tail of the PDF data in Figs. 3.8 and 3.9; while the prediction of left-tail shape is not robust. The better estimation of the probability density function is achieved for the case of experimental data (see Fig. 3.9), where Fig. 3.9(a) is the exception and the prediction for the left-tail is very similar to that of the GG distribution, but a better fit for the right-tail. A possible explanation for this is the relative high value of the scintillation index $\sigma^2_I = 4.57$, and that Eq. (29) is not capable of predicting values of α larger than 6. The goodness of fit of the estimated EW distribution is rather less accurate for numerical simulation data (see Fig. 3.8) than for the experimental data, except for Fig. 3.8(e) where it is a perfect fit. Once again the left-tail is the most problematic section of the PDF. Nevertheless, the predicted scintillation index $\hat{\sigma}^2_I$ from the estimated EW parameters, using the estimation method A, is always within less than 1% of error of the expected value (see Table 4 and Table 5).

3.7 PDF models goodness-of-fit

Previously the exponentiated Weibull distribution has been assessed utilizing different types of data, along with the Lognormal and Gamma-Gamma models. In Sec. 3.5 own produced data sets were obtained from numerical simulations and experiments. Moreover, already published data from other authors have been used in Sec. 3.6, including both simulation results and experiments. There, the EW and LN PDFs have been estimated using the corresponding expressions to deduce their distribu-

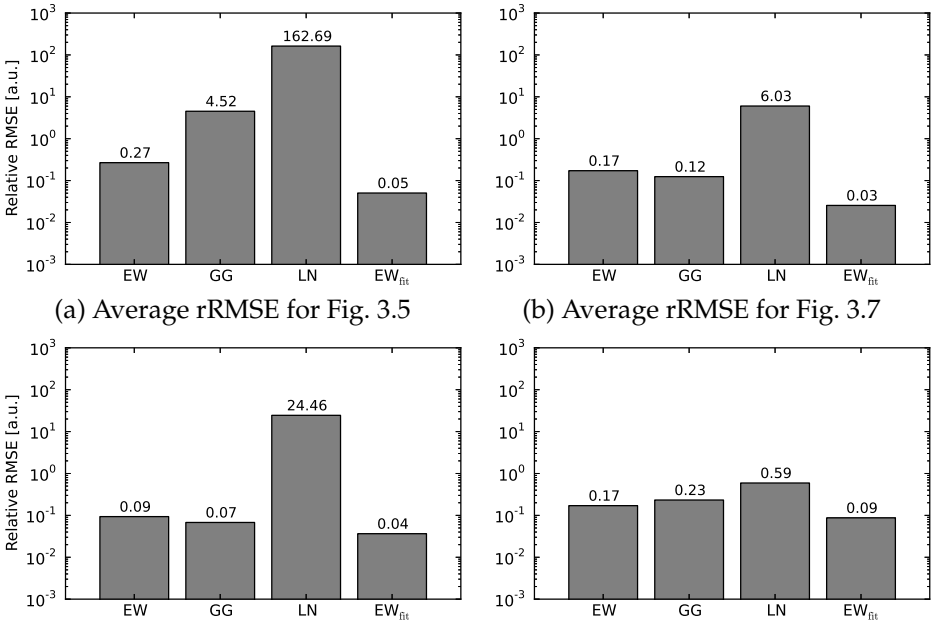

(a) Average rRMSE for Fig. 3.5 (b) Average rRMSE for Fig. 3.7

(c) Average rRMSE for Fig. 3.8 (d) Average rRMSE for Fig. 3.9

Figure 3.10 Average relative root-mean-squared-error (rRMSE) for (a) simulation results, (b) experimental data, (c) Vetelino et al. [94] data and (d) Wayne et al. [14] data.

tion parameters—method A in Fig. 3.3—, whereas the parameters for the GG model are estimated by means of a lest-square fitting algorithm—method B. Additionally, a best-fit version of the EW distribution is also presented for every data set tested. A visual inspection of Figs. 3.5–3.9 allows to qualitatively establish the different degrees of fit to the actual PDF data for all the models analyzed, where the EW distribution appears to have the best performance.

This section presents a quantitative analysis of the degree of goodness-of-fit (GOF) for each model in relation to the actual PDF of irradiance data. Common metrics used to test the goodness of a curve fitting process are the mean squared error (MSE) and the root-mean-squared error (RMSE). The problem with these metrics is that the errors near the peak of the probability density function have more weight than the errors at the tails, which are underestimated and not properly accounted. Therefore, in order to have similar weights for errors at the peak and tails of the PDF a relative root-mean-squared error (rRMSE) is used, defined by

$$\text{rRMSE} = \sqrt{\frac{1}{M}\sum_{j=1}^{M}\frac{(y_j - \hat{y}_j)^2}{\hat{y}_j}}, \tag{33}$$

where y_j and $\hat{y}_j$ denote the actual PDF points and the PDF points estimated by each model tested, respectively. Note that Eq. (33) resembles a chi-square goodness-of-fit test [108, Eq. (9-75)].

The GOF of the exponentiated Weibull, Lognormal and Gamma-Gamma models to the PDF of the irradiance data is evaluated in Fig. 3.10. For the analysis Figs. 3.5, 3.7, 3.8 and 3.9 are used, which correspond to the data sets obtained from simulations, experiments, Vetelino et al. [94] and Wayne et al. [14], respectively. Within each data set the rRMSE is calculated for every PDF model and receiving aperture, and the results are averaged for each PDF model tested. Thus, the suitability of each model being tested can be quantified through the average value of the rRMSE as a measure of GOF to the actual PDF data. For a better readability the average rRMSE values are presented as bar plots, in Fig. 3.10, with logarithmic scale in the vertical axis. The distributions tested are denoted by the labels in the horizontal axis; where models denoted by EW and LN correspond to PDFs estimated using method A, while the GG and EW_{fit} PDFs were estimated with method B—refer to Fig. 3.3.

In the analysis conducted in the previous sections it was concluded that the LN distribution had always the worst fit to the PDF data. This is confirmed by the rRMSE analysis in Fig. 3.10, where the LN model performs at least one order of magnitude poorer than the other two models, except for Fig. 3.10(d) where it is comparable to the other models but continues to be the worst fit. The EW model has an excellent performance similar to the fit offered by the GG PDF for every data set, and even outperforms the GG model in Fig. 3.10(a)—i.e. for simulation results—by one order of magnitude. This is expected as the expressions to estimate the EW distribution parameters were obtained following a semi-heuristic approach based on the simulation data set. As the expressions found in Sec. 3.4 are a first approximation, the best fit version of the exponentiated Weibull PDF—predicted by method B—has also been included throughout the analysis of the EW fading model and denoted by EW_{fit}. It is readily seen that the fitting performance of the EW_{fit} has the better performance of all the models tested. This indicates that on average the EW distribution was capable of offering the best fit to the actual PDF of the irradiance data, for the weak-to-strong turbulence regime under various aperture averaging conditions.

3.8 Summary

A new fading model was presented to describe the irradiance fluctuations in free-space optical links, resulting in the exponentiated Weibull distribution; with simple closed-form expression for its PDF and CDF as a very attractive property. The EW model was derived using standard physical assumptions similar to those used for the Gamma model, with the addition of a nonlinearity manifested in terms of a power parameter as in the work by Yacoub [96]. Thus, a physical justification for the appearance of the exponentiated Weibull distribution in FSO links has been provided.

For any PDF model proposed it is very desirable to find tractable expressions relating the distribution parameters directly to atmospheric parameters. Consequently, by means of a semi-heuristic approach a set of equations was derived in Sec. 3.4, relating the EW parameters directly to the scintillation index.

In order to assess the newly proposed model it has been compared with the Lognormal and Gamma-Gamma distributions, the two most widespread distributions nowadays. Numerical simulations were run and an experimental testbed was deployed, to produce PDF data sets under different turbulence and aperture averaging

conditions. In Sec. 3.5 it was shown how the proposed EW distribution offers an excellent fit to simulation and experimental data under all aperture averaging conditions, under weak and moderate turbulence conditions, as well as for point-like apertures. In this analysis the GG model presents an unpredictable performance when $D > \rho_0$. Specially it fails to reproduce the lower-tail shape when aperture averaging takes place. On the contrary, the exponentiated Weibull model gives a perfect fit in both tails of the probability density function of the irradiance data.

In Sec. 3.5.2 the distribution parameters for the LN, GG and EW models are estimated directly from the scintillation index values predicted from theory. This analysis permits to assess the suitability of each model when predicting the probability density function of the irradiance data, if link conditions are known beforehand. It is noteworthy that the EW distribution replicates the GG model behavior in some scenarios—when the latter is valid—, and even outperforms the GG predictions in others. Nevertheless, the expressions in Sec. 3.4 to estimate the EW parameters appear to behave poorer when $\sigma_I^2 < 0.1$. The LN distribution is the worst of all the models tested, indicating that the PDF data is not truly Lognormal as suggested before [92].

In addition, comparisons to previously published data from other authors have been done in Sec. 3.6, including numerical simulation results and experimental data in the moderate-to-strong turbulence regime. In this analysis the expressions to derive the EW parameters have shown to be fairly accurate when the aperture averaging $A < 0.90$, but they have rather unpredictable behavior for values of A close to unity—i.e. for point-like apertures. Nevertheless, it should be noted that the EW parameters expressions were obtained with an approach relying on data from weak-to-moderate turbulence conditions, and such expressions can be improved if sufficient data from the strong turbulence regime are available.

In summary, the exponentiated Weibull distribution has been analyzed with data from the weak-to-strong turbulence regime and compared to the LN and GG models. The results presented here suggest that the EW distribution presents the better fit for data under different aperture averaging conditions. Moreover, expressions to derive the EW distribution parameters have been found. For these reasons the exponentiated Weibull distribution becomes an excellent candidate to model the PDF of irradiance data under all conditions of atmospheric turbulence in the presence of aperture averaging.

4

FSO Link Performance under Exponentiated Weibull Fading

THIS CHAPTER is devoted to present the analysis of the probability of fade and bit error-rate (BER) performance of a FSO link, when the atmospheric turbulence can be modeled by an exponentiated Weibull distribution. New closed-form expressions are derived for the average BER. Moreover, these expressions are extended to include the impact of pointing errors.

4.1 Introduction

In the last chapter a new fading model has been introduced to describe the irradiance fluctuations in free-space optical (FSO) links, resulting in the exponentiated Weibull (EW) distribution. The new model has been compared with the Lognormal (LN) and Gamma-Gamma (GG) distributions, the two most widespread distributions nowadays, using simulation and experimental data results, as well as already published data from other authors.

Here, the analysis for the EW model is continued to include the probability of fade and bit error-rate (BER) performance of a FSO link. New closed-form expressions for the average BER assuming an intensity-modulation/direct-detection (IM/DD) FSO system with on-off keying (OOK) are derived, for the EW and GG models, utilizing a very general special function called the Meijer's G-function [See Appendix B.4]. Furthermore, the BER expression for the proposed exponentiated Weibull fading channel model, is extended to account for misalignment fading based on the seminal paper by Farid and Hranilovic [109].

The remainder of this chapter is structured as follows. First, in Sec. 4.2 the three models being tested are presented, and their probability density function (PDF) and cumulative distribution function (CDF) are given. Next, in Sec. 4.3, closed-form expressions for the average BER are derived. Section 4.4 is devoted to discuss simulation and experimental data results, using the same data sets presented in Chapter 3. The BER analysis is extended to include the impact of pointing errors in Sec. 4.5, assuming that the atmospheric turbulence can be modeled by an exponentiated Weibull distribution. Finally, some concluding remarks are given.

4.2 Probability of Fade

A laser beam propagating through the atmosphere will be altered by refractive-index inhomogeneities. At the receiver plane, a random pattern is produced both in time and space [23]. These fluctuations produce fading events, on the received signal, and under severe atmospheric conditions they can lead to complete outages. The performance of a FSO system can be addressed analytically from the PDF of the randomly fading irradiance signal. Different models were presented in Chapter 3 for the PDF of irradiance data, including the new proposal, namely the exponentiated Weibull distribution. In terms of these PDF models, the probability of fade is defined as the cumulative distribution of probability below a prescribed threshold. Note that the CDF for each model was presented in the previous chapter.

The probability of fade P_{fa} offers an estimate of how likely the received signal is to drop below a prescribed irradiance threshold I_T [58], defined as

$$P_{fa} \triangleq \Pr(I \leq I_T) = \int_0^{I_T} f_I(I) dI = F_I(I_T), \tag{1}$$

where $f_I(I)$ is the corresponding PDF of irradiance fluctuations, and I_T is the threshold level of the irradiance. The probability of fade can be obtained in closed-form, by means of the respective cumulative distribution function $F_I(I)$ for each fading model. For the analysis conducted here a fade threshold parameter F_T is introduced,

which is defined as the number of decibels below the mean irradiance [58]

$$F_T = 10\log_{10}\left(\frac{\langle I\rangle}{I_T}\right), \tag{2}$$

where, without loss of generality, the irradiance data is normalized to the mean value, i.e. $\langle I\rangle = 1$.

Next, the probability of fade expression, in terms of the threshold parameter F_T, is presented for the Lognormal, Gamma-Gamma and exponentiated Weibull distributions. The respective PDFs and some useful expressions, introduced in Chapter 3, are also presented here for a self-contained chapter.

4.2.1 Lognormal distribution

The PDF and probability of fade of a random variable I described by the Lognormal distribution are given by

$$f_I(I) = \frac{1}{I\sqrt{2\pi\sigma^2_{\ln I}}}\exp\left\{-\frac{\left[\ln(I)+0.5\sigma^2_{\ln I}\right]^2}{2\sigma^2_{\ln I}}\right\}, \quad I>0, \tag{3}$$

and

$$P_{fa}(F_T) = \frac{1}{2}+\frac{1}{2}\text{erf}\left[\frac{0.5\sigma^2_{\ln I}-0.23F_T}{\sqrt{2\sigma^2_{\ln I}}}\right], \tag{4}$$

respectively; where $\sigma^2_{\ln I}$ is the variance of the log-irradiance, and it is related to the scintillation index by

$$\sigma^2_{\ln I} = \ln\left(\sigma_I^2+1\right). \tag{5}$$

4.2.2 Gamma-Gamma distribution

The PDF and probability of fade of a random variable I described by the Gamma-Gamma distribution are given by [12]

$$f_I(I) = \frac{2(\alpha\beta)^{\frac{\alpha+\beta}{2}}}{\Gamma(\alpha)\Gamma(\beta)}I^{\frac{\alpha+\beta}{2}-1}K_{\alpha-\beta}\left(2\sqrt{\alpha\beta I}\right), \quad I>0, \tag{6}$$

and

$$\begin{aligned}P_{fa}(F_T) =& \frac{\pi\text{csc}(\pi(\alpha-\beta))}{\Gamma(\alpha)\Gamma(\beta)}\left[\frac{(\alpha\beta)^\beta e^{-0.23\beta F_T}}{\beta\Gamma(\beta-\alpha+1)}\,{}_1F_2\left(\beta;\beta+1,\beta-\alpha+1;\alpha\beta e^{-0.23F_T}\right)\right.\\ &\left.-\frac{(\alpha\beta)^\alpha e^{-0.23\alpha F_T}}{\alpha\Gamma(\alpha-\beta+1)}\,{}_1F_2\left(\alpha;\alpha+1,\alpha-\beta+1;\alpha\beta e^{-0.23F_T}\right)\right]\end{aligned} \tag{7}$$

respectively; where $K_\nu(x)$ is the Macdonald function of order ν, defined in Eq. (B.2.1); and ${}_1F_2(\cdot)$ is the generalized hypergeometric function [See Appendix B.3]. The parameters α and β are directly related to the scintillation index (SI) by

$$\sigma_I^2 = \frac{1}{\alpha}+\frac{1}{\beta}+\frac{1}{\alpha\beta}. \tag{8}$$

4.2.3 Exponentiated Weibull distribution

The PDF and probability of fade of a random variable I described by the exponentiated Weibull distribution are given by

$$f_I(I) = \frac{\alpha\beta}{\eta}\left(\frac{I}{\eta}\right)^{\beta-1}\exp\left[-\left(\frac{I}{\eta}\right)^{\beta}\right]\left\{1-\exp\left[-\left(\frac{I}{\eta}\right)^{\beta}\right]\right\}^{\alpha-1}, \quad I>0, \tag{9}$$

and

$$P_{fa}(F_T) = \left\{1-\exp\left[-\frac{e^{-0.23\beta F_T}}{\eta^{\beta}}\right]\right\}^{\alpha}, \tag{10}$$

respectively; and the expressions for the distribution parameters have been found to approximately follow

$$\alpha \simeq \frac{7.220\sigma_I^{2/3}}{\Gamma\left(2.487\sigma_I^{2/6}-0.104\right)}, \tag{11a}$$

$$\beta \simeq 1.012(\alpha\sigma_I^2)^{-13/25}+0.142, \tag{11b}$$

$$\eta = \frac{1}{\alpha\Gamma(1+1/\beta)g_1(\alpha,\beta)}, \tag{11c}$$

where $g_1(\alpha,\beta)$ can be obtained by setting $n=1$ into Eq. (25) in Chapter 3, leading to

$$g_1(\alpha,\beta) = \sum_{j=0}^{\infty}\frac{(-1)^j\Gamma(\alpha)}{j!(j+1)^{1+\frac{1}{\beta}}\Gamma(\alpha-j)}; \tag{12}$$

which is a convergent series [105].

4.3 Bit Error-Rate

In any communication system the main metric to assess the link performance is the probability of error—also called bit error-rate (BER). Traditionally, the analysis of BER in the FSO community has been done by modeling the atmospheric turbulence as Lognormal, in the weak turbulence regime, and Gamma-Gamma, for the strong turbulence regime [30, 59, 106, 110–116]. In this section the BER performance is studied for the LN and GG distributions, along with the new proposed exponentiated Weibull model. Moreover, closed-form expressions for the bit error-rate are derived for the GG and EW models.

Assuming a free-space optical communication system using IM/DD with OOK modulation—a very common choice in FSO links [8]—, the word-error probability under atmospheric turbulence is given by [106]

$$\text{PWE} = \frac{1}{2}\int_0^{\infty}\text{erfc}\left(\frac{\text{SNR}_0\, I}{2\sqrt{2}}\right)f_I(I)dI, \tag{13}$$

where $\text{erfc}(\cdot)$ is the complementary error function and $f_I(I)$ is the PDF of irradiance fluctuations. Assuming a simple PIN receiver front-end the signal-to-noise ratio in

the absence of atmospheric turbulence is related to the average transmitted optical power P_t as $\mathrm{SNR}_0 = 2RP_t/\sigma_n$; where R is the receiver responsivity and σ_n is the noise standard deviation. Note that for OOK modulation, the bit-error probability P_b is the same as the word-error probability, i.e. $P_b = \mathrm{PWE}$ [78].

In order to provide a closed-form solution of Eq. (13) the $\mathrm{erfc}(x)$ can be expressed in terms of the Meijer's G-function $G_{p,q}^{m,n}[\cdot]$, defined in Eq. (B.4.1), using Eq. (B.4.2.3)

$$\mathrm{erfc}(x) = \frac{1}{\sqrt{\pi}} G_{1,2}^{2,0}\left[x^2 \middle| \begin{matrix} 1 \\ 0, \frac{1}{2} \end{matrix}\right],$$

leading to

$$P_b = \frac{1}{2\sqrt{\pi}} \int_0^\infty G_{1,2}^{2,0}\left[\frac{(\mathrm{SNR}_0\, I)^2}{8} \middle| \begin{matrix} 1 \\ 0, \frac{1}{2} \end{matrix}\right] f_I(I) dI, \tag{14}$$

Note that the Meijer's G-function can be found as a bult-in function in commercial software packages such as Mathematica and Maple. The particular implementation used here corresponds to the pure-Python open source library for multiprecision floating-point arithmetic `mpmath`, written by Johansson [117].

Next, new closed-form expressions for the bit-error rate under Gamma-Gamma and exponentiated Weibull turbulence are derived. It was not possible to obtain such expression for Lognormal turbulence due to the complex mathematical form of Eq. (3), thus, efficient numerical integration of Eq. (13) is used instead for the Lognormal case.

4.3.1 BER under Gamma-Gamma turbulence

To obtain the bit error-rate under GG turbulence first Eq. (6) is inserted into Eq. (14). By writing the Macdonald function of order $\alpha - \beta$ in terms of the Meijer's G-function using Eq. (B.4.2.4), then, the bit-error probability yields

$$P_b = \frac{(\alpha\beta)^{\frac{\alpha+\beta}{2}}}{2\sqrt{\pi}\Gamma(\alpha)\Gamma(\beta)} \int_0^\infty I^{\frac{\alpha+\beta}{2}-1} G_{1,2}^{2,0}\left[\frac{(\mathrm{SNR}_0\, I)^2}{8} \middle| \begin{matrix} 1 \\ 0, \frac{1}{2} \end{matrix}\right] G_{0,2}^{2,0}\left[\alpha\beta I \middle| \begin{matrix} - \\ \frac{\alpha-\beta}{2}, \frac{\beta-\alpha}{2} \end{matrix}\right] dI. \tag{15}$$

This integral can be solved using the convenient property that the integral of the product of two G-functions yields another Meijer's G-function [See Eq. (B.4.3.2)] leading to

$$P_b = \frac{2^{\alpha+\beta-3}}{\pi\sqrt{\pi}\Gamma(\alpha)\Gamma(\beta)} G_{5,2}^{2,4}\left[2\left(\frac{\mathrm{SNR}_0}{\alpha\beta}\right)^2 \middle| \begin{matrix} \frac{1}{2}-\frac{\alpha}{2}, 1-\frac{\alpha}{2}, \frac{1}{2}-\frac{\beta}{2}, 1-\frac{\beta}{2}, 1 \\ 0, \frac{1}{2} \end{matrix}\right]. \tag{16}$$

Note that a similar expression has been derived before by Dang [118].

4.3.2 BER under exponentiated Weibull turbulence

To obtain the bit error-rate under EW turbulence first Eq. (9) is inserted into Eq. (14). Next, by making use of the Newton's generalized binomial theorem [See Eq. (D.28)]

the last term in Eq. (9) can be expanded and, thus, the bit-error probability yields

$$P_b = \frac{\alpha\beta}{2\eta\sqrt{\pi}} \sum_{j=0}^{\infty} \frac{(-1)^j \Gamma(\alpha)}{j!\Gamma(\alpha - j)} \times \int_0^{\infty} \left(\frac{I}{\eta}\right)^{\beta-1} \exp\left[-(1+j)\left(\frac{I}{\eta}\right)^{\beta}\right] G_{1,2}^{2,0}\left[\frac{(\mathrm{SNR}_0\, I)^2}{8} \,\middle|\, \begin{matrix} 1 \\ 0, \frac{1}{2} \end{matrix}\right] dI. \quad (17)$$

By using Eq. (B.4.2.1) to express the exponential function in terms of the Meijer's G-function, the probability of error can be written as

$$P_b = \frac{\alpha\beta}{2\eta\sqrt{\pi}} \sum_{j=0}^{\infty} \frac{(-1)^j \Gamma(\alpha)}{j!\Gamma(\alpha - j)} \times \int_0^{\infty} \left(\frac{I}{\eta}\right)^{\beta-1} G_{1,2}^{2,0}\left[\frac{(\mathrm{SNR}_0 I)^2}{8} \,\middle|\, \begin{matrix} 1 \\ 0, \frac{1}{2} \end{matrix}\right] G_{0,1}^{1,0}\left[(1+j)\left(\frac{I}{\eta}\right)^{\beta} \,\middle|\, \begin{matrix} - \\ 0 \end{matrix}\right] dI. \quad (18)$$

The above integral can be solved, by applying again Eq. (B.4.3.2), after making the transformation of variables $y = (I/\eta)^2$, resulting in

$$P_b = \frac{\alpha\beta\sqrt{k\pi}}{2\sigma(2\pi)^{\frac{\ell+k}{2}}} \left(\frac{\ell}{\sigma}\right)^{\frac{\beta}{2}-1} \sum_{j=0}^{\infty} \frac{(-1)^j \Gamma(\alpha)}{j!\Gamma(\alpha - j)} \times G_{2\ell,k+\ell}^{k,2\ell}\left[\left(\frac{\omega_j}{k}\right)^k \left(\frac{\ell}{\sigma}\right)^{\ell} \,\middle|\, \begin{matrix} \Delta(\ell, 1-\frac{\beta}{2}), \Delta(\ell, \frac{1}{2}-\frac{\beta}{2}) \\ \Delta(k,0), \Delta(\ell, -\frac{\beta}{2}) \end{matrix}\right], \quad (19)$$

where $\Delta(k,a) = \frac{a}{k}, \frac{a+1}{k}, \cdots, \frac{a+k-1}{k}$ [See Eq. (B.4.1.5)]; $\omega_j = 1 + j$, $\sigma = (\eta \mathrm{SNR}_0)^2/8$, and ℓ and k are integer numbers that satisfy $\ell/k = \beta/2$. Although Eq. (19) is given in terms of an infinite summation, usually about 30 terms are needed for the series to converge.

The average BER closed-form expression, for an IM/DD FSO systems with OOK modulation under exponentiated Weibull turbulence, given in Eq. (19) was first published in [105]. Furthermore, an approximation of such expression has recently been derived using the generalized Gauss–Laguerre quadrature rule by Yi et al. [119].

4.4 Data Analysis

For the analysis of the probability of fade given in Sec. 4.2 and the new closed-form expressions for the BER derived above, both numerical simulation results and experimental data are used for different aperture sizes D, namely 3, 25, 60 and 80 mm. Under the simulation conditions used the 3 mm receiving aperture behaves as a point-like receiver, since it is smaller than the atmospheric coherence radius ρ_0 [94]. The analysis is performed for the LN, GG and EW models. The data sets presented here are the same as those used in Chapter 3.

For the simulation data, a wave optics code for the propagation of a Gaussian beam was used and set a link range $L = 1225$ m, a refractive-index structure constant $C_n^2 = 2.1 \times 10^{-14}$ m$^{2/3}$ and the wavelength $\lambda = 780$ nm. The simulation parameters reproduce conditions of moderate turbulence, with a Rytov variance $\sigma_R^2 =$

$1.23C_n^2k^{7/6}L^{11/6}$ of 1.35, where $k = 2\pi/\lambda$ is the wavenumber. A total of 30000 realizations were run to reduce the statistical uncertainties in the numerical simulations of the irradiance. A complete description of the simulation details can be found in Sec. 3.5.1 and Barrios et al. [102].

The probability of fade of the simulation data was obtained by calculating the cumulative distribution function of each data set, using 80 bins of equal width, and the count of each bin was associated with the midpoint of its respective bin width. When a zero-count bin is found its width is merged with the next bin to the right, thus, unequal bins were used whenever needed. Finally, the bit-error rate for simulation data was obtained by performing a numerical integration of Eq. (13) using the values of the simulation PDF presented in Fig. 3.5. All the results are shown in Fig. 4.1.

On the other hand, the experiments were conducted at Barcelona, Spain, between the rooftops of two buildings along a medium density residential terrain. A 780 nm continuous-wave diode laser at 15 mW (12 dBm), with built-in collimator, was used. The testbed selected for the experiments consisted in a nearly horizontal 1.2 km optical path. On the receiver side the light was detected using a 15 cm focal length Fresnel lens. A set of diaphragms was used so measurements for different aperture diameters were possible. A complete description of the experimental setup can be found in Sec. 3.5.3 and Barrios et al. [102].

Data was taken in individuals runs for the receiving apertures of 5 min at 10 kHz sampling rate each, hence, 3×10^6 samples were available to calculate the experimental probability of fade. The same procedure used for the simulation data was applied to estimate probability of fade and BER for the experimental data set. For the BER analysis the experimental PDF presented in Fig. 3.7 is used to perform the numerical integration of Eq. (13). All the results are shown in Fig. 4.2.

For the analysis of both data sets, in Figs. 4.1 and 4.2, the probability of fade is in the left column of each figure, while the BER plot are in the right column, for every receiving aperture tested. Moreover, some link parameters are given for the sake of direct comparison, namely, the scintillation index $\sigma_{I\text{data}}^2$ calculated directly from the simulation and experimental data, the Rytov variance as a measure of the turbulence strength, the ratio of the receiving aperture diameter to the atmospheric coherence length $\rho_0 = (1.46C_n^2k^2L)^{-3/5}$, and the aperture averaging factor A given by [24]

$$A = \left[1 + 0.333\left(\frac{kD^2}{4L}\right)^{5/6}\right]^{-7/5}.$$

All the data used here were presented in Chapter 3, where the corresponding PDF analysis has been done and the parameter values for each model plotted were obtained. The plots in Figs. 3.5 and 3.7 contain the corresponding PDF curves of Figs. 4.1 and 4.2, respectively. Recall that the $\sigma_{I\text{data}}^2$ value is used to estimate the LN (dotted line) and EW (dashed line) parameters, using Eq. (3) and Eq. (11), respectively. For the GG model (dash-dotted line) the parameter values are obtained from the fitting algorithm. In all figures a best fit version of the EW model (solid line) is also shown, allowing a direct comparison with the GG distribution. All the parameter values used to plot each curve are embedded in the corresponding subfigure.

For the analysis of the probability of fade, it has to be noted that higher values of the F_T threshold parameter correspond to lower values of the irradiance in the PDF,

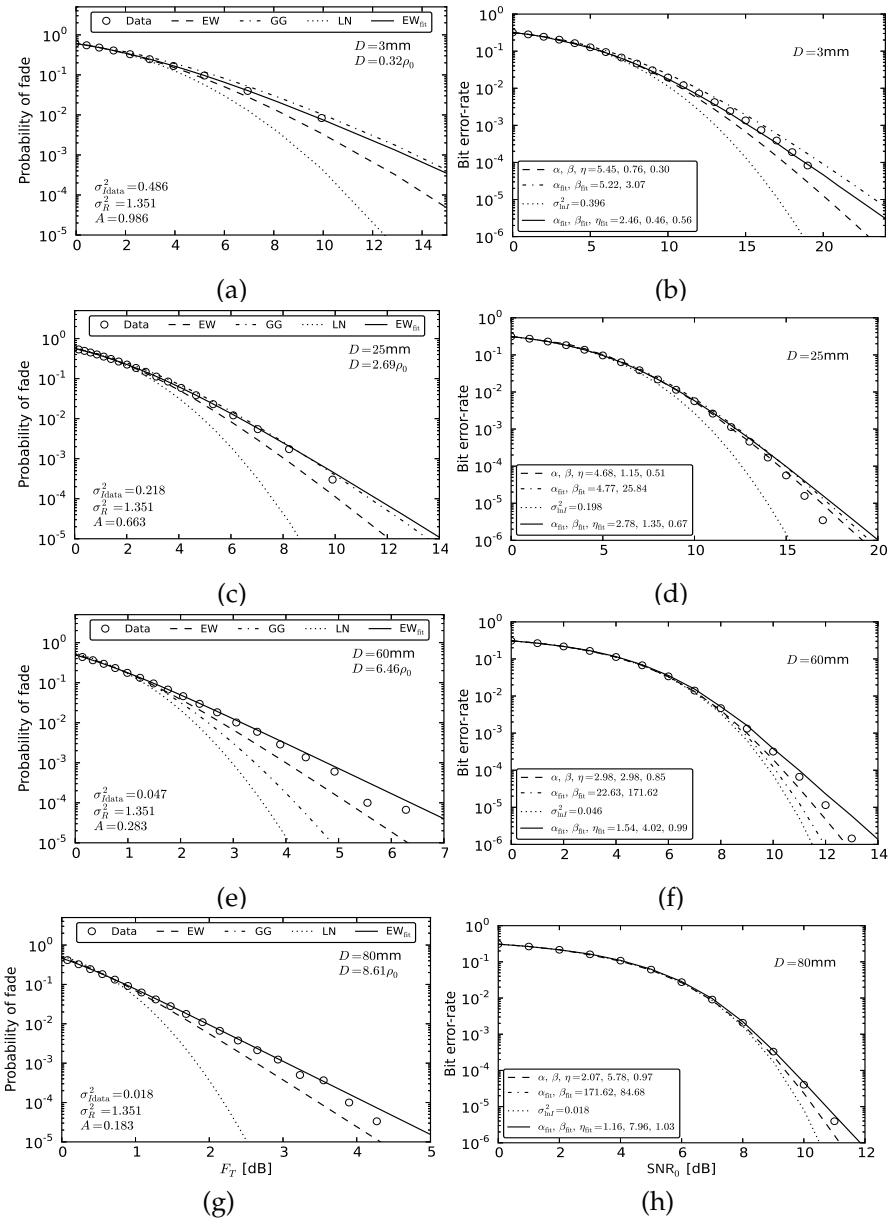

Figure 4.1 Probability of fade (left column) vs. fade threshold parameter F_T, and estimated BER (right column) vs. average signal-to-noise ratio (SNR_0) for numerical simulation results (circles), and various receiving aperture diameters.

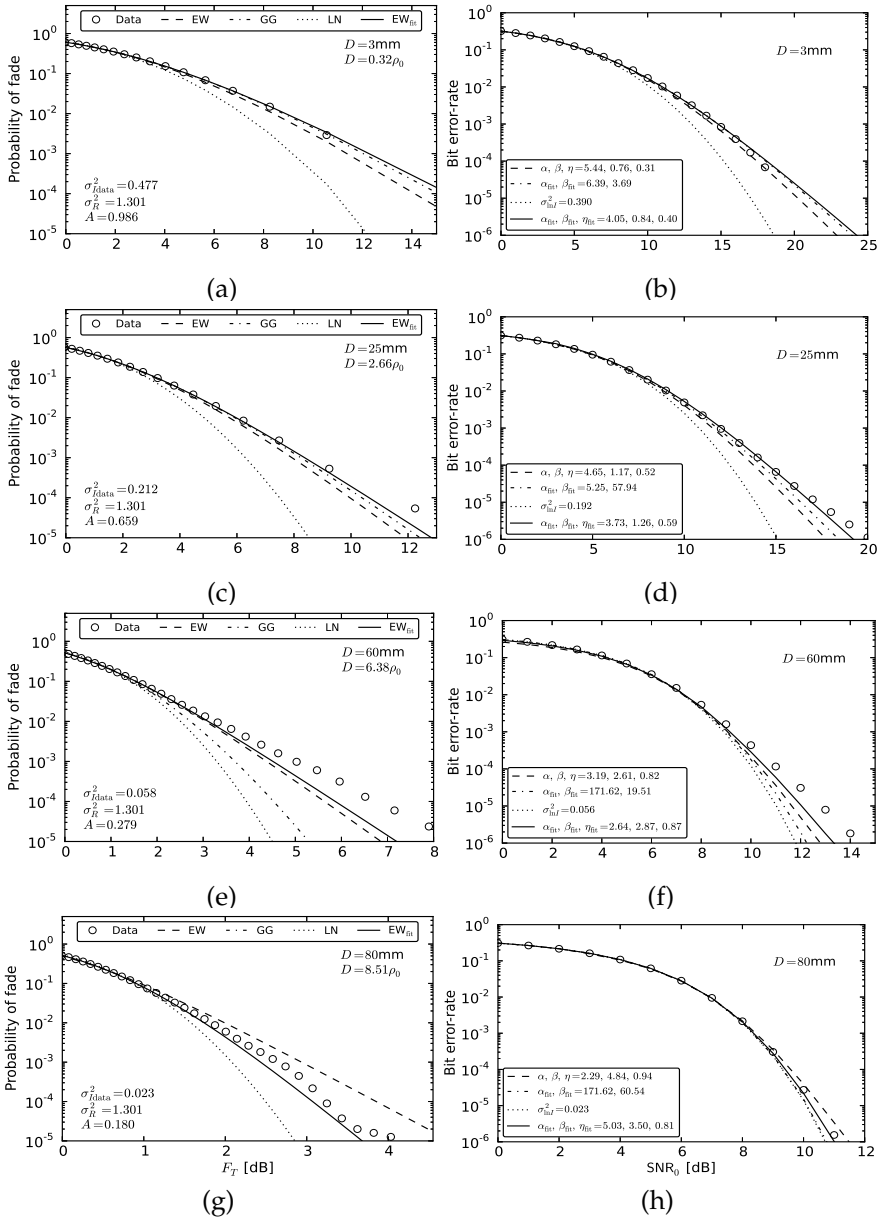

Figure 4.2 Probability of fade (left column) vs. fade threshold parameter F_T, and estimated BER (right column) vs. average signal-to-noise ratio (SNR_0) for experimental data (circles), and various receiving aperture diameters.

as expressed in Eq. (2). Having this in mind, it becomes evident that the behavior of the left tail in the PDF is somehow equivalent to the right side of the probability of fade plot. According to this, note how the relative position of each of the compared models maintains in Figs. 4.1 and 4.2, with respect to the PDF plots in Figs. 3.5 and 3.7. In the probability of fade curves the exponentiated Weibull model—fitted version—also presents the best fit to the corresponding data being evaluated. It is noteworthy to say that the probability of fade and the BER curves of the GG model for the 80 mm aperture are not plotted in both figures as the relatively high value of its parameters causes convergence problems in Eq. (7) and Eq. (16), respectively.

For the bit-error rate the new closed-form expressions derived in Sec. 4.3, for the GG and the EW model, were used. As mentioned before such expression is not available for the Lognormal distribution, thus, BER curves were obtained by direct numerical integration of Eq. (13) using the Lognormal PDF. Analyzing the BER plots, in both Figs. 4.1 and 4.2, it can be seen how all the tested models comply with the actual data up to about a signal-to-noise ratio of 8 dB, where the error rate is 10^{-2} or larger. After this point the LN model starts to deviate from the others, for all the cases presented here, unable to follow expected values. In the case of the 3 and 25 mm receiving aperture diameters the GG distribution has a close fit, and offers nearly the same prediction as the EW model. This situation is expected as for the PDF analysis both models have practically the same fit to the data. Nevertheless, for the 60 and 80 mm receiving aperture diameter cases the EW model offers a better prediction of the probability of fade and bit error-rate performance, as it can be seen in Figs. 4.1 and 4.2.

4.5 Bit Error-Rate with Pointing Errors

In the previous section BER performance analysis of an IM/DD FSO system under exponentiated Weibull fading, using OOK modulation, has been presented. Here, based on the work of Farid and Hranilovic [109], the BER analysis is extended to include the impact of pointing errors under exponentiated Weibull turbulence. Many other authors have utilized the model proposed in [109] with the atmospheric turbulence modeled by different distributions [111, 120–122].

Next, the FSO system and channel model is presented, along with the EW distribution, misalignment model, and overall combined channel statistics. The CDF is also derived for completeness. In Sec. 4.5.5 a new closed-form expression for the average BER in the case of FSO system with pointing errors, assuming OOK modulation, is derived. Section 4.5.6 is devoted to assess the new expression with Monte Carlo simulations, including the effects of aperture averaging, where the spherical wave approximation to a Gaussian beam is used to estimate the scintillation index. Lastly, some conclusions are given.

4.5.1 System and channel model

In this section an IM/DD FSO communication system with OOK modulation is considered. The signal-carrying laser beam propagates through the turbulent atmosphere, where traditionally the channel statistics have been assumed to be either

Lognormal or Gamma-Gamma. Here, the new proposed model is used, based on the exponentiated Weibull distribution. In addition, the impact of pointing errors is included in the analysis of the overall system performance.

For the receiver a collecting aperture of diameter D plus an avalanche photodetector (APD) is a typical configuration in FSO systems. In such conditions, for horizontal links, the additive white Gaussian noise (AWGN) channel is a good assumption, as although the output statistics of an APD are modeled by the McIntyre-Conradi distribution [73], the Gaussian approximation is sufficient enough when the bulk current is of the order of nanoamperes and the absorbed photons are more than a few hundreds within the observation time [123], mostly due to background optical power.

Therefore, the output signal y of a FSO system under the influence of atmospheric and misalignment fading, and additive noise, can be modeled as

$$y = Rhx + n, \tag{20}$$

where x is the transmitted optical power in watts, R is the receiver responsivity in A/W; whereas h represents the overall channel state, and n is the AWGN term with variance σ_n^2.

The channel induced fading $h = h_\ell h_a h_p$ is composed by three different factors, where two of them are random independent processes while the other is a deterministic factor. As explained in [109], the random terms h_p and h_a are the misalignment and atmospheric turbulence fading, respectively; and the atmospheric path loss h_ℓ—explained in Sec. 2.5.1—is considered to be deterministic, and without loss of generality, herein it is assumed that $h_\ell = 1$. Note that the time scales of the fading processes considered in FSO systems are in the order of milliseconds and, thus, the overall channel state h is assumed to be constant for a large number of transmitted bits [109].

4.5.2 Atmospheric turbulence

Let us assume, that the turbulence induced fading h_a can be modeled by an exponentiated Weibull distribution with PDF given by Eq. (9), and the distribution parameters are estimated with the expressions in Eq. (11). The parameters for the EW distribution can be directly related to atmospheric conditions, through the scintillation index σ_I^2, as indicated by Eq. (11). Recall that the SI for a finite receiving aperture with diameter D and zero inner scale of turbulence is given by [See Eq. (61) in Chapter 2]

$$\sigma_I^2(D) = \exp\left[\sigma_{\ln x}^2(D) + \sigma_{\ln y}^2(D)\right] - 1, \tag{21}$$

where $\sigma_{\ln x}^2$ and $\sigma_{\ln y}^2$ are the large-scale and small-scale log-irradiance flux variances, respectively, and assuming that the spherical wave is a good approximation at the receiver plane, they can be calculated as [124]

$$\sigma_{\ln x}^2(D) = \frac{0.49\beta_0^2}{\left(1 + 0.18d^2 + 0.56\beta_0^{12/5}\right)^{7/6}},$$
$$\sigma_{\ln y}^2(D) = \frac{0.51\beta_0^2(1 + 0.69\beta_0^2)^{-5/6}}{1 + 0.9d^2 + 0.62d^2\beta_0^{12/5}},$$

where $\beta_0^2 = 0.41\sigma_R^2$ is the Rytov variance of a spherical wave, and $d^2 = kD^2/4L$ is a normalization of the receiving aperture diameter. Note that the spherical wave approximation is valid for estimating the scintillation index of Gaussian beams when the link conditions produce a beam size at the receiver plane relatively larger than the collecting aperture size.

The atmospheric turbulence induced fading can be classified in a continuum of regimes, from weak to strong turbulence conditions, depending on the value of the Rytov variance σ_R^2. Thus, the weak fluctuations regime occurs when $\sigma_R^2 \ll 1$, and the strong fluctuations regime is associated with $\sigma_R^2 \gg 1$, while for $\sigma_R^2 \sim 1$ the regime is said to be moderate.

4.5.3 Misalignment fading

In a FSO link when a pointing error r is present, considering a circular receiver of radius a, the fraction of the collected power in the receiving plane can be approximated by $h_p(r, L) = A_0 \exp(-2r^2/W_{Leq}^2)$; where $A_0 = [\mathrm{erf}(\nu)]^2$ with $\nu^2 = \pi a^2/2W_L^2$, and $W_{Leq}^2 = w_L^2\sqrt{\pi}\,\mathrm{erf}(\nu)/(2\nu\exp(-\nu^2))$. Lastly, $\mathrm{erf}(\cdot)$ is the error function and W_L is the beam radius at the receiver plane [109].

The fading due to pointing errors h_p has been modeled as the result of considering independent identical Gaussian distributions, with variance σ_s^2, for the elevation and horizontal displacement (sway) [125]. Based on this assumption Farid and Hranilovic [109] developed a model for the statistics of the misalignment fading as

$$f_{h_p}(h_p) = \frac{\gamma^2}{A_0^{\gamma^2}} h_p^{\gamma^2-1}, \quad 0 \le h_p \le A_0, \tag{22}$$

where $\gamma = W_{Leq}/2\sigma_s$ is the ratio between the equivalent beam radius and the pointing error jitter at the receiver.

4.5.4 Combined channel statistics

The overall channel $h = h_p h_a$ term of the FSO model in Eq. (20) is modeled as the product of two i.i.d. random variables, thus, the statistics of h can be obtained as a conditional random process given a turbulence state h_a as

$$f_h(h) = \int f_{h|h_a}(h|h_a) f_{h_a}(h_a) dh_a.$$

Using Eq. (22) and applying standard statistical procedures, the channel state distribution gives [109]

$$f_h(h) = \frac{\gamma^2}{A_0^{\gamma^2}} h^{\gamma^2-1} \int_{h/A_0}^{\infty} h_a^{-\gamma^2} f_{h_a}(h_a) dh_a. \tag{23}$$

By applying the Newton's generalized binomial theorem to expand the last term in Eq. (9) and inserting the result in Eq. (23), the PDF of h yields

$$f_h(h) = \frac{\alpha\gamma^2}{\eta A_0}\left(\frac{h}{\eta A_0}\right)^{\gamma^2-1} \sum_{j=0}^{\infty} \frac{(-1)^j \Gamma(\alpha)}{j!\Gamma(\alpha-j)\omega_j^{1-\gamma^2/\beta}} \Gamma\left[1 - \frac{\gamma^2}{\beta},\ \omega_j\left(\frac{h}{\eta A_0}\right)^{\beta}\right], \tag{24}$$

where $\omega_j = 1 + j$, and $\Gamma(a, z)$ is the upper incomplete Gamma function, defined in Eq. (B.1.4). Although Eq. (24) is given in terms of an infinite summation this is a fast convergent series.

Now, the cumulative distribution function is obtained by integration of Eq. (24). To provide a compact closed-form solution of such integral, the upper incomplete Gamma function is expressed in terms of the Meijer's G-function using Eq. (B.4.2)

$$\Gamma(a, x) = G_{1,2}^{2,0}\left[x \,\middle|\, \begin{matrix} 1 \\ 0, a \end{matrix}\right].$$

Next, by applying Eq. (B.4.3.1) the CDF of h gives

$$F_h(h) = \frac{\alpha\gamma^2}{\beta}\left(\frac{h}{\eta A_0}\right)^{\gamma^2} \sum_{j=0}^{\infty} \frac{(-1)^j \Gamma(\alpha)}{j!\Gamma(\alpha - j)\omega_j^{1-\gamma^2/\beta}} G_{2,3}^{2,1}\left[\omega_j \left(\frac{h}{\eta A_0}\right)^{\beta} \,\middle|\, \begin{matrix} 1, 1 - \frac{\gamma^2}{\beta} \\ 0, 1 - \frac{\gamma^2}{\beta}, -\frac{\gamma^2}{\beta} \end{matrix}\right]. \tag{25}$$

4.5.5 Average bit error-rate

Assuming on-off keying modulation, the transmitted signal x is either 0 or $2P_t$; where P_t is the average transmitted optical power. Then, the average bit error probability under fading h is given, as in Eq. (13), by [106]

$$P_b = \frac{1}{2}\int_0^{\infty} \operatorname{erfc}\left(\frac{\mathrm{SNR}_0\, h}{2\sqrt{2}}\right) f_h(h) dh, \tag{26}$$

where $\mathrm{SNR}_0 = 2RP_t/\sigma_n$ is the signal-to-noise ratio in the absence of channel induced fading, $\operatorname{erfc}(\cdot)$ is the complementary error function, and $f_h(h)$ is the PDF of the channel state, derived in the previous section.

To find a closed-form expression for Eq. (26) the same strategy followed to solve Eq. (14) is used here. The complementary error function $\operatorname{erfc}(\cdot)$ is rewritten using Eq. (B.4.2.3), and when misalignment is present in a FSO system the average BER is obtained by using Eq. (24) as the PDF statistics of the overall fading channel. Next, applying Eq. (B.4.3.2) and solving yields

$$\begin{aligned} P_b =& \frac{\alpha\gamma^2\sqrt{\pi k^{1-2\gamma^2}}}{2\sigma(2\pi)^{\frac{\ell+k}{2}}}\left(\frac{\ell}{\sigma}\right)^{\frac{\gamma^2}{2}-1} \sum_{j=0}^{\infty} \frac{(-1)^j\Gamma(\alpha)}{j!\Gamma(\alpha-j)\omega_j^{1-\gamma^2/\beta}} \\ &\times G_{2\ell+k,2k+\ell}^{2k,2\ell}\left[\left(\frac{\omega_j}{k}\right)^k \left(\frac{\ell}{\sigma}\right)^{\ell} \,\middle|\, \begin{matrix} \Delta(\ell, 1-\frac{\gamma^2}{2}), \Delta(\ell, \frac{1}{2}-\frac{\gamma^2}{2}), \Delta(k, 1) \\ \Delta(k, 0), \Delta(k, 1-\frac{\gamma^2}{\beta}), \Delta(\ell, -\frac{\gamma^2}{2}) \end{matrix}\right], \end{aligned} \tag{27}$$

where $\Delta(k, a)$ is defined by Eq. (B.4.1.5); $\sigma = (\eta\mathrm{SNR}_0)^2/8$, and ℓ and k are integer numbers that satisfy $\ell/k = \beta/2$ as in Eq. (19).

4.5.6 Monte Carlo simulations

Some numerical simulation results are shown in Figs. 4.3–4.5, where an FSO system with OOK modulation is analyzed in terms of its BER performance in the presence

of atmospheric turbulence and misalignment fading under aperture averaging conditions.

To conduct the analysis the link parameters were set to emulate common values encountered in real FSO systems. Therefore, the link distance, divergence and beam size at the receiver are set as reported by Wayne et al. [14], where the laser source is used in combination with a beam expander to achieve a good approximation to a spherical wave at the receiver plane. To assess the impact of aperture averaging in such system three different receiving aperture sizes are tested, with diameters 200, 100 and 50 mm. Furthermore, in order to study the influence of the atmospheric turbulence three distinct values, reported in [14, 122], of the refractive-index structure parameter were used—corresponding to weak, moderate and strong turbulence regimes. A complete list of the link parameters and their values is presented in Table 1.

For the simulation results the Monte Carlo method was used, and 10000 channel conditions tested. The overall channel state was obtained by using the inverse CDF method to draw random values from the atmospheric turbulence and misalignment fading models, and then multiplying them, since both are assumed to be independent processes. To obtain the BER statistics, blocks of 10^4 bits are transmitted through the FSO link model in Eq. (20) until a minimum of 100 errors are found or a maximum of 10^7 bits are transmitted, for each SNR condition. This helps to keep reasonable simulation runtimes.

In every scenario tested turbulence-only conditions are simulated, as well as turbulence plus pointing errors with jitter $\sigma_s = 30$ cm—presented as a standard value in Farid and Hranilovic [109]. Taking into account the receiving apertures used the normalized jitters are $\sigma_s/a = 3, 6, 12$; where higher values indicate higher impact of pointing errors. Moreover, the normalized beam widths are $W_L/a = 20, 40, 80$; where higher values indicate higher impact of atmospheric turbulence, due to lower aperture averaging.

In Figs. 4.3–4.5 the average BER is presented in terms of the signal-to-noise ratio, for a single receiving aperture size. Monte Carlo simulation results are shown in circles, while the predictions of the closed-form expressions in Eq. (19) and Eq. (27) are plotted as lines; where weak (solid line), moderate (dashed line) and strong (dotted line) turbulence conditions are shown. Additionally, the exponentiated Weibull

Table 1 FSO System Configuration

Description	Parameter	Value
Optical transmitted power	P_t	$[-40, 20]$ dBm
Optical wavelength	λ	780 nm
Weak turbulence	C_n^2	7.2×10^{-15} m$^{-2/3}$
Moderate turbulence	C_n^2	5.0×10^{-14} m$^{-2/3}$
Strong turbulence	C_n^2	3.6×10^{-13} m$^{-2/3}$
Beam half-angle divergence	θ	2 mrad
Link distance	L	1000 m
Beam radius at receiver	w_L	2 m
Receiver responsivity	R	0.5 A/W
Noise standard deviation	σ_n	1×10^{-17} A/Hz
Pointing errors jitter std.	σ_s	30 cm
Receiving aperture diameter	$D = 2a$	$200, 100, 50$ mm

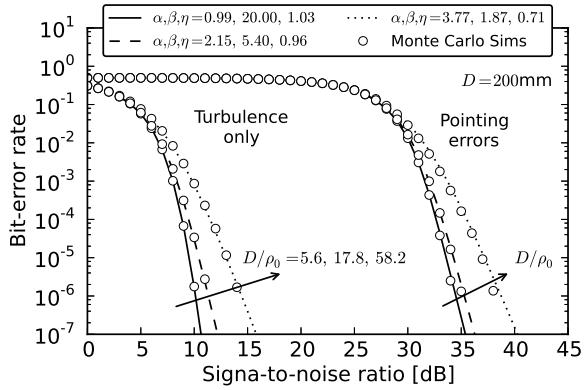

Figure 4.3 BER performance assuming normalized pointing errors jitter $\sigma_s/a = 3$ and $W_L/a = 20$ in weak (solid), moderate (dashed) and strong (dotted) turbulence regimes with increasing Rytov variance $\sigma_R^2 = 0.32, 2.22, 15.97$; respectively.

parameters values—predicted with Eq. (11)— are given for each scenario, using the scintillation index estimated with Eq. (21). Lastly, the ratio of the aperture diameter D to the coherence length ρ_0 is shown, where the sense of increment of D/ρ_0 is indicated with an arrow. For spherical waves the coherence radius is $\rho_0 = (0.55C_n^2k^2L)^{-3/5}$.

In Fig. 4.3 the receiving aperture $D = 200$ mm is analyzed. It is readily seen the major impact of the misalignment fading ($\sigma_s = 30$ cm) on system performance, where there is about a 25 dB penalty to achieve a 10^{-7} bit error-rate performance—herein this is the reference BER value when referring to decibel penalties—, respect to a turbulence only scenario, in all the regimes of turbulence tested. As expected, the performance is undermined as the turbulence strength increases, and about a 5 dB difference is seen between weak and strong turbulence regime—either if pointing errors are present or not.

In Fig. 4.4 the receiving aperture size is 100 mm, half of that in Fig. 4.3. Here, it is noteworthy to say that, when going from $D = 200$ to 100 mm, for turbulence only conditions there is only 1 dB and 4 dB difference, considering weak and strong turbulence regime, respectively; whereas this penalty increases to 7 dB and 11 dB when pointing errors are included in the analysis. It can be inferred that in the presence of misalignment fading aperture averaging offers even better performance in the FSO link, when compared with turbulence only conditions. The penalty in BER performance is about 30 dB when misalignment is present, respect to a turbulence only scenario.

The results for the receiving aperture size $D = 50$ mm are shown in Fig. 4.5. This is the smallest aperture size tested here and it becomes evident, as expected, that it provides the worst BER performance. As the ratio D/ρ_0 indicates, in weak and moderate turbulence the aperture is not capable of producing effective aperture averaging, thus, demanding higher SNR values to achieve any given BER value. In strong turbulence, although the aperture size should provide a fair amount of aperture averaging as $D/\rho_0 > 10$, the coherence radius is $\rho_0 = 3.4$ mm indicating a severe loss of the light source coherence, and in such conditions it is well known that the atmo-

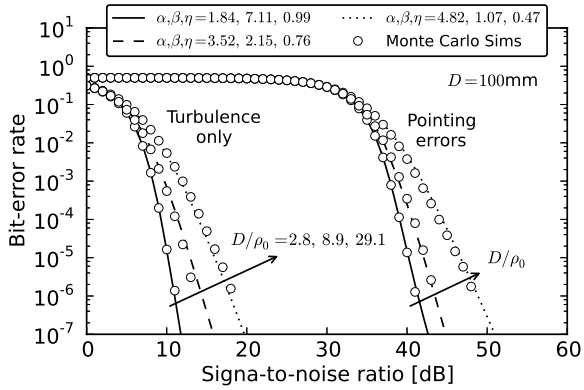

Figure 4.4 BER performance assuming normalized pointing errors jitter $\sigma_s/a = 6$ and $W_L/a = 40$ in weak (solid), moderate (dashed) and strong (dotted) turbulence regimes with increasing Rytov variance $\sigma_R^2 = 0.32, 2.22, 15.97$; respectively.

spheric turbulence imposes a larger impact than the countermeasures that aperture averaging can provide.

From the analysis of the three different aperture sizes, in Figs. 4.3–4.5, the performance in weak turbulence conditions with no misalignment is relatively similar, as there is only a 3 dB difference between the largest and smallest apertures. This situation may be explained as the scale sizes of the aperture diameter relative to the coherence radius are comparable—if the convention that D is much larger than ρ_0 when $D/\rho_0 > 10$ is established—and, therefore, they represent similar aperture averaging scenarios. In the moderate and strong turbulence regimes this difference is of about 8 dB, in both cases, as the ratio D/ρ_0 is no longer comparable for the three

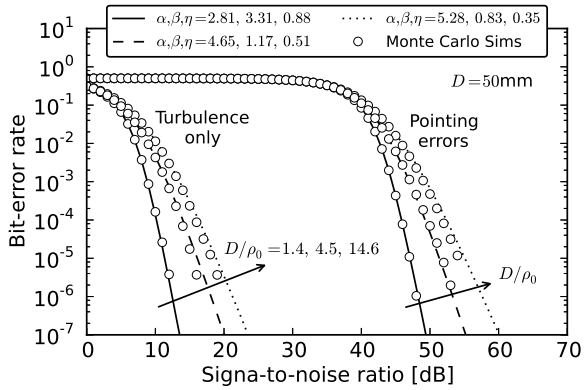

Figure 4.5 BER performance assuming normalized pointing errors jitter $\sigma_s/a = 12$ and $W_L/a = 80$ in weak (solid), moderate (dashed) and strong (dotted) turbulence regimes with increasing Rytov variance $\sigma_R^2 = 0.32, 2.22, 15.97$; respectively.

apertures.

When pointing errors are considered in weak turbulence, although the aperture averaging conditions can be comparable, the impact of misalignment is larger and there is a penalty of 14 dB, when going from a receiving aperture $D = 200$ mm to 50 mm. A similar situation is seen for moderate and strong turbulence regimes, where this penalty is even higher with 18 and 20 dB, respectively.

4.6 Summary

To summarize, free-space optical communication links based on an IM/DD system, using OOK modulation, have been studied in terms of the probability of fade and bit error-rate performance.

Numerical simulation results and experimental data have been used to study the probability of fade and BER performance of FSO communications links in the turbulent atmosphere. The main goal of this analysis was to contrast the new proposed fading model, namely, exponentiated Weibull, with the most accepted models nowadays in the FSO community. Additionally, new closed-form BER expressions have been derived for the Gamma-Gamma and exponentiated Weibull fading channel models, for OOK modulation, by making use of the Meijer's G-function.

The analysis presented here suggests that the better fit to the actual data are the predictions made by the EW model. Although part of the analysis has been done by estimating the parameters of each model from curve fitting algorithms, estimated parameters using Eq. (11) were also used to assess the EW distribution. The parameter estimation made by such equations, for the EW model, outperforms the prediction made by fitted GG model, in the 60 and 80 mm receiving aperture diameter cases for both simulation and experimental data.

It was seen that whenever a model has a close fit to the PDF of the irradiance data—by contrasting to Fig. 3.5 and Fig. 3.7—, then the probability of fade and the bit-error rate have a close fit too, accordingly.

Furthermore, the BER expression has been extended to account for pointing errors when the atmospheric turbulence is assumed to follow the exponentiated Weibull fading model, and a new closed-form expression has been derived.

To assess this new expression Monte Carlo simulations have been conducted. For this study the link parameters were set to values previously reported in the literature, to provide a realistic scenario, allowing to include weak-to-strong turbulence regimes in the analysis, as well as the impact of aperture averaging, by the use of three different receiving aperture sizes. Monte Carlo simulations for turbulence only conditions have also been presented here for completeness of the analysis, and also to test the closed-form BER expression derived in Sec. 4.3.2.

From the analysis of the BER plots presented here, it can be concluded that the influence of the aperture averaging has a larger impact in the presence of pointing errors, relative to that of turbulence only conditions. For instance, to achieve a 10^{-7} BER performance, considering no misalignment fading and strong turbulence, there is a 7 dB improvement in passing from a receiving aperture $D = 50$ mm to 200 mm; whereas, when pointing errors are included, this improvement is about 20 dB.

Finally, as the PDF fit for the exponentiated Weibull model has been demonstrated

in the weak-to-strong turbulence regime under numerous aperture averaging conditions in Chapter 3, the EW fading channel model can be regarded as an excellent candidate to accurately predict the probability of fade and the BER performance of laser beam propagating through atmospheric turbulence under the presence of aperture averaging.

5

The Exponentiated Weibull Model with Partially Coherent Beams

THE PURPOSE of this chapter is to evaluate the validity of the exponentiated Weibull fading channel for partially coherent beams (PCB), based on the Gaussian Schell-model. A recently reported simulation approach is used for the analysis of a PCB propagating under atmospheric turbulence in the presence of aperture averaging.

5.1 Introduction

The study presented up to this point for the exponentiated Weibull (EW) fading channel, in free-space optical (FSO) communications through the turbulent atmosphere, has been entirely based on coherent beams. It has been shown, in Chapter 2, how these types of beams are affected by atmospheric turbulence and the corresponding theory to estimate the beam size, beam wander, angle-of-arrival fluctuations, and scintillation index (SI) has also been presented. Among these effects, the most important metric for FSO communications is the latter where the lower the SI the better the performance of the communication system, as it will be less affected by the intensity fluctuations caused by the atmospheric turbulence.

The most common technique to fight against the turbulence induced fading in FSO links is the aperture averaging method, in which a collecting telescope is used as a receiving optical antenna, instead of a bear photodetector [17, 20, 23, 24, 32]. The received wavefront can be regarded as a self-interference pattern, produced by atmospheric inhomogeneities of different spatial scale sizes, that is averaged over the entire receiving area, and thus the intensity fluctuations are mitigated, therefore, reducing the scintillation index. Other atmospheric turbulence mitigation methods used rely on active and adaptive optics [29–31].

In the past decade the interest in *spatially* partially coherent beam (PCB) waves has been constantly growing, as yet another mitigation technique to counterbalance the effects of atmospheric turbulence over the signal-carrying laser beam in FSO links [25, 27, 126–131]. By reducing the coherence length l_c of the initial light source there is also a reduction on the SI at the receiver plane—at the expense of lower received optical power—, therefore, the use of a PCB is often regarded as *transmitter aperture averaging* [132].

The vast majority of works on partially coherent beams rely on the Gaussian Schell-model (GSM) beams [133] to account for the coherence degree of the light source used at the transmitter side. In the GSM theory the PCB generated beam field amplitude distribution and spatial coherence function are both Gaussian. It is noteworthy that the practical generation of a PCB is still a difficult task. To achieve a Gaussian-like beam the GSM theory requires that a large number of random PCBs are averaged at the receiver within the observation time, i.e. the bit time [134]. One way to create a partially coherent beams is using a spatial light modulator (SLM) to control the phase of a fully coherent light source, by rapidly applying a series of random phase realizations following the desired statistics—Gaussian in the GSM case. Current SLM technology does not permit to achieve refresh rate scales shorter than bit-time for high-speed communications, although work is being done in this regard [135].

The remainder of this chapter is devoted to present the basic Gaussian Schell-model theory in Sec. 5.2, and a recently developed approach [136, 137]—based on the GSM—to simulate partially coherent beams in Sec. 5.2.1. Moreover, in Sec. 5.3, this simulation technique is utilized to assess if the exponentiated Weibull model is still valid for a PCB propagating in atmospheric turbulence in the presence of aperture averaging, and comparisons are made to the Lognormal and Gamma-Gamma PDF models. Finally, some conclusions are given in Sec. 5.4.

5.2 Gaussian Schell-Model

To create a partially coherent beam one must have control over the (spatial) phase of the initial beam. A PCB can be generated in different ways, the most simple of which is to place a diffuser at the transmitter of a quasi-monochromatic laser source [127]. A propagation scheme for a GSM beam, generated with a diffuser, is shown in Fig. 5.1.

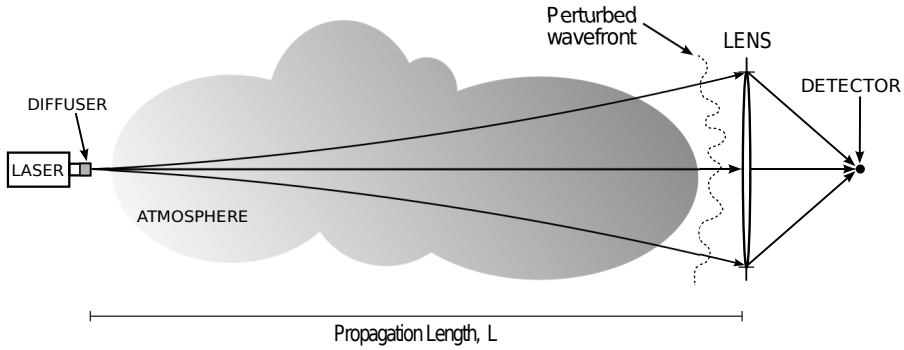

Figure 5.1 Propagation scheme of a partially coherent Gaussian beam.

Hereafter, the light source is assumed to be a collimated coherent optical beam, with Gaussian profile, that can be characterized by its input dimensionless parameters [See Sec. 2.3]

$$\Theta_0 = 1; \quad \Lambda_0 = \frac{2L}{kW_0^2}, \tag{1}$$

where W_0 is the beam radius at the transmitter plane; and $k = 2\pi/\lambda$ is the wavenumber, being λ the optical wavelength. The output parameters, for a system without the diffuser, at the receiver plane $z = L$ are

$$\Theta = \frac{\Theta_0}{\Theta_0^2 + \Lambda_0^2}; \quad \Lambda = \frac{\Lambda_0}{\Theta_0^2 + \Lambda_0^2}. \tag{2}$$

If the effects of the diffuser placed at the transmitter located at $z = 0$ are included, as shown in Fig. 5.1, the field of the optical wave emerging from the diffuser is modeled by

$$\widetilde{U}_0(\vec{r}, 0) = U_0(\vec{r}, 0) \exp\left[i\varphi(\vec{r})\right], \tag{3}$$

where $U_0(\vec{r}, 0)$ is the light source optical field before the diffuser, $\vec{r}$ is a transverse vector, $\varphi(\vec{r})$ is a random phase with zero mean, and $\widetilde{U}_0(\vec{r}, 0)$ is the *effective source* [32]. The diffuser can be modeled by a thin random phase screen characterized by a single-scale Gaussian spectrum model [127]

$$\Phi_\varphi(\kappa) = \frac{\langle n_1^2 \rangle \, l_c^3}{8\pi\sqrt{\pi}} \exp\left(-\frac{1}{2} l_c^2 \kappa^2\right), \tag{4}$$

where κ is the scalar spatial frequency; $\langle n_1^2 \rangle$ denotes the fluctuation of the index of refraction associated with the diffuser, and l_c is the lateral coherence length—the only effective scale associated with the diffuser.

Alternatively, the diffuser can also be modeled through the autocorrelation function of Eq. (3), that it is customary to be described by a Gaussian function in the GSM as

$$\begin{aligned} R_{\widetilde{U}_0}(\vec{r}_1,\vec{r}_2) &= \left\langle \widetilde{U}_0(\vec{r}_1,0)\widetilde{U}_0^*(\vec{r}_2,0)\right\rangle \\ &= U_0(\vec{r}_1,0)U_0^*(\vec{r}_2,0)\left\langle \exp\left[i\varphi(\vec{r}_1)\right]\exp\left[-i\varphi(\vec{r}_2)\right]\right\rangle \\ &= U_0(\vec{r}_1,0)U_0^*(\vec{r}_2,0)\exp\left[-\frac{|\vec{r}_1-\vec{r}_2|^2}{2\sigma_f^2}\right] \end{aligned} \tag{5}$$

where σ_f^2 is the variance of the Gaussian function describing the ensemble average of the random phases; and is related to the lateral coherence length of the diffuser by $l_c^2 = 2\sigma_f^2$.[†] Note that if $\sigma_f^2 \to \infty$ —consequently l_c also tends to infinity—then the exponential factor in Eq. (5) vanishes and the source is essentially a coherent wave, whereas if σ_f^2 is comparable in size with the beam radius the source starts to act like an incoherent source. Indeed, if the coherence radius of the beam after passing through the diffuser is significantly smaller than the beam radius, the process of propagation of the laser beam can be considered as the independent propagation of a large number of coherent beams [128]. The effective number of independent propagation paths or *speckle cells* is described by the source coherence parameter defined as [127]

$$\zeta_S = 1 + \frac{2W_0^2}{l_c^2}. \tag{6}$$

Now, all the theory developed for coherent waves [Refer to Chap. 2] can be extended to account for partially coherent beam waves, using the Gaussian Schell-model. Thus, the beam size of a PCB in turbulence, at the receiver plane $z = L$, is defined as

$$W_\zeta = W_0\sqrt{\Theta_0^2 + \zeta\Lambda_0^2}. \tag{7}$$

Note that Eq. (7) is virtually the same as Eq. (24) in Chap. 2, except for the global coherence parameter ζ defined as

$$\zeta = \zeta_S + \frac{2W_0^2}{\rho_0^2}, \tag{8}$$

where $\rho_0 = (0.55C_n^2k^2L)^{-3/5}$ is the coherence radius for a spherical wave.

Additionally, the average intensity for a unit-amplitude GSM beam after propagating a distance $z = L$, i.e. at the receiver side, can be expressed as

$$\langle I(r)\rangle = \frac{W_0^2}{W_\zeta^2}\exp\left(-\frac{2r^2}{W_\zeta^2}\right), \tag{9}$$

where r is the radial distance from the optical axis.

[†]Note that σ_f^2 is traditionally denoted as σ_g^2 in the literature. Here, the notation has been changed to keep consistency with the rest of the manuscript.

Finally, the effective output parameters of a partially coherent beam wave are affected by the source coherence parameter in Eq. (6) resulting in

$$\Theta_e = \frac{\Theta_0}{\Theta_0^2 + \Lambda_0^2 \zeta_S}; \quad \Lambda_e = \frac{\Lambda_0 \zeta_S}{\Theta_0^2 + \Lambda_0^2 \zeta_S}. \tag{10}$$

These effective output parameters can be replaced *ad-hoc* in Eq. (59) and Eq. (61) of Chap. 2, to estimate the scintillation index for a point receiver and a finite aperture receiver, respectively.

5.2.1 Simulation approach for GSM beams

Traditionally the analysis of partially coherent beams has been done based on theoretical studies [25, 27, 126, 127, 129–131], until very recently Xiao and Voelz [137] developed a wave optics simulation method to generate a PCB relying on the Gaussian Schell-model, and a number of works have been published based on this method [132, 135, 138, 139]. This technique consists in applying a series of random phase screens—following Gaussian statistics—to the initial beam wave at the transmitter end, thus, at the receiver plane the final intensity profile resulting from the summation of the incoming waves can be regarded as a partially coherent beam. Some recent experimental results, utilizing a SLM based setup, are also available [135].

Now, in the Gaussian Schell-model the random phase screen is denoted by $\varphi(\vec{r})$ in Eq. (3); where $\vec{r} = (x, y)$ is a point in the transverse plane of the propagating optical field, and is related to the radial distance by $r^2 = x^2 + y^2$. This random phase screen is now defined in terms of the convolution of two functions

$$\varphi(x, y) = r(x, y) \otimes g(x, y), \tag{11}$$

where $r(x, y)$ is a uniform random variable with probability density function (PDF) given by [136]

$$f_r(x, y) = \begin{cases} \dfrac{1}{C}, & -\dfrac{C}{2} < x, y < \dfrac{C}{2} \\ 0, & \text{otherwise} \end{cases} \tag{12}$$

and $g(x, y)$ is a Gaussian filter defined as [137]

$$g(x, y) = \frac{1}{2\pi\sigma_g^2} \exp\left(-\frac{x^2 + y^2}{2\sigma_g^2}\right), \tag{13}$$

where σ_f^2 is a transverse spatial correlation length parameter.

In the Gaussian Schell-model theory the autocorrelation of the transmittance of the GSM random phase screen $T(x, y) = \exp[i\varphi(x, y)]$ is assumed to be a Gaussian function, as shown in the last term of Eq. (5). Therefore, this correlation function can be expressed as

$$R_\varphi(x, y) = \exp\left(-\frac{\sigma_{\Delta\varphi}^2}{2}\right), \tag{14}$$

where $\sigma^2_{\Delta\varphi} = \left\langle (\varphi(x_1, y_1) - \varphi(x_2, y_2))^2 \right\rangle$ is the variance of the difference random phase $\Delta\varphi$. As the phase can be considered stationary, and taking that φ is a convolution of two functions as shown in Eq. (11), then $\sigma^2_{\Delta\varphi}$ can be taken to be [136]

$$\sigma^2_{\Delta\varphi} = R_r(\Delta p, \Delta q) \otimes [g(\Delta p, \Delta q) \otimes g^*(-\Delta p, -\Delta q)], \tag{15}$$

where $\Delta p = x_2 - x_1$ and $\Delta q = y_2 - y_1$.

For a random signal governed by the PDF in Eq. (12), the autocorrelation function is found to be

$$R_r(\Delta p, \Delta q) = \sigma_r^2 \delta(\Delta p, \Delta q), \tag{16}$$

where $\delta(\Delta p, \Delta q)$ is the delta function, and $\sigma_r^2 = C^2/12$ is a parameter related to the amplitude variation of the random phase screen $\varphi(x, y)$ [137].

Additionally, the second part of Eq. (15) can be calculated as

$$g(\Delta p, \Delta q) \otimes g^*(-\Delta p, -\Delta q) = \frac{1}{4\pi\sigma_g^2} \exp\left[-\frac{(\Delta p + \Delta q)^2}{4\sigma_g^2}\right]. \tag{17}$$

Next, inserting Eq. (16) and Eq. (17) into Eq. (15), and using the result in Eq. (14) yields

$$R_\varphi(\Delta p, \Delta q) = \exp\left\{-\frac{\sigma_r^2}{4\pi\sigma_g^2}\left[1 - \exp\left(-\frac{\Delta p^2 + \Delta q^2}{4\sigma_g^2}\right)\right]\right\}. \tag{18}$$

Note that if $\sigma_r^2/(4\pi\sigma_g^2) \gg 1$, then Eq. (18) can be approximated by

$$R_\varphi(\Delta p, \Delta q) \approx \exp\left(-\frac{\Delta p^2 + \Delta q^2}{2\sigma_f^2}\right), \tag{19}$$

which is very similar to Eq. (5); and the variance of the Gaussian function is given by

$$\sigma_f^2 = \frac{8\pi\sigma_g^4}{\sigma_r^2}. \tag{20}$$

5.2.2 Simulation of a GSM beam under atmospheric turbulence

In the previous section the grounds to simulate a partially coherent beam wave were set. In the method described the average intensity profile of the propagated optical wave is Gaussian as expected by the GSM theory. Consequently, after applying M random phase screens the intensity profile of the source wave is given by

$$I(x, y) = \frac{1}{M} \sum_{j=0}^{M-1} \left| U_0(x, y) \exp\left[i\varphi_j(x, y)\right] \right|^2, \tag{21}$$

where $U_0(x, y)$ is the initial coherent beam and $\varphi_j(x, y)$ are the GSM random phase screens. In previous works a summation of 30 GSM screens has been used because it starts to bring in the Gaussian-like intensity profile in the computer simulations conducted [132, 135, 138].

In order to include the effects of atmospheric turbulence over a partially coherent beam various realizations of turbulence states are used. Then, the average intensity profile of a PCB for each realization n of atmospheric turbulence is given by

$$I_n(x,y) = \frac{1}{M}\sum_{j=0}^{M-1}\left|\mathscr{F}^{-1}\left\{\mathscr{F}\left\{U_0(x,y)\exp\left[i\varphi_j(x,y)\right]\right\}H(u,v)\right\}\exp\left[-i\theta_n(x,y)\right]\right|^2, \tag{22}$$

where $H(u,v)$ is a Fourier propagator defined as [50]

$$H(u,v) = \exp\left(-i\Delta z\frac{u^2+v^2}{2k}\right), \tag{23}$$

where $\mathscr{F}\{\cdot\}$ is the two-dimensional Fourier transform operator, Δz is the propagation length, u and v are spatial frequencies, and $\theta_n(x,y)$ corresponds to each of the turbulence phase screen realizations. Evidently, the process described by Eq. (22) is executed many times and the resulting fields are averaged to obtain the estimation of the intensity for a PCB propagating in a specific atmospheric turbulence condition. Note that Eq. (22) complies with the *beam propagation method* described in Sec. 2.4.

Herein, the turbulence phase screens $\theta_n(x,y)$ are generated using the spectral method described in Sec. 2.4.1, where the Kolmogorov power spectrum is used. Moreover, the resolution in the spatial frequencies around zero is improved by adding five subharmonics components to each of the turbulence random phase screen following the procedure proposed by Recolons and Dios [49].

5.3 Simulation Results of Partially Coherent Beams

In Chapter 2 the suitability of the proposed exponentiated Weibull fading channel was studied in terms of the PDF, and in Chapter 3 the analysis was in terms of the probability of fade and bit error-rate, obtaining promising results for the new model. All the work conducted in previous chapter dealt exclusively with fully coherent waves. Next, the EW is explored in its capabilities to model the fluctuations of the irradiance data for partially coherent beams under atmospheric turbulence in the presence of aperture averaging, by conducting some simulations and analyzing the PDF of the simulated data.

The atmospheric turbulence induced fading can be classified, depending on the value of the Rytov variance $\sigma_R^2 = 1.23C_n^2k^{7/6}L^{11/6}$, from weak to strong turbulence conditions. The weak fluctuations regime occurs when $\sigma_R^2 \ll 1$, and the strong fluctuations regime is associated with $\sigma_R^2 \gg 1$, while for $\sigma_R^2 \sim 1$ the regime is said to be moderate. Thus, to include different atmospheric conditions in the simulation analysis the value of the refractive-index structure parameter C_n^2 is set to 7.2×10^{-15}, 5.0×10^{-14} and 3.6×10^{-13} $\mathrm{m}^{-2/3}$ in order to reproduce the weak, moderate and strong turbulence regime, respectively. Note that these values of C_n^2 are the same as those used in Sec. 4.5. The simulation grid size is set to 256×256 pixels for weak and moderate turbulence, while it is set to 512×512 pixels for strong turbulence conditions.

All the simulations conducted use an initially collimated Gaussian beam with wavelength $\lambda = 785$ nm and a link distance $L = 1000$ m. The initial beam radius

at the transmitter is $W_0 = 5$ cm. To assess the impact of aperture averaging in such system three different receiving aperture sizes are tested, with diameters 25, 60 and 80 mm—this apertures sizes were also used in Chap. 3. In addition point receiver conditions are also tested, which is taken as a single pixel in the optical axis of the simulation grid.

The wave optics code used to perform the numerical simulations for partially coherent beams is based on the method described in the previous sections. In order to generate a GSM phase screen $\varphi(x, y)$ the convolution in Eq. (11) is performed using the Fourier transform convolution theorem, thus, to accurately approximate the convolution—accounting for the discretization limitations imposed by the finite simulation grid size—the expression in Eq. (11) is scaled as

$$\varphi(x, y) = [r(x, y) \otimes g(x, y)]\Delta x \Delta y, \tag{24}$$

where Δx and Δy are the spatial sample step sizes along the dimensions of the simulation grid, and $g(x, y)$ is a Gaussian filter given by Eq. (13). Next, to create the Gaussian-correlated random phase function in Eq. (24), the random matrix $r(x, y)$, following the probability density function in Eq. (12), is defined as

$$r(x, y) = \frac{[\gamma(x, y) - 0.5]\sqrt{12\sigma_r^2}}{\sqrt{\Delta x \Delta y}}, \tag{25}$$

where $\gamma(x, y)$ is a random number generator uniformly distributed on $[0, 1]$. The spatial coherence length l_c of the initial GSM beam can be related to the variance of the Gaussian filter σ_g^2 and the variance of the random matrix σ_r^2 using Eq. (20) as

$$l_c^2 = \frac{16\pi\sigma_g^4}{\sigma_r^2}. \tag{26}$$

The spatial coherence length is set to $l_c = 3$ cm as a common value used in a previous work [132]. To reduce the simulation runtime 30 random GSM phase screens are used to generate a partially coherent beam wave to be propagated through the turbulence random phase screens [135]. The number of turbulence screens are 6, 16 and 46 for weak, moderate and strong turbulence conditions, respectively; in order to only create sufficiently weak fluctuation in each propagation step and avoid aliasing issues.

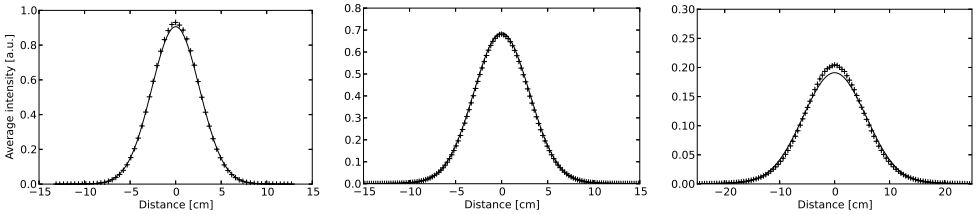

(a) Weak turbulence. (b) Moderate turbulence. (c) Strong turbulence.

Figure 5.2 Simulated average intensity profile (crosses) and analytic profile (solid line) for a GSM beam propagating in atmospheric turbulence.

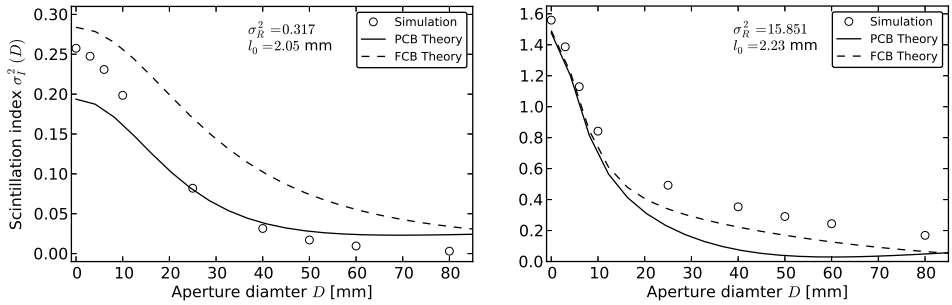

(a) (b)

Figure 5.3 Scintillation index predicted by simulation data (circles), and theory for a partially coherent beam (solid line) and a fully coherent beam (dashed line), in (a) weak and (b) strong turbulence regimes, as a function of the receiving aperture size.

The average intensity profile obtained from the wave optics code (crosses) and the estimated intensity profile (solid line), predicted by Eq. (9), is shown in Fig. 5.2. The simulated and theoretical intensity profiles for weak and moderate turbulence conditions are in good agreement; while for strong turbulence there is a slight deviation, possibly due to the relatively low number of GSM phase screens used to generate the partially coherent beam. Note that the intensity profiles shown correspond to the cross-section taken along the x-axis at the receiver plane in the optical axis.

Figure 5.3 shows a comparison between the scintillation index predicted by the GSM theory for a partially coherent beam and the SI obtained directly from the simulation data. Weak and strong turbulence conditions are presented in Figs. 5.3(a) and 5.3(b), respectively. The scintillation index for a fully coherent beam (FCB) is also shown, for comparison purposes. The expressions to calculate the SI for a PCB and a FCB are those given in Appendix C, where for the PCB case the dimensionless beam parameters Θ and Λ are replaced for the effective parameters defined in Eq. (10), in order to include the effects of a GSM beam. Moreover, the minimum effective scale size that produces scintillation in the simulations is not zero, but rather twice the grid spacing Δx of the respective scenario. Thus, the resulting inner scale of turbulence is $l_0 = 2.05$ mm in weak turbulence and $l_0 = 2.23$ mm for strong turbulence. The differences observed between the simulated data and the theoretical predictions can be due to the finite number of realizations of the GSM phase screens, that were restricted to 30 to avoid an excessively long simulation runtime. This discrepancies have been annotated before [138]. It can be seen in Fig. 5.3(a) how the use of a PCB in weak turbulence improves the SI statistics compared to a FCB, but this improvement vanishes as aperture averaging increases. Whereas for strong turbulence there is no relative advantage when using a PCB. This situation is expected as the effects of strong atmospheric turbulence disrupt the spatial coherence length of a FCB, within a short distance from the source, in such a way that the beam starts to behave like a PCB when the traveling beam is detected at the receiver plane. Moreover, it has been concluded elsewhere that for fixed link conditions a smaller coherence length l_c is necessary—in strong turbulence compared to weak turbulence—for a PCB to effectively reduce the scintillation index [138]. Note how the receiving aperture averaging effect increases,

consequently reducing the SI value, as the aperture diameter increases to finally settling to a plateau indicating that the SI can not be reduced without bounds, as any physical system has a saturation regime.

5.3.1 PDF data analysis and discussion

The study of fully coherent beams in terms of the probability density function has been performed in Chapter 3. Here, the analysis is extended to partially coherent beams based on the Gaussian Schell-model described above. Previously, Xiao and Voelz [132] conducted a work on the on-axis PDF of a PCB in atmospheric turbulence, i.e. only for point receivers, using the Lognormal (LN) and Gamma-Gamma (GG) distributions. The authors concluded that in weak turbulence regime the PDF data was best described by a GG distribution; while the LN model has a better fit in strong turbulence conditions. Nevertheless, they found that by manipulating the ratio between the initial beam size and the atmospheric coherence length W_0/ρ_0, and the PCB coherence length size l_c the PDF data fits with one of both models.

Here, the exponentiated Weibull (EW) model is tested to find if it is still valid for partially coherent beams propagating in atmospheric turbulence, as the validity of this model for fully coherent beams has been demonstrated in the preceding chapters. Additionally aperture averaging conditions are also included in the analysis. In addition to the EW model, the LN and the GG models are assessed to find their suitability to model the irradiance fluctuation for PCBs in atmospheric turbulence in the presence of aperture averaging. The GG and EW models are fitted to the PDF data, using the Levenberg-Marquardt least-squares fitting algorithm [103, 104]. To generate the PDF plots in the Lognormal model case, no fitting algorithm is used; and the LN parameter is estimated using the scintillation index data directly in combination with Eq. (3) in Chap. 3. In addition, the expressions presented in Sec. 3.4 are used to estimate the PDF data for every tested case, for the EW model. The same conventions to conduct the PDF study in Sec. 3.5 are adopted here. A total of 10000 realizations were run to reduce the statistical uncertainties in the numerical simulations of the

Table 1 Parameters for the LN, GG and EW distributions used to generate PDF curves in Figs. 5.4–5.6. The general conditions of the experiments, and the estimated scintillation index for the GG and EW distributions are also shown.

Aperture		Conditions			LN	Gamma-Gamma			Exponentiated Weibull			
D [mm]		$\sigma^2_{I\text{data}}$	σ^2_R	A	$\sigma^2_{\ln I}$	α_{fit}	β_{fit}	$\hat{\sigma}^2_{I\text{fit}}$	α	β	η	$\hat{\sigma}^2_I$
Weak→	0.0	0.265	0.317	1.000	0.235	9.66	6.63	0.270	4.89	1.03	0.46	0.266
	25.0	0.089	0.317	0.334	0.085	171.62	11.77	0.091	3.67	1.97	0.73	0.089
	60.0	0.011	0.317	0.041	0.011	143.02	143.02	0.014	1.69	8.27	1.00	0.011
	80.0	0.004	0.317	0.013	0.004	143.02	143.02	0.014	1.01	19.27	1.03	0.004
Moderate→	0.0	1.625	2.202	1.000	0.965	1.62	1.62	1.620	5.93	0.46	0.11	1.620
	25.0	0.438	2.202	0.270	0.363	9.28	2.84	0.498	5.37	0.80	0.33	0.439
	60.0	0.074	2.202	0.046	0.072	171.62	13.12	0.083	3.47	2.20	0.77	0.074
	80.0	0.030	2.202	0.018	0.029	171.62	40.07	0.031	2.52	4.06	0.92	0.030
Strong→	0.0	1.559	15.851	1.000	0.940	1.96	1.96	1.281	5.94	0.46	0.11	1.554
	25.0	0.512	15.851	0.235	0.413	6.82	2.78	0.559	5.50	0.74	0.29	0.513
	60.0	0.244	15.851	0.112	0.219	171.62	3.64	0.282	4.80	1.08	0.48	0.245
	80.0	0.168	15.851	0.077	0.155	5.20	171.62	0.199	4.39	1.34	0.58	0.168

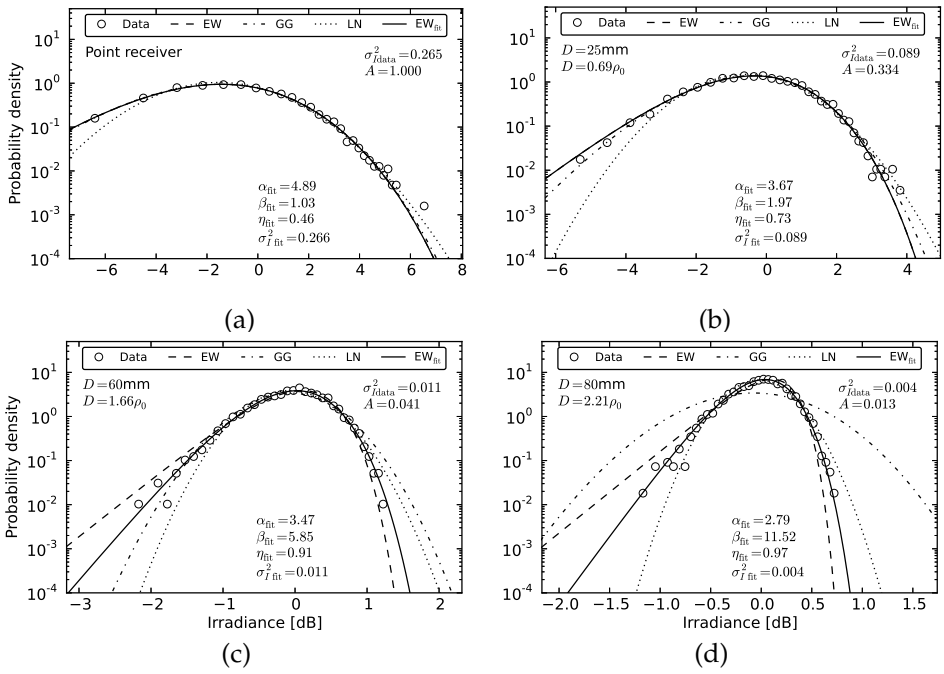

Figure 5.4 Simulation data (circles) for a GSM beam in weak turbulence regime ($\sigma_R^2 = 0.317$) with $l_c = 3$ cm for different receiving apertures. The best fit curve for the EW distribution (solid line) is shown along with its parameters values.

irradiance. Unequal bins were used whenever needed.

The simulation scenario included weak ($\sigma_R^2 = 0.317$), moderate ($\sigma_R^2 = 2.202$) and strong ($\sigma_R^2 = 15.851$) turbulence conditions. All the parameters needed to reproduce the plots for each PDF model shown in Figs. 5.4–5.6 are presented in Table 1. The $\sigma^2_{I\text{data}}$ value—i.e. the scintillation index obtained directly from the simulation data—is used to estimate the parameters of the LN (dotted line) and EW (dashed line) models. For the GG model (dash-dotted line) the parameter values are obtained from the fitting algorithm. The best fit curve for the exponentiated Weibull distribution (solid line) is also plotted, and its estimated parameters values are embedded in each figure. Furthermore, in Table 1 some optical link defining parameters are also listed, such as the receiving aperture size D, scintillation index σ_I^2, Rytov variance σ_R^2, and the aperture averaging factor A obtained by the ratio of the SI of the corresponding aperture to that of the point receiver. This approach is used as the expression in Eq. (31) in Chapter 3, for the aperture averaging factor, only depends on the receiving aperture size and it does not account for the additional transmitter aperture averaging effect due to the use of a PCB, thus it is no longer valid for GSM beam waves.

Figure 5.4 presents the PDF analysis for a partially coherent Gaussian beam in weak turbulence conditions. Data has been obtained for a point receiver Fig. 5.4(a) and three other aperture diameters Fig. 5.4(b)–(d). The first thing to be noticed is that the EW parameter values obtained with the fitting algorithm are exactly the same as

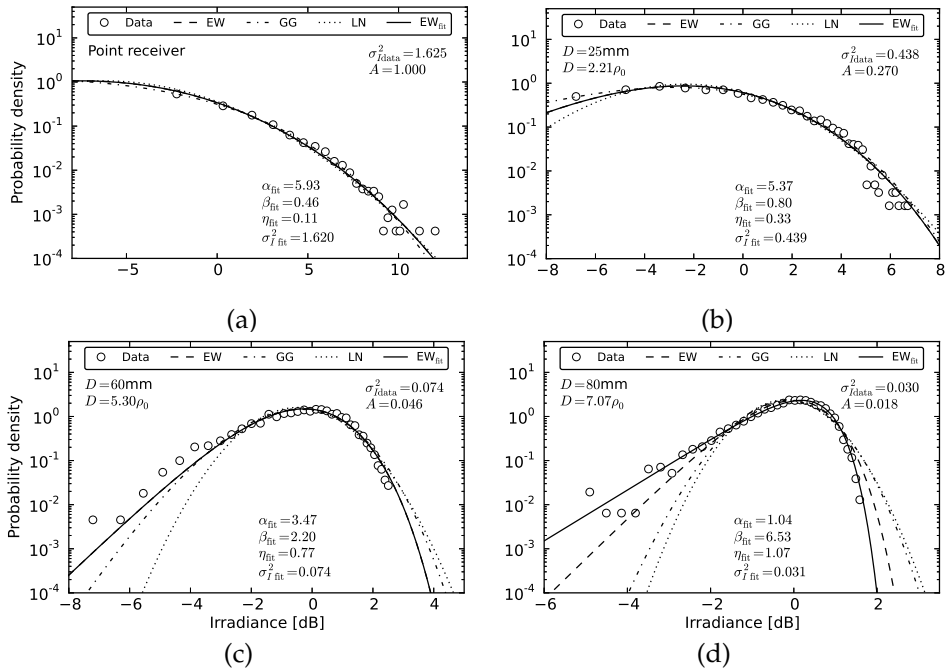

Figure 5.5 Simulation data (circles) for GSM beam in moderate turbulence regime ($\sigma_R^2 = 2.202$) with $l_c = 3$ cm for different receiving apertures. The best fit curve for the EW distribution (solid line) is shown along with its parameters values.

those predicted by the expressions derived in Sec. 3.4—see Table 1—, for Fig. 5.4(a) and (b). Note that in these cases the GG model offers an excellent fit to the PDF data. Secondly, the best fit algorithm for the GG distribution for the largest aperture tested fails to converge as the model parameters are relatively large and produce overflow errors in the GG PDF, for Fig. 5.4(d). The LN model is a good fit in all cases, except in Figs. 5.4(c) and (d) where the tail prediction fails in large amount. Nevertheless, the tails behavior of the simulation PDF data is not properly modeled by a Lognormal distribution. It is noteworthy that EW distribution (dash line) offers a best prediction than the LN model for all shown cases; improves the estimation of the GG model for the right tail, and even offers an acceptable fit to the PDF data when the GG fails for the largest aperture.

The analysis for moderate turbulence conditions is shown in Fig. 5.5, where the same apertures as in Fig. 5.4 are tested. Again, the EW parameter values from the fitting algorithm are the same as those in Table 1 for Figs. 5.5(a)–(c). Here, the EW distribution is always the best fit, while the GG curve practically offers the same fit as the EW model for the point receiver and for $D = 25$ mm, although it has a poorer performance in Fig. 5.5(c). Whereas the LN model appears as a valid fit for Fig. 5.5(a) and (b), it fails for the other two receiving aperture diameters tested. For the largest aperture shown in Fig. 5.5(d) the EW model (dashed line) gives a better fit than the LN and GG distribution, although it is not a perfect fit to the PDF data. Nevertheless,

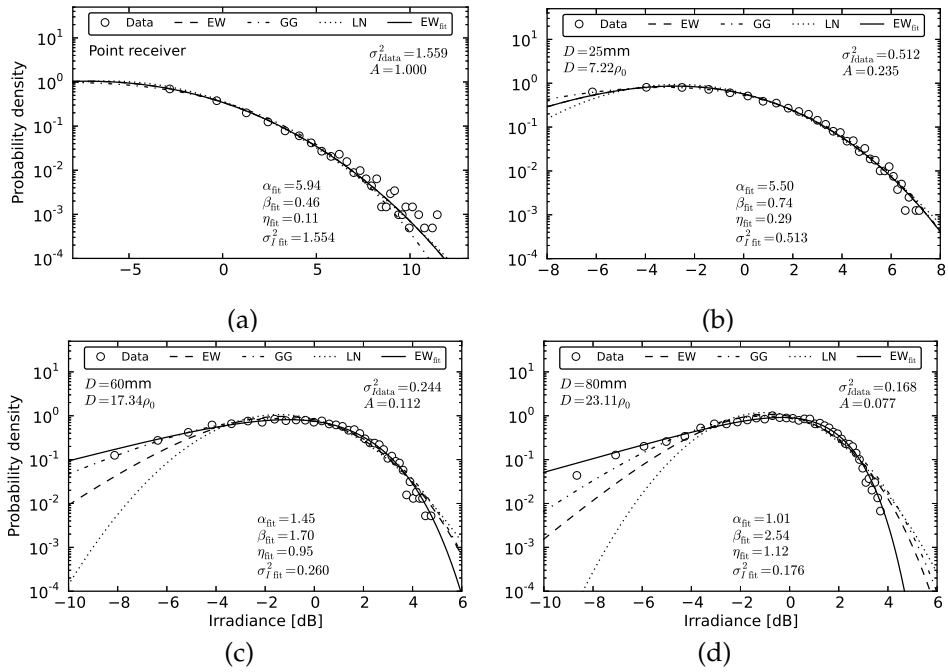

Figure 5.6 Simulation data (circles) for GSM beam in strong turbulence regime ($\sigma_R^2 = 15.851$) with $l_c = 3$ cm for different receiving apertures. The best fit curve for the EW distribution (solid line) is shown along with its parameters values.

the fitted EW curve (solid line) offers the best prediction to actual data.

Finally, the simulation PDF results for the strong turbulence regime conditions are shown in Fig. 5.6. Once more, the EW parameter values from the fitting algorithm are the same as those in Table 1 for Fig. 5.6(a) and (b). For the point receiver case all the three models tested can be said to offer the same fit to the PDF data. For the smallest aperture $D = 25$ mm the EW and GG distributions are excellent fits, whereas the LN model is a good fit with a slight deviation in the left tail from the simulation data. The LN model estimation fails for the rest of the apertures. In Fig. 5.6(c) and (d) the fitted EW model (solid line) offers the best prediction to PDF data. For these cases the EW model (dashed line) offers the same prediction for the right tail as the GG distribution; while the EW is outperformed by the GG model for the left tail fit.

5.4 Summary

In this chapter a recently developed approach to simulate partially coherent beams, based on the Gaussian Schell-model theory, has been applied to study the suitability of the exponentiated Weibull distribution to model the irradiance fluctuations under atmospheric turbulence. For completeness of the study the Lognormal and the Gamma-Gamma models have also been included in the analysis, allowing for a direct

comparison to the EW distribution.

In a previous work [132] it was concluded that in weak turbulence regime the PDF data was best described by a GG distribution; while the LN model has a better fit in strong turbulence conditions. Whereas the analysis conducted above suggests that the EW distribution has an excellent fit to the PDF of the irradiance data for partially coherent beam waves propagating in weak-to-strong atmospheric turbulence regime in the presence of aperture averaging.

The exponentiated Weibull model, using the parameter values estimated from the expressions derived in Sec. 3.4, in most of the cases tested offered a good fit; while for some cases it provided the best fit to simulation PDF data. Nevertheless, in the cases where the EW model (dashed line) was not the perfect fit, the EW fitted version (solid line) was always the best fit to actual PDF data. Thus, the exponentiated Weibull proves to still be valid for partially coherent beams propagating in atmospheric turbulence in the presence of aperture averaging.

6

Conclusions & Future Work

THIS CHAPTER summarizes the main conclusions of the work developed during this Ph.D. Thesis. A general conclusion, along with the shortcomings of the proposed exponentiated Weibull model, and the future research lines are presented.

6.1 Conclusions

Since the Gamma-Gamma (GG) model was introduced by Al-Habash et al. [12] a decade ago, along with the Lognormal (LN) model, they have become ubiquitous in the free-space optical (FSO) communications literature in the studies on the probability density function (PDF) of the irradiance fluctuations in atmospheric turbulence. After a great number of works published on the subject, it has become customary to use as a decision criterion the ratio between the receiving aperture diameter D and the atmospheric coherence length ρ_0, to determine whether the LN or the GG distribution is adequate to model PDF data. Basically, it is accepted that if $D \ll \rho_0$ the receiving aperture is unable to average atmospheric effects and under this condition the Gamma-Gamma distribution presents the best fit to PDF of the received irradiance data. On the contrary, if $D \gg \rho_0$ a fair amount of aperture averaging takes place and the PDF of the data is better described by a Lognormal distribution. While, in the region of $D \sim \rho_0$ there is not a definitive answer and the best distribution to model the irradiance PDF can be either the LN or the GG distribution.

Although the Lognormal model has long been accepted to model data in weak turbulence, and when a relatively large amount of aperture averaging takes place, recently it has been suggested that the PDF of the irradiance fluctuations in weak turbulence is not truly Lognormal, as the second-order phase perturbation term in the Rytov approximation is needed to accurately represent the PDF data [92], resulting in a skewed LN distribution. Experimental results [57] and simulation data [57, 93] seem to support this claim.

The major drawback of the most widespread PDF models nowadays, i.e. LN and GG distribution, is that either of them is capable of fitting the irradiance data under all conditions of atmospheric turbulence in the presence of aperture averaging [14]. Moreover, there are several cases where neither the LN or the GG model seem to fit the irradiance data, specially in the left tail of the PDF [14, 58, 60, 106].

The work presented here was devoted to introduce and assess the suitability of a new model for the probability density function of the irradiance data in atmospheric turbulence, namely the exponentiated Weibull (EW) distribution, with simple closed-form expression for its PDF and cumulative distribution function (CDF). The proposed model has been derived using standard physical assumptions similar to those used for the Gamma model, with the addition of a nonlinearity manifested in terms of a power parameter as in the work by Yacoub [96]. Thus, a physical justification for the appearance of the exponentiated Weibull distribution in FSO links has been provided.

Previously, the Lognormal-Rician distribution—also called Beckmann PDF—, a very promising PDF model, was discarded as it was not possible to find expressions to deduce the distribution parameters directly from observable atmospheric parameters [12]. Knowing that for any new PDF model to be accepted and actually be used by the FSO community it must has tractable expressions to estimate the distribution parameters, Sec. 3.4 deals with this issue for the exponentiated Weibull model. There, a semi-heuristic approach was used to find a set of equations relating the EW parameters directly to the scintillation index (SI). This first approximation to the EW parameters has been tested in the weak-to-strong turbulence regime offering a fairly good fitting of the PDF of irradiance, with data from a wave optics code simulations

and experiments. In addition, previously published data from other authors, including numerical simulation results and experimental data in the moderate-to-strong turbulence regime, have been used to assess the EW model [14, 94]. Furthermore, for all the scenarios tested a best fit version of the EW distribution is obtained and always presents an excellent fit to the PDF data. The best fit version of the models analyzed is obtained by means of the Levenberg-Marquardt least-square fitting algorithm [103, 104].

The expressions derived for the EW distribution parameters have not been tested in the saturation regime, i.e. the scintillation index approaches unity for a point receiver. Nevertheless, if one is certain that the saturation will occur then the simple Weibull model, developed in Sec. 3.3.1, can be used as it degenerates to the negative exponential (NE) distribution, i.e. $f(I) \sim \exp(-I)$, complying with theory as it is well known that the PDF of irradiance becomes the NE distribution in the limit of saturated scintillation [11, 140]. For the exponentiated Weibull distribution to become a negative exponential distribution the shape parameters α and β shall be unity. This is clearly not the case for current expressions of the EW parameters, suggesting the need for a better approximation to make the distribution parameter expressions valid in all regimes of atmospheric turbulence and additional work should be done in this regard. Perhaps, the EW parameters expressions should not only depend on the SI—as the current expressions—, but in some other link parameters. It is the author's belief that the shape parameter α for the EW distribution is somehow affected by the ratio D/ρ_0, as previously suggested [80], and/or the Rytov variance σ_R^2.

The results presented here suggest that the EW distribution exhibits the better fit for data under different aperture averaging conditions. Moreover, expressions to derive the EW distribution parameters have been found. For these reasons the exponentiated Weibull distribution becomes an excellent candidate to model the PDF of irradiance data under all conditions of atmospheric turbulence in the presence of aperture averaging.

In Chapter 4 the analysis of the probability of fade and bit error-rate (BER) performance of a FSO communication link, when the atmospheric turbulence can be modeled by an exponentiated Weibull distribution, is presented. For this analysis the new model was also compared with the Lognormal and Gamma-Gamma distributions, using simulation and experimental data results. It was seen that whenever a model has a close fit to the PDF of the irradiance data, then the probability of fade and the bit-error rate have a close fit too, accordingly. Thus, the EW distribution offered the best fits to actual data for the probability of fade and BER performance, when compared with the LN and GG models.

For the BER performance study a free-space optical communication links based on an intensity-modulation/direct-detection (IM/DD) system, using on-off keying (OOK) modulation, has been used. New closed-form average BER expressions have been derived for the Gamma-Gamma and exponentiated Weibull fading channel models by making use of the Meijer's G-function [See Appendix B.4]. It was not possible to obtain such expression for Lognormal turbulence due to the complex mathematical of its PDF expression. It is noteworthy to mention that Yi et al. [119] have proposed an approximation of the average BER expression by means of the generalized GaussLaguerre quadrature rule, for an IM/DD FSO system with OOK modulation using the exponentiated Weibull fading channel model. This is an evidence that the

EW is starting to be considered by other authors in the FSO community as a valid model for the irradiance fluctuations in atmospheric turbulence.

Using the seminal work of Farid and Hranilovic [109] the BER expression is extended to include the impact of pointing errors under exponentiated Weibull turbulence. The misalignment fading model results of considering independent identical Gaussian distributions for the elevation and horizontal displacement (sway), changing the statistics of the probability density function of the received irradiance data. Therefore, a new PDF and CDF have been derived when the atmospheric turbulence and pointing errors are modeled by an EW distribution and the misalignment model in [109], respectively. In terms of the bit error-rate a new closed-form expression has been derived, again utilizing the Meijer's G-function. To assess this new expression Monte Carlo simulations have been conducted, where the overall channel state was obtained by using the inverse CDF method to draw random values from the atmospheric turbulence and misalignment fading models, and then multiplying them, since both are assumed to be independent processes. The spherical wave approximation is used to estimate the scintillation index, which then is used to obtain the EW distribution parameter. The whole analysis was done in terms of the aperture averaging, as three different receiving aperture diameters were used and no point receiver has been analyzed. From the BER analysis conducted, it was concluded that the influence of the aperture averaging has a larger impact in the presence of pointing errors, relative to that of turbulence only conditions. Note that other authors have utilized the model proposed by Farid and Hranilovic [109] with the atmospheric turbulence modeled by different distributions [111, 120–122].

Lastly, the proposed exponentiated Weibull fading channel model has been assessed, in Chapter 5, with partially coherent beams (PCB) using the Gaussian Schell-model (GSM) theory. The use of a PCB in FSO links has been suggested as an atmospheric turbulence mitigation technique, called transmitter aperture averaging. The simulation approach recently developed by Xiao and Voelz [137] was used in a wave optics code to generate a PCB propagating in atmospheric turbulence, and the PDF statistics were obtained from the simulated irradiance data. The first work on the probability density function of the irradiance data of partially coherent beams based on the GSM theory was conducted by Xiao and Voelz [132], and only included the LN and GG distributions for point receivers. Here, the study on the PDF included the new proposed EW model in the presence of aperture averaging, in the weak-to-strong turbulence regime. Point receiver conditions were also analyzed. For completeness of the study the Lognormal and the Gamma-Gamma models have also been included in the analysis, allowing for a direct comparison to the EW distribution. On the one hand, the exponentiated Weibull model, estimated from the expressions derived in Sec. 3.4, in most of the tested cases offered a good fit; while for some cases it provided the best fit to simulation PDF data. On the other hand, the EW fitted version—obtained from a least-squares curve fitting algorithm—was always the best fit to the actual PDF data. Thus, the exponentiated Weibull fading channel model proves to still be valid for partially coherent beams.

In summary, a new proposal to model the irradiance fluctuations, in FSO links, under atmospheric turbulence in the presence of aperture averaging has been made, resulting in the exponentiated Weibull distribution. The work conducted here suggests that the EW model is a valid model in the weak-to-strong turbulence regime.

The new model has been compared to the two currently most widespread fading models, based on the Lognormal and Gamma-Gamma distributions, proving to cope with the predictions made by those and, in some cases, even outperforming the LN and GG models. From the communication theory point of view, the EW model has been analyzed in terms of the probability of fade and bit-error rate, and a new-closed form expression has been derived for estimating the BER performance for IM/DD systems, using OOK modulation. Furthermore, this expression for the EW model has been extended to include pointing errors. Finally, the exponentiated Weibull distribution has been proved to be valid with partially coherent beams, using the GSM theory. In the following section, the lines of work that the author has envisioned as the next steps in the development of the exponentiated Weibull fading channel model, to enlarge its theoretical ground, are given.

A special acknowledgement to the scientific open-source community is given, as the vast majority of the work presented in this book has been accomplished by using free and open-source alternatives to commercial packages. Among the libraries used here there is the Scientific Python (SciPy) package for mathematics, science, and engineering written by Jones et al. [141]; the pure-Python library for multiprecision floating-point arithmetic `mpmath` written by Johansson [117]; and the python 2D plotting library `matplotlib` written by Hunter [142].

6.2 Future Work

In future lines of work, in order to provide an even more solid ground to the exponentiated Weibull fading channel model proposed in this book, it is expected to obtain an improved set of expressions to estimate the distribution parameters, to be applicable in any conditions of aperture averaging and turbulence regime, including the saturated scintillation region; as current expressions—derived in Sec. 3.4—were obtained following a semi-heuristic approach. Moreover, to complete the development of the EW distribution as a solid candidate to model irradiance fluctuations in FSO links, it is desirable to obtain a mathematical expression for the joint PDF of the irradiance and its time derivative, in order to account for expected number of fades per unit time and their mean fade time. This problem, eminently mathematical, is of great complexity in its derivation and unfortunately it couldn't be solved during the time frame of this thesis. Once this two major shortcomings are solved, the exponentiated Weibull fading channel model would possess a solid physical and mathematical ground to be considered within the FSO community as a valid and practical-to-use distribution to model the irradiance fluctuations under atmospheric turbulence.

Appendix A

Publications

Book Chapter

1. R. Barrios and F. Dios, "Wireless Optical Communications Through the Turbulent Atmosphere: A review," in *Optical Communications Systems*, Narottam Das, Ed., InTech, pp. 3–40, 2012.

Journals & Proceedings

1. R. Barrios and F. Dios, "BER performance of FSO links under exponentiated Weibull turbulence with pointing errors," *submitted.*

2. R. Barrios and F. Dios, "Exponentiated Weibull fading model for free-space optical links with partially coherent beams under aperture averaging," *Opt. Eng.* manuscriptID: OE-1320280 (to be published), 2013.

3. R. Barrios and F. Dios, "Exponentiated Weibull model for the irradiance probability density function of a laser beam propagating through atmospheric turbulence," *Opt. Laser Technol.*, vol. 41, no. 1, pp. 13–20, 2013.

4. R. Barrios, "Contributions to Free-Space Optical Communications through the Turbulent Atmosphere," in *2012 Barcelona Forum on Ph.D. Research in Communications,* X. Masip, X. Aragonès, J. Forné, J. L. Balczar, A. Rodríguez-Gómez, Ed., pp. 81–82, 2012.

5. R. Barrios and F. Dios, "Probability of fade and BER performance of FSO links over the exponentiated Weibull fading channel under aperture averaging," in *Advanced Free-Space Optical Communication Techniques and Applications,* L. Laycock and H. J. White, Ed., *Proc. SPIE,* vol. 8540, pp. 85400D, 2012.

6. R. Barrios and F. Dios, "Reply to comments on: "The exponentiated Weibull distribution family under aperture averaging for Gaussian beam waves"," *Opt. Express,* vol. 20, no. 18, pp. 20684–20687, 2012.

7. R. Barrios and F. Dios, "The exponentiated Weibull distribution family under aperture averaging for Gaussian beam waves," *Opt. Express,* vol. 20, no. 11, pp. 13055–13064, 2012.

8. R. Barrios, F. Dios, J. Recolons, A. Rodriguez, "Aperture averaging in a laser Gaussian beam: simulations and experiments," in *Free-Space Laser Communications X,* C. Majumdar, A. K. and Davis, Ed., *Proc. SPIE,* vol. 7814, pp. 78140C, 2010.

Appendix B

Special Functions

B.1 Gamma Function

The Gamma function is an interpolation between integer numbers in the factorial function. The most common way to define the Gamma function is through the integral representation

1. $\Gamma(z) = \int_0^\infty e^{-t} t^{z-1} dt, \quad \mathrm{Re}(z) > 0.$ [143, Eq. (8.310.1)]

If the argument is an integer then the Gamma function reduces to a simple factorial

2. $\Gamma(z) = (z-1)!.$ [144, Eq. (2.4)]

The Gamma function can be generalized by the lower and upper incomplete gamma function, respectively defined

3. $\gamma(a, z) = \int_0^a e^{-t} t^{z-1} dt,$ [143, Eq. (8.350.1)]

4. $\Gamma(a, z) = \int_a^\infty e^{-t} t^{z-1} dt.$ [143, Eq. (8.350.2)]

B.2 Macdonald Function

The modified Bessel function $K_\nu(z)$ is one of the two linearly independent solutions to the modified Bessel's equation

$$z^2 \frac{d^2 y}{dz^2} + z \frac{dy}{dz} + (z^2 + \nu^2) y = 0.$$

The modified Bessel functions of the second kind are sometimes called the Macdonald functions [144, Eq. (6.106)] or Basset functions. They are exponential decaying functions, with integral representation

1. $K_\nu(z) = \frac{1}{2} \left(\frac{z}{2}\right)^\nu \int_0^\infty t^{-(\nu+1)} \exp\left(-t - \frac{z^2}{4t}\right) dt.$ [143, Eq. (8.432.6)]

B.3 Hypergeometric Function

A generalized hypergeometric function is defined in terms of hypergeometric series as

1. $${}_pF_q\left(a_1,\ldots,a_p;\, b_1,\ldots,b_q;\, z\right) = \sum_{n=0}^{\infty} \frac{(a_1)_n \ldots (a_p)_n}{(b_1)_n \ldots (b_p)_n} \frac{z^n}{n!},$$

where $(a)_n$ is the Pochhammers symbol, and it is defined by

$$(a)_n = a(a+1)\cdots(a+n-1) = \frac{\Gamma(a+n)}{\Gamma(a)}, \quad (a)_0 = 1.$$

A hypergeometric function complies with the following convergence properties [144, Sec. 10.2]

- $p < q+1$, the series converges for all (finite) x.
- $p = q+1$, the series converges for $|x| < 1$ and diverges for $|x| > 1$.
- $p > q+1$, the series diverges for all x except $x = 0$.

B.4 Meijer's G-Function

The Meijer's G-function is a very general function, first introduced as an analytic continuation of the generalized hypergeometric function for the divergent cases. The Meijer's G-function is defined as a line integral in the complex plane

1. $$G_{p,q}^{m,n}\left[z \,\middle|\, \begin{matrix}\mathbf{a_p} \\ \mathbf{b_q}\end{matrix}\right] = \frac{1}{2\pi i}\int_L \frac{\prod_{j=1}^{m}\Gamma(b_j - s)\prod_{j=1}^{n}\Gamma(1-a_j+s)}{\prod_{j=1}^{q}\Gamma(1-b_j+s)\prod_{j=n+1}^{p}\Gamma(a_j-s)} z^s ds,$$

where $\mathbf{a_p} = a_1,\ldots,a_p$ and $\mathbf{b_q} = b_1,\ldots,b_q$; and L denotes the path to be followed in the integration [143, Sec. 9.302].

The Meijer's G-function includes most of the special functions used in mathematics as particular cases.

B.4.1 Useful expressions

1. $b^* = s + t - \dfrac{u+v}{2}$ [145, Eq. (07.34.21.0015.01)]
2. $c^* = m + n - \dfrac{p+q}{2}$ [145, Eq. (07.34.21.0016.01)]
3. $\rho = \sum_{j=1}^{v} d_j - \sum_{j=1}^{u} c_j + \dfrac{u-v}{2} + 1$ [145, Eq. (07.34.21.0017.01)]
4. $\mu = \sum_{j=1}^{q} b_j - \sum_{j=1}^{p} a_j + \dfrac{p-q}{2} + 1$ [145, Eq. (07.34.21.0018.01)]
5. $\Delta(k,a) = \dfrac{a}{k}, \dfrac{a+1}{k}, \cdots, \dfrac{a+k-1}{k}$ [146, Eq. (22)]

B.4.2 Relation to other functions

1. $\exp(z) = G_{0,1}^{1,0}\left[z \,\middle|\, \begin{matrix} - \\ 0 \end{matrix}\right]$ [147, Eq. (8.4.3.1)]

2. $\Gamma(a,z) = G_{1,2}^{2,0}\left[z \,\middle|\, \begin{matrix} 1 \\ 0, a \end{matrix}\right]$ [145, Eq. (06.06.26.0005.01)]

3. $\operatorname{erfc}(z) = \frac{1}{\sqrt{\pi}} G_{1,2}^{2,0}\left[z^2 \,\middle|\, \begin{matrix} 1 \\ 0, \frac{1}{2} \end{matrix}\right]$ [147, Eq. (8.4.14.2)]

4. $K_\nu(z) = \frac{1}{2} G_{0,2}^{2,0}\left[\frac{1}{4}z^2 \,\middle|\, \begin{matrix} - \\ \frac{1}{2}\nu, -\frac{1}{2}\nu \end{matrix}\right]$ [147, Eq. (8.4.23.1)]

5. ${}_pF_q\left(\mathbf{a_p}; \mathbf{b_q}; z\right) = \frac{\prod_{j=1}^{m}\Gamma(b_j)}{\prod_{j=1}^{m}\Gamma(a_j)} G_{p,q+1}^{1,p}\left[-z \,\middle|\, \begin{matrix} 1-\mathbf{a_p} \\ 0, 1-\mathbf{b_q} \end{matrix}\right]$ [143, Eq. (9.34.8)]

B.4.3 Definite integrals

1. $\int_0^y x^{\alpha-1} G_{p,q}^{m,n}\left[\omega x \,\middle|\, \begin{matrix} \mathbf{a_p} \\ \mathbf{b_q} \end{matrix}\right] dx = y^\alpha G_{p+1,q+1}^{m,n+1}\left[\omega y \,\middle|\, \begin{matrix} \mathbf{a_n}, 1-\alpha, \mathbf{a_{n:p}} \\ \mathbf{b_m}, -\alpha, \mathbf{b_{m:q}} \end{matrix}\right]$ [146, Eq. (26)]

2. $$\int_0^\infty x^{\alpha-1} G_{u,v}^{s,t}\left[\sigma x \,\middle|\, \begin{matrix} \mathbf{c_u} \\ \mathbf{d_v} \end{matrix}\right] G_{p,q}^{m,n}\left[\omega x^{\ell/k} \,\middle|\, \begin{matrix} \mathbf{a_p} \\ \mathbf{b_q} \end{matrix}\right] dx = \frac{k^\mu \ell^{\rho+\alpha(v-u)-1}\sigma^{-\alpha}}{(2\pi)^{b^*(\ell-1)+c^*(k-1)}}$$
$$\times G_{k\rho+\ell v, kq+\ell u}^{km+\ell t, kn+\ell s}\left[\frac{\omega^k k^{k(p-q)}}{\sigma^\ell \ell^{\ell(u-v)}} \,\middle|\, \begin{matrix} \Delta(k,\mathbf{a_n}), \Delta(\ell, 1-\alpha-\mathbf{d_v}), \Delta(k, \mathbf{a_{n+1:p}}) \\ \Delta(k,\mathbf{b_m}), \Delta(\ell, 1-\alpha-\mathbf{c_u}), \Delta(k, \mathbf{b_{m+1:q}}) \end{matrix}\right],$$

[147, Eq. (2.24.1.1)]

where

- $s, t, u, v, m, n, p, q, \ell$ and k are integer numbers.
- $\mathbf{a_{n:p}} = a_n, a_{n+1}, \ldots, a_p; \quad \forall\, n \le p, \quad \mathbf{a_p} \triangleq \mathbf{a_{1:p}}$.

Appendix C

Scintillation index for nonzero scales of turbulence

C.1 Useful dimensionless quantities

Hereafter, for mathematical convenience, the following dimensionless quantities are defined

$$\Theta_0 = 1 - \frac{L}{F_0}, \quad \Lambda_0 = \frac{2L}{kW_0^2},$$
$$\Theta = \frac{\Theta_0}{\Theta_0^2 + \Lambda_0^2}, \quad \Lambda = \frac{\Lambda_0}{\Theta_0^2 + \Lambda_0^2},$$

where $k = 2\pi/\lambda$ is the wavenumber, being λ the optical wavelength; L in the link distance, and W_0 and F_0 are the beam radius and phase front radius at the transmitter plane, respectively.

Additional quantities are defined as

$$Q_l = \frac{10.89L}{kl_0^2},$$
$$Q_0 = \frac{64\pi^2 L}{kL_0^2},$$
$$\varphi_1 = \tan^{-1}\left(\frac{2\Lambda}{1+2\Theta}\right),$$
$$\varphi_2 = \tan^{-1}\left[\frac{(1+2\Theta)Q_l}{3+2\Lambda Q_l}\right],$$
$$\overline{\Theta} = 1 - \Theta.$$

C.2 Point receiver case

In order to account for the effects induced by the inner l_0 and outer scale L_0 of turbulence, the scintillation index for a point receiver is given by

$$\sigma_I^2(l_0, L_0) = \exp\left[\sigma^2_{\ln X}(l_0) - \sigma^2_{\ln X}(L_0) + \sigma^2_{\ln Y}(l_0)\right] - 1. \tag{C.1}$$

The first term in the exponential of Eq. (C.1) is the large-scale log-irradiance scintillation due to the inner scale of turbulence, defined by

$$\sigma^2_{\ln X}(l_0) = 0.49\sigma_R^2 \left(\frac{1}{3} - \frac{1}{2}\overline{\Theta} + \frac{1}{5}\overline{\Theta}^2\right) \left(\frac{\eta_X Q_l}{\eta_X + Q_l}\right)^{7/6} \times \left[1 + 1.75\left(\frac{\eta_X}{\eta_X + Q_l}\right)^{1/2} - 0.25\left(\frac{\eta_X}{\eta_X + Q_l}\right)^{7/12}\right], \tag{C.2}$$

where $\sigma_R^2 = 1.23 C_n^2 k^{7/6} L^{11/6}$ is the Rytov variance, and

$$\eta_X = \left[\frac{0.38}{1 - 3.21\overline{\Theta} + 5.29\overline{\Theta}^2} + 0.47\sigma_R^2 Q_l^{1/6} \left(\frac{\frac{1}{3} - \frac{1}{2}\overline{\Theta} + \frac{1}{5}\overline{\Theta}^2}{1 + 2.20\overline{\Theta}}\right)^{6/7}\right]^{-1}. \tag{C.3}$$

Next, the large-scale log-irradiance scintillation induced by the outer scale of turbulence is given by

$$\sigma^2_{\ln X}(L_0) = 0.49\sigma_R^2 \left(\frac{1}{3} - \frac{1}{2}\overline{\Theta} + \frac{1}{5}\overline{\Theta}^2\right) \left(\frac{\eta_{X0} Q_l}{\eta_{X0} + Q_l}\right)^{7/6} \times \left[1 + 1.75\left(\frac{\eta_{X0}}{\eta_{X0} + Q_l}\right)^{1/2} - 0.25\left(\frac{\eta_{X0}}{\eta_{X0} + Q_l}\right)^{7/12}\right], \tag{C.4}$$

where

$$\eta_{X0} = \frac{\eta_X Q_0}{\eta_X + Q_0}. \tag{C.5}$$

Finally, the small-scale log-irradiance scintillation—note that the effects of L_0 are negligible—is given by

$$\sigma^2_{\ln Y}(l_0) = \frac{0.51\sigma_G^2}{\left(1 + 0.69\sigma_G^{12/5}\right)^{5/6}}, \tag{C.6}$$

where

$$\sigma_G^2 = 3.86\sigma_R^2 \left\{0.40\frac{\left[(1+2\Theta)^2 + (2\Lambda + 3/Q_l)^2\right]^{11/12}}{\left[(1+2\Theta)^2 + 4\Lambda^2\right]^{1/2}} \left[\sin\left(\frac{11}{6}\varphi_2 + \varphi_1\right) + \frac{2.61}{\xi^{1/4}}\sin\left(\frac{4}{3}\varphi_2 + \varphi_1\right) - \frac{0.52}{\xi^{7/24}}\sin\left(\frac{5}{4}\varphi_2 + \varphi_1\right)\right] - \frac{13.40\Lambda}{Q_l^{11/6}\left[(1+2\Theta)^2 + 4\Lambda^2\right]} - \frac{11}{6}\left[\left(\frac{1 + 0.31\Lambda Q_l}{Q_l}\right)^{5/6} + \frac{1.10(1 + 0.27\Lambda Q_l)^{1/3}}{Q_l^{5/6}} - \frac{0.19(1 + 0.24\Lambda Q_l)^{1/4}}{Q_l^{5/6}}\right]\right\}, \tag{C.7}$$

where

$$\xi = (1 + 2\Theta)^2 Q_l^2 + (3 + 2\Lambda Q_l)^2. \tag{C.8}$$

C.3 Finite aperture receiver case

For a finite aperture D receiver, including the effects induced by the inner l_0 and outer scale L_0 of turbulence, the expression of the scintillation index is given by

$$\sigma_I^2(D, l_0, L_0) = \exp\left[\sigma_{\ln X}^2(D, l_0) - \sigma_{\ln X}^2(D, L_0) + \sigma_{\ln Y}^2(D, l_0)\right] - 1, \quad \Omega_G \geq \Lambda, \tag{C.9}$$

where $\Omega_G = 2L/kW_G$ is a non-dimensional parameter defining the beam radius at the collecting aperture element; being W_G the soft aperture radius, related to the receiving aperture D by $D^2 = 8W_G^2$.

The first term in the exponential of Eq. (C.9) is the large-scale log-irradiance scintillation due to the inner scale of turbulence, defined by

$$\sigma_{\ln X}^2(D, l_0) = 0.49\sigma_R^2 \left(\frac{\Omega_G - \Lambda}{\Omega_G + \Lambda}\right)^2 \left(\frac{1}{3} - \frac{1}{2}\overline{\Theta} + \frac{1}{5}\overline{\Theta}^2\right) \left(\frac{\eta_{Xd} Q_l}{\eta_{Xd} + Q_l}\right)^{7/6} \times \left[1 + 1.75\left(\frac{\eta_{Xd}}{\eta_{Xd} + Q_l}\right)^{1/2} - 0.25\left(\frac{\eta_{Xd}}{\eta_{Xd} + Q_l}\right)^{7/12}\right], \tag{C.10}$$

where

$$\eta_{Xd} = \frac{\eta_X}{1 - 0.40\eta_X(2 - \overline{\Theta})/(\Lambda + \Omega_G)}. \tag{C.11}$$

Next, the large-scale log-irradiance scintillation induced by the outer scale of turbulence is given by

$$\sigma_{\ln X}^2(D, L_0) = 0.49\sigma_R^2 \left(\frac{\Omega_G - \Lambda}{\Omega_G + \Lambda}\right)^2 \left(\frac{1}{3} - \frac{1}{2}\overline{\Theta} + \frac{1}{5}\overline{\Theta}^2\right) \left(\frac{\eta_{Xd0} Q_l}{\eta_{Xd0} + Q_l}\right)^{7/6} \times \left[1 + 1.75\left(\frac{\eta_{Xd0}}{\eta_{Xd0} + Q_l}\right)^{1/2} - 0.25\left(\frac{\eta_{Xd0}}{\eta_{Xd0} + Q_l}\right)^{7/12}\right], \tag{C.12}$$

where

$$\eta_{Xd0} = \frac{\eta_{Xd} Q_0}{\eta_{Xd} + Q_0}. \tag{C.13}$$

Finally, the small-scale log-irradiance scintillation is given by

$$\sigma_{\ln Y}^2(D, l_0) = \frac{1.27\sigma_R^2 \eta_Y^{-5/6}}{1 + 0.40\eta_Y/(\Lambda + \Omega_G)}, \tag{C.14}$$

where

$$\eta_Y = 3\left(\frac{\sigma_R^2}{\sigma_G^2}\right)^{12/5} \left(1 + 0.69\sigma_G^{12/5}\right). \tag{C.15}$$

Appendix D

Derivation of PDF models

D.1 Lognormal distribution

The first-order Rytov approximation is used to express the irradiance of a optical wave traveling in atmospheric turbulence as

$$I = \langle I \rangle \exp\left(2\chi_1\right), \tag{D.1}$$

where $\chi_1 = \frac{1}{2}\left(\psi_1 + \psi_1^*\right)$ is the first-order log-amplitude of the the field, and ψ_1 is the first-order phase perturbation term in the Rytov approximation. As the irradiance is normalized in the sense that $\langle I \rangle = 1$, and the log-amplitude χ_1 obeys a Gaussian distribution [90, p. 65], by making the transformation of variables $\chi_1 = \frac{1}{2}\ln I$, the PDF of the irradiance can be obtained as

$$\begin{aligned} f_I(I) =& f_{\chi_1}(\chi_1)\left.\frac{d\chi_1}{dI}\right|_{\chi_1=\frac{1}{2}\ln I} \\ =& \frac{1}{2I\sqrt{2\pi\sigma_{\chi_1}^2}} \exp\left[-\frac{\left(\frac{1}{2}\ln I - \langle\chi_1\rangle\right)^2}{2\sigma_{\chi_1}^2}\right]. \end{aligned} \tag{D.2}$$

Equation (D.2) is a Lognormal distribution, where the variance of χ_1 can be expressed in terms of log-irradiance variance as [See Eq. (52) in Chapter 2]

$$\sigma_{\ln I}^2 = 4\sigma_{\chi_1}^2. \tag{D.3}$$

Next by taking the expected value of Eq. (D.1) yields

$$\langle I \rangle = \langle I \rangle \langle \exp\left(2\chi_1\right) \rangle = \langle I \rangle \exp\left[2\left(\langle\chi_1\rangle + \sigma_{\chi_1}^2\right)\right],$$

where the equality only holds if the argument in the exponential is zero. Thus,

$$\langle\chi_1\rangle = -\sigma_{\chi_1}^2. \tag{D.4}$$

Finally, inserting Eq. (D.3) and Eq. (D.4) into Eq. (D.2) results in

$$f_I(I) = \frac{1}{I\sqrt{2\pi\sigma^2_{\ln I}}} \exp\left[-\frac{\left(\ln I + \frac{1}{2}\sigma^2_{\ln I}\right)^2}{2\sigma^2_{\ln I}}\right], \tag{D.5}$$

where the variance of the log-irradiance $\sigma^2_{\ln I}$ is related to the scintillation index by [See Eq. (53) in Chapter 2]

$$\sigma^2_{\ln I} = \ln\left(\sigma_I^2 + 1\right). \tag{D.6}$$

The cumulative distribution function (CDF) of a random variable (RV) I having the Lognormal distribution is defined by

$$F_I(I) = \frac{1}{2} - \frac{1}{2}\,\mathrm{erf}\left[\frac{\ln I - 0.5\sigma^2_{\ln I}}{\sqrt{2\sigma^2_{\ln I}}}\right].$$

Another method to derive the Lognormal distribution relies on assuming that the travelling optical wave is scattered forward due to the interaction with many on-axis turbulent eddies, along the propagation path. At the receiver plane the intensity pattern is composed by the multiplication of many independent fields scattered by each eddy. Taking the logarithm and invoking the central limit theorem results in the Lognormal distribution. A complete demonstration of this procedure is presented by Wayne [90, Sec. 4.2].

D.2 Negative exponential distribution

Let us assume a circular complex Gaussian RV $U = X_1 + iX_2 = X\exp(-i\varphi)$, where $i^2 = -1$. Considering that X_1 and X_2 are independent zero-mean Gaussian processes with variance σ^2, then, the joint PDF of X and φ can be determined from [108, Eq. (6-72)]

$$f(x,\varphi) = xf(x_1,x_2) = xf(x\cos\varphi, x\sin\varphi) = xf(x\cos\varphi)f(x\sin\varphi), \tag{D.7}$$

where the last equality is due to the independence of X_1 and X_2.

Since,

$$f(x_1,x_2) = \frac{1}{2\pi\sigma^2}e^{-(x_1^2+x_2^2)/2\sigma^2}; \quad x_1^2 + x_2^2 = x^2,$$

Eq. (D.7) yields,

$$f(x,\varphi) = \frac{x}{2\pi\sigma^2}e^{-x^2/2\sigma^2}, \quad x \geq 0, \quad 0 \leq \varphi < 2\pi.$$

Then, the PDFs of X and φ can be determined as the marginal distributions of $f(x,\varphi)$. Thus,

$$f_X(x) = \int_0^{2\pi} f(x,\varphi)d\varphi = \frac{x}{\sigma^2}e^{-x^2/2\sigma^2}, \tag{D.8}$$

easily recognized as a Rayleigh distribution, and,

$$f_\Phi(\varphi) = \int_0^{\infty} f(x,\varphi)dx = \frac{1}{2\pi},$$

is evidently following a uniform distribution in the interval $[0, 2\pi)$.

Now, applying the transformation of variables $I = X^2$, and applying [108, Eq. (5-5)]

$$f_I(I) = f_X(x) \left.\frac{dx}{dI}\right|_{x=\sqrt{I}} = \frac{1}{2\sigma^2} e^{-I/2\sigma^2},$$

and setting $2\sigma^2 = \eta$, yields

$$f_I(I) = \frac{1}{\eta} e^{-I/\eta}, \tag{D.9}$$

where $\eta = E[I]$ is a scale parameter, and $E[\cdot]$ denotes expectation. As the irradiance is normalized in the sense that $\langle I \rangle = 1$, then

$$f_I(I) = e^{-I}, \tag{D.10}$$

which is a negative exponential distribution, with scale parameter equal to unity.

The CDF of a variate I defined by a negative exponential distribution is given by

$$F_I(I) = 1 - e^{-I}.$$

D.3 Gamma distribution

A Gamma random variable I can be derived as the summation of m negative exponential variates as

$$I = \sum_{j=1}^{m} I_j, \tag{D.11}$$

where $I_1, I_2, \ldots, I_m$ are i.i.d. negative exponential variates.

The PDF of the sum of m i.i.d. variates is the convolution of their respective PDFs. Furthermore, if their characteristic functions are given, then characteristic function of the random variable I is

$$\Phi_I(\omega) = \left[\Phi_{I_j}(\omega)\right]^m = \left[\frac{1}{1 - i\omega \langle I_j \rangle}\right]^m, \tag{D.12}$$

where $\Phi_{I_j}(\omega)$ is the characteristic function for a negative exponential variate.

Therefore, the PDF of a Gamma RV can be obtained by applying a inverse Fourier transform [91]

$$f_I(I) = \mathscr{F}^{-1}\left\{\left[\frac{1}{1 - i\omega \langle I_j \rangle}\right]^m\right\} \tag{D.13}$$

$$= \frac{1}{\langle I_j \rangle^m (m-1)!} I^{m-1} e^{-I/\langle I_j \rangle}. \tag{D.14}$$

Now, setting $m = \alpha$, where α is a real valued parameter, using Eq. (B.1.2), and due to independence between all I_j then $\langle I \rangle = \alpha \langle I_j \rangle = 1$, yields

$$f_I(I) = \frac{\alpha(\alpha I)^{\alpha-1}}{\Gamma(\alpha)} \exp\left(-\alpha I\right), \tag{D.15}$$

which is a Gamma probability distribution function; where $\alpha = 1/\sigma_I^2$ is directly related to the scintillation index. The parameter α is associated with the effective number of scatterers along the propagation path [32].

The CDF of a random variable I defined by a Gamma distribution is given by

$$F_I(I) = \frac{1}{\Gamma(\alpha)}\gamma(\alpha, \alpha I),$$

where $\gamma(a, z)$ is the lower incomplete Gamma function defined in Eq. (B.1.3).

D.4 Gamma-Gamma distribution

This heuristic model was developed under the assumption that the resulting irradiance fluctuations are due to a modulation process between the large-scale X and small-scale Y effects over the irradiance [12]

$$I = XY,$$

where X and Y are i.i.d. Gamma random variables. Thus, the probability density functions of X and Y are

$$f_X(x) = \frac{\alpha(\alpha x)^{\alpha-1}}{\Gamma(\alpha)} \exp(-\alpha x),$$

and

$$f_Y(y) = \frac{\beta(\beta y)^{\beta-1}}{\Gamma(\beta)} \exp(-\beta y),$$

respectively. Hence, the conditional PDF of the irradiance is

$$f_I(I|x) = f_Y(y) \left.\frac{dy}{dI}\right|_{y=I/x} = \frac{\beta}{x\Gamma(\beta)} \left(\frac{\beta I}{x}\right)^{\beta-1} \exp(-\beta I/x),$$

where the small-scale Gamma process Y is assumed to be modulated by the large-scale Gamma distributed process X.

The unconditional PDF of irradiance is then found by taking the expectation over the conditional PDF [91]

$$\begin{aligned} f_I(I) &= \int_0^\infty f_I(I|x) f_X(x) dx \\ &= \frac{(\alpha\beta I)^{\beta-1}}{\Gamma(\alpha)\Gamma(\beta) I} \int_0^\infty t^{\alpha-\beta-1} \exp\left(-t + \frac{\alpha\beta I}{t}\right) dt, \end{aligned} \tag{D.16}$$

where the variable transformation $t = \alpha x$ was used. Here, the integral can be related with the Macdonald function, using Eq. (B.2.1), resulting in

$$f_I(I) = \frac{2(\alpha\beta)^{\frac{\alpha+\beta}{2}}}{\Gamma(\alpha)\Gamma(\beta)} I^{\frac{\alpha+\beta}{2}-1} K_{\alpha-\beta}\left(2\sqrt{\alpha\beta I}\right) \tag{D.17}$$

where α and β represent the effective number of large-scale and small-scale eddies, and are related to the scintillation index by [12]

$$\sigma_I^2 = \frac{1}{\alpha} + \frac{1}{\beta} + \frac{1}{\alpha\beta}.$$

The derivation of the GG distribution parameter values can be done through the relationships [12]

$$\begin{aligned}\alpha =& \frac{1}{\sigma_X^2(D)} = \frac{1}{\exp(\sigma_{\ln X}^2(D)) - 1},\\ \beta =& \frac{1}{\sigma_Y^2(D)} = \frac{1}{\exp(\sigma_{\ln Y}^2(D)) - 1}.\end{aligned}$$

The CDF of a variate I having the Gamma-Gamma distribution is defined by [12]

$$\begin{aligned}F_I(I) =& \frac{\pi \csc(\pi(\alpha-\beta))}{\Gamma(\alpha)\Gamma(\beta)} \left[\frac{(\alpha\beta I)^\beta}{\beta\Gamma(\beta-\alpha+1)} {}_1F_2(\beta; \beta+1, \beta-\alpha+1; \alpha\beta I) \right.\\ & \left. - \frac{(\alpha\beta I)^\alpha}{\alpha\Gamma(\alpha-\beta+1)} {}_1F_2(\alpha; \alpha+1, \alpha-\beta+1; \alpha\beta I) \right], \end{aligned} \tag{D.18}$$

where $\csc(x) = 1/\sin(x)$; and ${}_1F_2(\cdot)$ is a generalized hypergeometric function defined in Eq. (B.3.1).

A more compact expression for the CDF can be given in terms of the Meijer's G-function. First, the Macdonald function in Eq. (D.17) is rewritten using Eq. (B.4.2.4), and thus the CDF can be calculated as

$$F_I(I) = \int_0^I f_I(I) dI = \frac{(\alpha\beta)^{\frac{\alpha+\beta}{2}}}{\Gamma(\alpha)\Gamma(\beta)} \int_0^I I^{\frac{\alpha+\beta}{2}-1} G_{0,2}^{2,0}\left[\alpha\beta I \;\middle|\; \begin{matrix} - \\ \frac{\alpha-\beta}{2}, \frac{\beta-\alpha}{2} \end{matrix} \right] dI.$$

Finally, applying Eq. (B.4.3.1), the cumulative distribution function can be given in terms of the Meijer's G-function as

$$F_I(I) = \frac{(\alpha\beta I)^{\frac{\alpha+\beta}{2}}}{\Gamma(\alpha)\Gamma(\beta)} G_{1,3}^{2,1}\left[\alpha\beta I \;\middle|\; \begin{matrix} 1 - \frac{\alpha+\beta}{2} \\ \frac{\alpha-\beta}{2}, \frac{\beta-\alpha}{2}, -\frac{\alpha+\beta}{2} \end{matrix} \right] \tag{D.19}$$

D.5 Weibull distribution

To derive the Weibull distribution a similar approach to that used in Sec. D.2 is followed. Here, applying the transformation of variables $I = X^{2/\beta}$ in Eq. (D.8), where a shape parameter $\beta > 0$ is introduced, yields

$$f_I(I) = f_X(x) \left.\frac{dx}{dI}\right|_{x=I^{\beta/2}} = \frac{\beta}{2\sigma^2} I^{\beta-1} e^{-I^\beta/2\sigma^2},$$

and setting $2\sigma^2 = \eta^\beta$, results in

$$f_I(I) = \frac{\beta}{\eta}\left(\frac{I}{\eta}\right)^{\beta-1} \exp\left[-\left(\frac{I}{\eta}\right)^\beta \right]. \tag{D.20}$$

Equation (D.20) is a Weibull probability distribution function where β and η are the shape and scale parameters, respectively.

The cumulative distribution function can be derived in terms of the PDF as follows

$$F_I(I) = \int_0^I f_I(I)dI = \frac{\beta}{\eta^\beta}\int_0^I I^{\beta-1}\exp\left[-\left(\frac{I}{\eta}\right)^\beta\right]dI,$$

Making the transformation of variables $y = (I/\eta)^\beta$, integrating, and evaluating the limits yields

$$F_I(I) = 1 - \exp\left[-\left(\frac{I}{\eta}\right)^\beta\right]. \tag{D.21}$$

D.5.1 Raw moments

The n-th moment of a RV I following the Weibull distribution is obtained solving

$$\begin{aligned}\langle I^n\rangle &= \int_0^\infty I^n f_I(I)dI \\ &= \frac{\beta}{\eta^\beta}\int_0^\infty I^{n+\beta-1}\exp\left[-\left(\frac{I}{\eta}\right)^\beta\right]dI.\end{aligned}$$

Making the transformation of variables $y = (I/\eta)^\beta$, results in

$$\langle I^n\rangle = \eta^n\int_0^\infty y^{n/\beta}e^y dy,$$

where the integral can be easily related with a gamma function, thus, the n-th irradiance moment of the Weibull distribution is given by

$$\langle I^n\rangle = \eta^n\Gamma\left(1+\frac{n}{\beta}\right). \tag{D.22}$$

D.6 Exponentiated Weibull distribution

Assume a non-linear weighted summation of several mutually independent random variables

$$I^p = \sum_{j=1}^m w_j I_j^p, \tag{D.23}$$

where I_j are Weibull RVs and w_j are weighting factors, such that $\sum w_j = 1$.

Next, in order to approximate such summation to the largest term, but still considering all other terms, the maximum function can be introduced as

$$I = \lim_{p\to\infty}\left[\sum_{j=1}^m w_j I_j^p\right]^{1/p} = \max\{I_1, I_2, \ldots, I_m\}, \tag{D.24}$$

where $I_1, I_2, \ldots, I_m$ are i.i.d. Weibull random variables.

By using the property of ordered statistics for the maximum of a sample the CDF of the irradiance is $F_I(I) = [F_{I_j}(I)]^m$ [100, Eq. (5.3b)], where $F_{I_j}(I)$ is the CDF of the Weibull RVs I_j, and m is an integer number. Then, by setting α as real valued extension of m, the CDF of the RV I yields

$$F_I(I) = \left\{1 - \exp\left[-\left(\frac{I}{\eta}\right)^{\beta}\right]\right\}^{\alpha}. \tag{D.25}$$

Next, by applying standard statistical procedures, the PDF of the RV I is given by

$$f_I(I) = \frac{d}{dI}F_I(I) = \frac{d}{dI}\left\{1 - \exp\left[-\left(\frac{I}{\eta}\right)^{\beta}\right]\right\}^{\alpha},$$

resulting in

$$f_I(I) = \frac{\alpha\beta}{\eta}\left(\frac{I}{\eta}\right)^{\beta-1}\exp\left[-\left(\frac{I}{\eta}\right)^{\beta}\right]\left\{1 - \exp\left[-\left(\frac{I}{\eta}\right)^{\beta}\right]\right\}^{\alpha-1}. \tag{D.26}$$

D.6.1 Raw moments

The n-th moment of a random variable I following the exponentiated Weibull distribution is obtained solving

$$\begin{aligned}\langle I^n\rangle =& \int_0^{\infty} I^n f_I(I)dI \\ =& \frac{\alpha\beta}{\eta^{\beta}}\int_0^{\infty} I^{n+\beta-1}\exp\left[-\left(\frac{I}{\eta}\right)^{\beta}\right]\left\{1 - \exp\left[-\left(\frac{I}{\eta}\right)^{\beta}\right]\right\}^{\alpha-1}dI.\end{aligned} \tag{D.27}$$

Using the Newton's generalized binomial theorem

$$(1+z)^r = \sum_{j=0}^{\infty}\frac{\Gamma(r+1)}{\Gamma(r-j+1)}\frac{z^j}{j!}, \tag{D.28}$$

the last term in Eq. (D.27) can be expanded to yield

$$\langle I^n\rangle = \frac{\alpha\beta}{\eta^{\beta}}\sum_{j=0}^{\infty}\frac{(-1)^j\Gamma(\alpha)}{j!\Gamma(\alpha-j)}\int_0^{\infty} I^{n+\beta-1}\exp\left[-(j+1)\left(\frac{I}{\eta}\right)^{\beta}\right]dI.$$

Making the transformation of variables $y = (j+1)(I/\eta)^{\beta}$, results in

$$\langle I^n\rangle = \alpha\eta^n\sum_{j=0}^{\infty}\frac{(-1)^j\Gamma(\alpha)}{j!(j+1)^{1+n/\beta}\Gamma(\alpha-j)}\int_0^{\infty} y^{n/\beta}e^y dy,$$

where the integral can be easily related with a gamma function using Eq. (B.1.1), thus, the n-th irradiance moment of the exponentiated Weibull distribution has the form

$$\langle I^n \rangle = \alpha \eta^n \Gamma \left(1 + \frac{n}{\beta}\right) g_n(\alpha, \beta). \tag{D.29}$$

where $g_n(\alpha, \beta)$ was introduced to simplify the notation, and is defined by

$$g_n(\alpha, \beta) = \sum_{j=0}^{\infty} \frac{(-1)^j \Gamma(\alpha)}{j!(j+1)^{1+n/\beta}\Gamma(\alpha - j)}. \tag{D.30}$$

References

[1] Y. Arimoto, "Near field laser transmission with bidirectional beacon tracking for Tbps class wireless communications," in *Free-Space Laser Communication Technologies XXII*, ser. Proc. SPIE, H. Hemmati, Ed., vol. 7587, 2010, p. 758708.

[2] E. Ciaramella, Y. Arimoto, G. Contestabile, M. Presi, A. D'Errico, E. Guarino, and M. Matsumoto, "1.28 Terabit/s (32x40 Gbit/s) WDM transmission system for free space optical communications," *IEEE J. Sel. Area Comm.*, vol. 27, pp. 1639–1645, 2009.

[3] R. M. Sova, J. E. Sluz, D. W. Young, J. C. Juarez, A. Dwivedi, I. N. M. Demidovich, J. E. Graves, M. Northcott, J. Douglass, J. Phillips, D. Driver, A. McClarin, and D. Abelson, "80 Gb/s free-space optical communication demonstration between an aerostat and a ground station," in *Free-Space Laser Communications VI*, ser. Proc. SPIE, A. K. Majumdar and C. C. Davis, Eds., vol. 6304, 2006, p. 630414.

[4] G. Fletcher, T. Hicks, and B. Laurent, "The SILEX optical interorbit link experiment," *J. Electron. Comm. Eng.*, vol. 3, no. 6, pp. 273–279, 1991.

[5] M. Toyoda, M. Toyoshima, T. Takahashi, M. Shikatani, Y. Arimoto, K. Araki, and T. Aruga, "Ground to ETS-VI narrow laser beam transmission," ser. Proc. SPIE, vol. 2699, 1996, pp. 71–80.

[6] M. Jeganathan, M. Toyoshima, K. . Wilson, J. James, G. Xu, and J. Lesh, "Data analysis results from the GOLD experiments," in *Free-Space Laser Comm. Tech. IX*, ser. Proc. SPIE, vol. 1990, 1997, pp. 70–81.

[7] M. Toyoshima, Y. Takayama, T. Takahashi, K. Suzuki, S. Kimura, K. Takizawa, T. Kuri, W. K. M. Toyoda, and H. Kunimori, "Ground-to-satellite laser communication experiments," *EEE Aerosp. Electron. Syst. Mag.*, vol. 23, no. 8, pp. 10–18, 2008.

[8] N. Perlot, M. Knapek, D. Giggenbach, J. Horwath, M. Brechtelsbauer, Y. Takayama, and T. Jono, "Results of the optical downlink experiment KIODO from OICETS satellite to optical ground station Oberpfaffenhofen (OGS-OP)," in *Free-Space Laser Communication Technologies XIX and Atmospheric Propagation of Electromagnetic Waves*, ser. Proc. SPIE, O. Korotkova and S. Mecherle, Eds., vol. 6457, 2007, p. 645704.

[9] V. I. Tatarski, *The effects of the turbulent atmosphere on wave propagation*. Israel Program for Scientific Translation, 1971.

[10] P. Beckmann, *Probability in Communication Engineering*. Harcourt, Brace & World, 1967.

[11] J. H. Churnside and R. J. Hill, "Probability density of irradiance scintillations for strong path-integrated refractive turbulence," *J. Opt. Soc. Am. A*, vol. 4, no. 4, pp. 727–737, 1987.

[12] M. A. Al-Habash, L. C. Andrews, and R. L. Phillips, "Mathematical model for the irradiance probability density function of a laser beam propagating through turbulent media," *Opt. Eng.*, vol. 40, no. 8, pp. 1554–1562, 2001.

[13] E. Jakeman and P. Pusey, "Significance of K distributions in scattering experiments," *Phys. Rev. Lett.*, vol. 40, pp. 546–550, 1978.

[14] D. T. Wayne, R. L. Philips, and L. C. Andrews, "Comparing the log-normal and gamma-gamma model to experimental probability density functions of aperture averaging data," in *Free-Space Laser Communications X*, ser. Proc. SPIE, C. Majumdar, A. K.and Davis, Ed., vol. 7814, 2010, p. 78140K.

[15] S. Doss-Hammel, E. Oh, J. Ricklin, F. Eaton, C. Gilbreath, and D. Tsintikidis, "A comparison of optical turbulence models," in *Remote Sensing and Modeling of Ecosystems for Sustainability*, ser. Proc. SPIE, J. C. Ricklin and D. G. Voelz, Eds., vol. 5550, 2004, pp. 236–246.

[16] J. C. Ricklin, S. M. Hammel, F. D. Eaton, and S. L. Lachinova, "Atmospheric channel effects on free-space laser communication," *J. Opt. Fiber. Commun. Rep.*, vol. 3, pp. 111–158, 2006.

[17] L. C. Andrews, M. A. Al-Habash, C. Y. Hopen, and R. L. Phillips, "Theory of optical scintillation: Gaussian-beam wave model," *Waves in Random and Complex Media*, vol. 11, no. 3, pp. 271–291, 2001.

[18] E. Korevaar, I. I. Kim, and B. McArthur, "Atmospheric propagation characteristics of highest importance to commercial free space optics," in *Atmospheric Propagation*, ser. Proc. SPIE, C. Y. Young and J. S. Stryjewski, Eds., vol. 4976, 2003, pp. 1–12.

[19] A. K. Majundar and J. C. Ricklin, "Effects of the atmospheric channel on free-space optical communication," in *Free-Space Laser Communications V*, ser. Proc. SPIE, D. G. Voelz and J. C. Ricklin, Eds., vol. 5892, 2005, pp. 149–164.

[20] D. L. Fried, "Aperture averaging of scintillation," *J. Opt. Soc. Am.*, vol. 57, no. 2, pp. 169–175, 1967.

[21] G. E. Homstad, J. W. Strohbehn, R. H. Berger, and J. M. Heneghan, "Aperture-averaging effects for weak scintillations," *J. Opt. Soc. Am.*, vol. 64, no. 2, pp. 162–165, 1974.

[22] R. J. Hill, "Theory of saturation of optical scintillation by strong turbulence: plane-wave variance and covariance and spherical-wave covariance," *J. Opt. Soc. Am.*, vol. 72, no. 2, pp. 212–222, 1982.

[23] J. H. Churnside, "Aperture averaging of optical scintillations in the turbulent atmosphere," *Appl. Opt.*, vol. 30, pp. 1982–1994, 1991.

[24] L. C. Andrews, "Aperture-averaging factor for optical scintillations of plane and spherical waves in the atmosphere," *J. Opt. Soc. Am.*, vol. 9, no. 4, pp. 597–600, 1992.

[25] J. C. Ricklin and F. M. Davidson, "Atmospheric turbulence effects on a partially coherent gaussian beam: implications for free-space laser communication," *J. Opt. Soc. Am. A*, vol. 19, no. 9, pp. 1794–1802, 2002.

[26] W. B. Miller, J. C. Ricklin, and L. Andrews, "Log-amplitudevariance and wave structure function - a new perspective for gaussian beams," *J. Opt. Soc. Am. A*, vol. 10, no. 4, pp. 661–672, 1993.

[27] J. C. Ricklin and F. M. Davidson, "Atmospheric optical communication with a gaussian schell beam," *J. Opt. Soc. Am. A*, vol. 20, no. 5, pp. 856–866, 2003.

[28] A. Weeks, J. Xu, R. Phillips, L. Andrews, C. Stickley, G. Sellar, J. Stryjewsky, and J. Harvey, "Experimental verification for an eight-element multiple-aperture equal-gain coherent laser receiver for laser communications," *Appl. Opt.*, vol. 37, no. 21, pp. 4782–4788, 1998.

[29] B. Levine, E. Martinsen, A. Wirth, A. Jankevics, M. Toledo-Quinones, F. Landers, and T. Bruno, "Horizontal line-of-sight turbulence over near-ground paths and implications for adaptive optics corrections in laser communications," *Appl. Opt.*, vol. 37, no. 21, pp. 4782–4788, 1998.

[30] R. K. Tyson, "Bit-error rate for free-space adaptive optics laser communications," *J. Opt. Soc. Am. A*, vol. 19, no. 4, pp. 753–758, 2002.

[31] T. Weyrauch and M. A. Vorontsov, "Free-space laser communications with adaptive optics: Atmospheric compensation experiments," *J. Opt. Fiber. Commun. Rep.*, vol. 1, pp. 355–379, 2004.

[32] L. C. Andrews and R. L. Philips, *Laser Beam Propagation through Random Media*, 2nd ed. Belligham: SPIE Press, 2005.

[33] R. S. Lawrence, G. R. Ochs, and S. F. Clifford, "Measurements of atmospheric turbulence relevant to optical propagation," *J. Opt. Soc. Am.*, vol. 60, no. 6, pp. 826–830, 1970.

[34] E. L. Andreas, "Estimating C_n^2 over snow and sea ice from meteorological data," *J. Opt. Soc. Am. A*, vol. 5, no. 4, pp. 481–495, 1988.

[35] D. Sadot and N. S. Kopeika, "Forecasting optical turbulence strength on the basis of macroscale meteorology and aerosols: models and validation," *Opt. Eng.*, vol. 31, no. 31, pp. 200–212, 1992.

[36] T. Wang, G. R. Ochs, and S. F. Clifford, "A saturation-resistant optical scintillometer to measure C_n^2," *J. Opt. Soc. Am.*, vol. 68, no. 3, pp. 334–338, 1978.

[37] Y. Yitzhaky, I. Dror, and N. S. Kopeika, "Restoration of atmospherically blurred images according to weather-predicted atmospheric modulation transfer functions," *Opt. Eng.*, vol. 36, no. 11, pp. 3064–3072, 1997.

[38] A. N. Kolmogorov, "The local structure of turbulence in a incompressible viscous fluid for very large reynolds numbers," *C. R. (Doki) Acad. Sci. U.S.R.R.*, vol. 30, pp. 301–305, 1941.

[39] A. Ishimaru, "Fluctuations of a focused beam wave for atmospheric turbulence probing," *Proc. IEEE*, vol. 57, pp. 407–414, 1969.

[40] H. T. Yura, C. C. Sung, S. F. Clifford, and R. J. Hill, "Second-order Rytov approximation," *J. Opt. Soc. Am.*, vol. 73, no. 4, pp. 500–502, 1983.

[41] F. Dios, J. Recolons, A. Rodríguez, and O. Batet, "Temporal analysis of laser beam propagation in the atmosphere using computer-generated long phase screens," *Opt. Express*, vol. 16, no. 3, pp. 2206–2220, 2008.

[42] R. L. Fante, "Electromagnetic beam propagation in turbulent media: an update," *Proc. IEEE*, vol. 68, no. 11, pp. 1424–1443, 1980.

[43] J. Recolons, L. Andrews, and R. L. Philips, "Analysis of beam wander effects for a horizontal-path propagating gaussian-beam wave: focused beam case," *Opt. Eng.*, vol. 46, no. 8, p. 086002, 2007.

[44] J. H. Churnside and R. J. Lataitis, "Wander of an optical beam in the turbulent atmosphere," *Appl. Opt.*, vol. 29, no. 7, pp. 926–930, 1990.

[45] G. R. Ochs and R. J. Hill, "Optical-scintillation method of measuring turbulence inner scale," *Appl. Opt.*, vol. 24, no. 15, pp. 2430–2432, 1985.

[46] J. A. Fleck, J. R. Morris, and M. D. Feit, "Time-dependent propagation of high-energy laser beams through the atmosphere," *Appl. Phys.*, vol. 10, pp. 129–160, 1976.

[47] J. M. Martin and S. M. Flattè, "Intensity images and statistics from numerical simulation of wave propagation in 3-D random media," *J. Opt. Soc. Am.*, vol. 27, no. 11, pp. 2111–2126, 1998.

[48] R. Frehlich, "Simulation of laser propagation in a turbulent atmosphere," *J. Opt. Soc. Am.*, vol. 39, no. 3, pp. 393–397, 2000.

[49] J. Recolons and F. Dios, "Accurate calculation of phase screens for the modeling of laser beam propagation through atmospheric turbulence," in *Atmospheric Optical Modeling, Measurement, and Simulation*, ser. Proc. SPIE, S. M. Doss-Hammel and A. Kohnle, Eds., vol. 5891, 2005, pp. 51–62.

[50] R. G. Lane, A. Glindemann, and J. C. Dainty, "Simulation of a kolmogorov phase screen," *Waves Random Media*, vol. 2, pp. 209–224, 1992.

[51] C. M. Harding, R. A. Johnston, and R. G. Lane, "Fast simulation of a Kolmogorov phase screen," *Appl. Opt.*, vol. 38, no. 11, pp. 2161–2160, 1999.

[52] R. D. Hudson, *Infrared System Engineering*. New York: John Wiley & Sons, 1969.

[53] I. I. Kim, R. Stieger, J. A. Koontz, C. Moursund, M. Barclay, M. Adhikari, J. Schuster, E. Korevaar, R. Ruigrok, and C. DeCusatis, "Wireless optical transmission of fast ethernet, FDDI, ATM, and ESCON protocol data using the TerraLink laser communication system," *Opt. Eng.*, vol. 37, no. 12, pp. 3143–3155, 1998.

[54] E. E. Bell, L. Eisner, and J. O. R. A. Young, "Spectral radiance of sky and terrain at wavelengths between 1 and 20 microns. II. Sky measurements," *J. Opt. Soc. Am.*, vol. 50, no. 12, pp. 1313–1320, 1960.

[55] G. L. Knestrick and J. A. Curcio, "Measurements of spectral radiance of the horizon sky," *Appl. Opt.*, vol. 6, no. 12, pp. 2105–2109, 1967.

[56] R. E. Bird and C. Riordan, "Simple solar spectral model for direct and diffuse irradiance on horizontal and tilted plans at the earths surface for cloudless atmosphere," *J. Clim. Meteor.*, vol. 25, pp. 87–97, 1986.

[57] J. H. Churnside and R. G. Frehlich, "Experimental evaluation of log-normally modulated rician and IK models of optical scintillation in the atmosphere," *J. Opt. Soc. Am. A*, vol. 6, no. 11, pp. 1760–1766, 1989.

[58] F. S. Vetelino, C. Young, and L. Andrews, "Fade statistics and aperture averaging for Gaussian beam waves in moderate-to-strong turbulence," *Appl. Opt.*, vol. 46, no. 18, pp. 3780–3790, 2007.

[59] B. Epple, "Simplified channel model for simulation of free-space optical communications," *J. Opt. Commun. Netw.*, vol. 2, no. 5, pp. 293–304, 2010.

[60] N. Perlot and D. Fritzsche, "Aperture-averaging – theory and measurements," in *Free-Space Laser Communication Technologies XVI*, ser. Proc. SPIE, G. Mecherle, C. Y. Young, and J. S. Stryjewski, Eds., vol. 5338, 2004, pp. 233–242.

[61] J. Barry, *Wirelees Infrarred Communications*. Norwell: Kluwer Academic Publishers, 1994.

[62] K. K. Wong, T. O. R, and M. Kiatweerasakul, "The performance of optical wireless ook, 2-ppm and spread spectrum under the effects of multipath dispersion and artificial light interference," *Int. J. Commun. Syst.*, vol. 13, pp. 551–576, 2000.

[63] V. Chan, "Coding for the turbulent atmospheric optical channel," *IEEE Trans. Commun.*, vol. 30, no. 1, pp. 269–275, 1982.

[64] D. Shiu and J. M. Kahn, "Differential pulse-position modulation for power-efficient optical communication," *IEEE Trans. Commun.*, vol. 47, no. 8, pp. 1201–1211, 1999.

[65] S. Patarasen and C. N. Georghlades, "Frame synchronization for optical overlapping pulse-position modulation systems," *IEEE Trans. Commun.*, vol. 40, no. 4, pp. 783–794, 1992.

[66] R. Perez-Jimenez, J. Rabadan, V. Melian, and M. Betancor, "Improved PPM modulations for high spectral efficiency IR-WLAN," in *Personal, Indoor and Mobile Radio Communications, 1996. PIMRC'96., Seventh IEEE International Symposium on*, vol. 1, 1996, pp. 262–266.

[67] H. Sigiyama and K. Nosu, "MPPM: A method for improving the band-utilization efficiency in optical PPM," *IEEE J. Lightw. Technol.*, vol. 7, no. 3, pp. 465–472, 1989.

[68] C. N. Georghiades and D. L. Snyder, "Locating data frames in direct-detection optical communication systems," *IEEE Trans. Commun.*, vol. COM-32, no. 2, pp. 118–123, 1984.

[69] M. Srinivasan, V. Vilnrotter, and C. Lee, "Decision-directed slot synchronization for pulse-position-modulated optical signals," Jet Propulsion Laboratory, Pasadena, California, The Interplanetary Network Progress Report 42-161, May 15 2005.

[70] X. Sun and F. M. Davidson, "Word timing recovery in direct detection optical ppm communication systems with avalanche photodiodes using a phase lock loop," *IEEE Trans. Commun.*, vol. 38, no. 5, pp. 666–673, 1990.

[71] R. Otte, L. P. de Jong, and A. H. M. van Roermund, "Slot synchronization by reducing the ppm pulsewidth in wireless optical systems," *IEEE Trans. Circuits Syst. II, Exp. Briefs*, vol. 45, no. 7, pp. 901–903, 1998.

[72] A. Okazaki, "Pulse interval modulation applicable to narrow band transmission," *IEEE. Trans. Cable Television*, vol. CATV-3, no. 4, pp. 155–164, 1978.

[73] P. P. Webb, R. J. McIntyre, and J. Conradi, "Properties of avalanche photodiodes," *RCA review*, vol. 35, pp. 234–278, 1974.

[74] F. M. Davidson and X. Sun, "Gaussian approximation versus nearly exact performance analysis of optical communication systems with PPM signaling and APD receivers," *IEEE Trans. Commun.*, vol. 36, no. 11, pp. 1185–1192, 1988.

[75] J. C. Ricklin, S. Bucaille, and F. M. Davidson, "Performance loss factors for optical communication through clear air turbulence," in *Free-Space Laser Communications and Active Laser Illumination III*, ser. Proc. SPIE, D. G. Voelz and J. C. Ricklin, Eds., vol. 5160, 2004, pp. 1–12.

[76] S. J. Dolinar, J. Hamkins, B. E. Moision, and V. A. Vilnrotter, *Deep Space Optical Communications*. Wiley-Interscience, 2006, ch. Optical Modulation and Coding, pp. 215–299.

[77] A. J. C. Moreira, R. T. Valdas, and A. M. de Oliveira Duarte, "Performance of infrared transmission systems under ambient light interference," *IEEE Proc. Optoelectron.*, vol. 143, no. 6, pp. 339–346, 1996.

[78] J. G. Proakis, *Digital Communications*, 4th, Ed. Boston: McGraw-Hill, 2001.

[79] L. C. Andrews and R. L. Phillips, "*I–K* distribution as a universal propagation model of laser beams in atmospheric turbulence," *J. Opt. Soc. Am. A*, vol. 2, pp. 160–163, 1985.

[80] R. Barrios and F. Dios, "Exponentiated Weibull distribution family under aperture averaging for Gaussian beam waves," *Opt. Express*, vol. 20, no. 12, pp. 13 055–13 064, 2012.

[81] G. Mudholkar and D. Srivastava, "Exponentiated Weibull family for analyzing bathtub failure-rate data," *IEEE Trans. Reliab.*, vol. 42, no. 2, pp. 299–302, 1993.

[82] W. Weibull, "A statistical distribution function of wide applicability," *J. Appl. Mech.-Trans. ASME*, vol. 18, no. 3, p. 293297, 1951.

[83] J. V. Seguro and T. W. Lambert, "Modern estimation of the parameters of the Weibull wind speed distribution for wind energy analysis," *J Wind. Eng. Ind. Aerod.*, vol. 85, no. 1, pp. 75–84, 2000.

[84] Z. Fang, B. R. Patterson, and M. E. T. Jr., "Modeling particle size distributions by the Weibull distribution function," *Mater. Charact.*, vol. 31, no. 3, pp. 177–182, 1993.

[85] D. Schleher, "Radar detection in Weibull clutter," *IEEE Trans. Aerosp. Electron. Syst.*, vol. AES-12, no. 6, pp. 736–743, nov. 1976.

[86] M.-S. Alouini and M. Simon, "Performance of generalized selection combining over Weibull fading channels," in *Vehicular Technology Conference, 2001. VTC 2001 Fall. IEEE VTS 54th*, vol. 3, 2001, pp. 1735 –1739.

[87] M. Lupupa and M. Dlodlo, "Performance of MIMO system in Weibull fading channel - Channel capacity analysis," in *EUROCON 2009, EUROCON '09. IEEE*, may 2009, pp. 1735 –1740.

[88] N. C. Sagias, D. A. Zogas, G. K. Karagiannidis, and G. S. Tombras, "Channel capacity and second-order statistics in Weibull fading," *IEEE Commun. Lett.*, vol. 8, no. 6, pp. 377–379, 2004.

[89] N. Chatzidiamantis, H. Sandalidis, G. Karagiannidis, S. Kotsopoulos, and M. Matthaiou, "New results on turbulence modeling for free-space optical systems," in *Telecommunications (ICT), 2010 IEEE 17th International Conference on*, april 2010, pp. 487–492.

[90] D. T. Wayne, "The PDF of irradiance for a free-space optical communications channel: A physics based model," Ph.D. dissertation, School of Electrical Engineering and Computer Science, College of Engineering and Computer Science, University of Central Florida, 2010.

[91] F. Vetelino, "Fade statistics for a lasercom system and the joint PDF of a Gamma-Gamma distributed irradiance and its time derivative," Ph.D. Dissertation, Department of Mathematics, University of Central Florida, 2006.

[92] A. D. Wheelon, "Skewed distribution of irradiance predicted by the second-order Rytov approximation," *J. Opt. Soc. Am. A*, vol. 18, no. 11, pp. 2783–2798, 2001.

[93] S. M. Flatté, C. Bracher, and G.-Y. Wang, "Probability-density functions of irradiance for waves in atmospheric turbulence calculated by numerical simulation," *J. Opt. Soc. Am. A*, vol. 11, no. 7, pp. 2082–2092, 1994.

[94] F. S. Vetelino, C. Young, L. C. Andrews, and J. Recolons, "Aperture averaging effects on the probability density of irradiance fluctuations in moderate-to-strong turbulence," *Appl. Opt.*, vol. 46, pp. 2099–2108, 2007.

[95] S. Michael, R. R. Parenti, F. G. Walther, A. M. Volpicelli, J. D. Moores, W. Wilcox, Jr., and R. Murphy, "Comparison of scintillation measurements from a 5 km communication link to standard statistical models," in *Atmospheric Propagation VI*, ser. Proc. SPIE, L. M. W. Thomas and G. C. Gilbreath, Eds., vol. 7324, 2009, p. 73240J.

[96] M. D. Yacoub, "The α–μ distribution: a physical fading model for the Stacy distribution," *IEEE Trans. Veh. Technol.*, vol. 56, no. 1, pp. 27–34, 2007.

[97] A. Abdi, W. C. Lau, M.-S. Alouini, and M. Kaveh, "A new simple model for land mobile satellite channels: first- and second-order statistics," *IEEE Trans. Wireless Commun.*, vol. 2, no. 3, pp. 519–528, 2003.

[98] A. Jurado-Navas, J. M. Garrido-Balsells, J. F. Paris, and A. Puerta-Notario, *Numerical Simulations of Physical and Engineering Processes*. Intech, September 2011, ch. A Unifying Statistical Model for Atmospheric Optical Scintillation, pp. 181–206.

[99] R. R. Parenti and R. J. Sasiela, "Distribution models for optical scintillation due to atmospheric turbulence," Lincoln Laboratory, Massachusetts Institute of Technology, Tech. Rep. TR-1108, December 12 2005. [Online]. Available: http://handle.dtic.mil/100.2/ADA441284

[100] H. Rinne, *The Weibull distribution—A handbook*. CRC Press, 2009.

[101] S. Nadarajah and A. K. Gupta, "On the moments of the exponentiated Weibull distribution," *Communications in Statistics—Theory and Methods*, vol. 34, no. 2, pp. 253–256, 2005.

[102] R. Barrios, F. Dios, J. Recolons, and A. Rodríguez, "Aperture averaging in a laser gaussian beam: simulations and experiments," in *Free-Space Laser Communications X*, ser. Proc. SPIE, C. Majumdar, A. K.and Davis, Ed., vol. 7814, 2010, p. 78140C.

[103] K. Levenberg, "A method for the solution of certain problems in least squares," *Quart. Appl. Math.*, vol. 2, pp. 164–168, 1944.

[104] D. Marquardt, "An algorithm for least-squares estimation of nonlinear parameters," *SIAM J. Appl. Math.*, vol. 11, pp. 431–441, 1963.

[105] R. Barrios and F. Dios, "Probability of fade and BER performance of FSO links over the exponentiated Weibull fading channel under aperture averaging," in *Unmanned/Unattended Sensors and Sensor Networks IX*, ser. Proc. SPIE, vol. 8540, 2012, p. 85400D.

[106] S. D. Lyke, D. G. Voelz, and M. C. Roggemann, "Probability density of aperture-averaged irradiance fluctuations for long range free space optical communication links," *Appl. Opt.*, vol. 48, no. 33, pp. 6511–6527, 2009.

[107] A. Belmonte, "Feasibility study for the simulation of beam propagation: consideration of coherent lidar performance," *Appl. Opt.*, vol. 39, no. 30, pp. 5426–5445, 2000.

[108] A. Papoulis, *Probability, Random Variables, and Sthocastic Processes*, 3rd ed. McGraw-Hill, 1991.

[109] A. A. Farid and S. Hranilovic, "Outage capacity optimization for free-space optical links with pointing errors," *J. Lightwave Technol.*, vol. 25, no. 7, pp. 1702–1710, 2007.

[110] J. Ma, Y. Jiang, S. Yu, L. Tan, and W. Du, "Packet error rate analysis of OOK, DPIM and PPM modulation schemes for ground-to-satellite optical communications," *Opt. Commun.*, vol. 283, pp. 237–242, 2010.

[111] H. G. Sandalidis, T. A. Tsiftsis, and G. K. Karagiannidis, "Optical wireless communications with heterodyne detection over turbulence channels with pointing errors," *J. Lightwave Technol.*, vol. 27, no. 20, pp. 4440–4445, 2009.

[112] J. M. Garrido-Balsells, A. Jurado-Navas, J. F. Paris, M. Castillo-Vázquez, and A. Puerta-Notario, "Closed-form BER analysis of variable weight MPPM coding under gamma-gamma scintillation for atmospheric optical communications," *Opt. Lett.*, vol. 37, no. 4, pp. 719–721, 2012.

[113] M. Uysal, J. T. Li, and M. Yu, "Error rate performance analysis of coded free-space optical links over gamma-gamma atmospheric turbulence channels," *IEEE Trans. Wireless Commun.*, vol. 5, pp. 1229–1233, 2006.

[114] H. Wu, H. Yan, and X. Li, "Performance analysis of bit error rate for free space optical communication with tip-tilt compensation based on gammagamma distribution," *Opt. Appl.*, vol. XXXIX, no. 3, pp. 533–545, 2009.

[115] X. Zhu and J. M. Kahn, "Free-space optical communication through atmospheric turbulence channels," *IEEE Trans. Commun.*, vol. 50, no. 8, pp. 1293–1300, 2002.

[116] H. Moradi, M. Falahpour, H. H. Refai, P. G. LoPresti, and M. Atiquzzaman, "BER analysis of optical wireless signals through lognormal fading channels with perfect CSI," in *Telecommunications (ICT), 2010 IEEE 17th International Conference on*, 2010, pp. 493–497.

[117] F. Johansson, *mpmath: a Python library for arbitrary-precision floating-point arithmetic (version 0.17)*, February 2011, http://code.google.com/p/mpmath/. [Online]. Available: http://code.google.com/p/mpmath/

[118] A. Dang, "A closed-form solution of the bit-error rate for optical wireless communication systems over atmospheric turbulence channels," *Opt. Express*, vol. 19, pp. 3494–3502, 2011.

[119] X. Yi, Z. Liu, and P. Yue, "Average BER of free-space optical systems in turbulent atmosphere with exponentiated Weibull distribution," *Opt. Lett.*, vol. 37, no. 24, pp. 5142–5144, 2012.

[120] H. G. Sandalidis, T. A. Tsiftsis, G. K. Karagiannidis, and M. Uysal, "BER Performance of FSO links over strong atmospheric turbulence channels with pointing errors," *IEEE Commun. Lett.*, vol. 12, no. 1, pp. 44–46, 2008.

[121] W. Gappmair, S. Hranilovic, and E. Leitgeb, "Performance of PPM on terrestrial FSO links with turbulence and pointing errors," *IEEE Commun. Lett.*, vol. 14, no. 5, 2010.

[122] A. Jurado-Navas, J. M. Garrido-Balsells, J. F. Paris, M. Castillo-Vázquez, and A. Puerta-Notario, "Impact of pointing errors on the performance of generalized atmospheric optical channels," *Opt. Express*, vol. 20, no. 11, 2012.

[123] R. Barrios and F. Dios, *Optical Communications Systems*. InTech, 2011, ch. Wireless Optical Communications Through the Turbulent Atmosphere: A Review.

[124] L. C. Andrews, R. L. Philips, and C. Y. Hopen, *Laser Beam Scintillation with Applications*. Belligham: SPIE Press, July 2001.

[125] K. Kiasaleh, "On the probability density function of signal intensity in free-space optical communications systems impaired by pointing jitter and turbulence," *Opt. Eng.*, vol. 33, no. 11, pp. 3748–3757, 1994.

[126] L. C. Andrews, W. B. Miller, and J. C. Ricklin, "Spatial coherence of a Gaussian-beam wave in weak and strong optical turbulence," *J. Opt. Soc. Am. A*, vol. 11, no. 5, pp. 1653–1660, 1994.

[127] O. Korotkova, L. C. Andrews, and R. L. Phillips, "Model for a partially coherent gaussian beam in atmospheric turbulence with application in lasercom," *Opt. E*, vol. 43, no. 2, pp. 330–341, 2004.

[128] G. P. Berman, A. R. Bishop, B. M. Chernobrod, D. C. Nguyen, and V. N. Gorshkov, "Suppression of intensity fluctuations in free space high-speed optical communication based on spectral encoding of a partially coherent beam," *Opt. Commun.*, vol. 280, pp. 264–270, 2007.

[129] C. Chen, H. Yang, X. Feng, and H. Wang, "Optimization criterion for initial coherence degree of lasers in free-space optical links through atmospheric turbulence," *Opt. Lett.*, vol. 34, no. 4, pp. 419–421, 2009.

[130] D. K. Borah and D. G. Voelz, "Spatially partially coherent beam parameter optimization for free space optical communications," *Opt. Express*, vol. 18, no. 20, pp. 20 746–20 758, 2010.

[131] J. Cang and X. Liu, "Average capacity of free-space optical systems for a partially coherent beam propagating through non-Kolmogorov turbulence," *Opt. Lett.*, vol. 36, no. 17, pp. 3335–3337, 2011.

[132] X. Xiao and D. Voelz, "On-axis probability density function and fade behavior of partially coherent beams propagating through turbulence," *Appl. Opt.*, vol. 48, no. 2, pp. 167–175, 2009.

[133] L. Mandel and E.Wolf, *Optical Coherence and Quantum*. Cambridge: Cambridge Univesity Press, 1995.

[134] D. G. Voelz and X. Xiao, "A brief review of spatially partially coherent beams for FSO communications," in *Atmospheric Propagation of Electromagnetic Waves III*, ser. Proc. SPIE, O. Korotkova, Ed., vol. 7200, 2009, p. 72000C.

[135] K. Drexler, M. Roggemann, and D. Voelz, "Use of a partially coherent transmitter beam to improve the statistics of received power in a free-space optical communication system: theory and experimental results," *Opt. Eng.*, vol. 50, no. 2, p. 025002, 2011.

[136] X. Xiao and D. Voelz, "Wave optics simulation of partially coherent beams," in *Free-Space Laser Communications V*, ser. Proc. SPIE, D. G. Voelz and J. C. Ricklin, Eds., vol. 5892, 2005, p. 58920Q.

[137] ——, "Wave optics simulation approach for partial spatially coherent beams," *Opt. Express*, vol. 14, no. 16, pp. 6986–6992, 2006.

[138] ——, "Toward optimizing partial spatially coherent beams for free space laser communications," in *Free-Space Laser Communications VII*, ser. Proc. SPIE, A. K. Majumdar and C. C. Davis, Eds., vol. 6709, 2007, p. 67090P.

[139] Q. Xian-Mei, Z. Wen-Yue, W. An-Ting, G. Chun, and R. Rui-Zhong, "Numerical simulation for coherent and partially coherent beam propagation through atmospheric turbulence," *Chin. Phys. Lett.*, vol. 27, no. 4, p. 044214, 2010.

[140] R. J. Hill, R. G. Frehlich, and W. D. Otto, "The probability distribution of irradiance scintillation," National Oceanic and Atmospheric Administration (NOAA), Boulder, Colorado, Tech. Rep. ETL-270, January 1997.

[141] E. Jones, T. Oliphant, and P. Peterson, "SciPy: Open source scientific tools for Python," 2001–. [Online]. Available: http://www.scipy.org/

[142] J. D. Hunter, "Matplotlib: A 2D graphics environment," *Comput. Sci. Eng.*, vol. 9, no. 3, pp. 90–95, 2007.

[143] I. Gradshteyn and I. Ryzhik, *Table of Integrals, Series, and Products*, 7th ed., A. Jeffrey and D. Zwillinger, Eds. New York: Academic Press, 2007.

[144] L. C. Andrews, *Special Functions for Engineers and Applied Mathematicians*. Macmillan Publishing Company, 1985.

[145] The Wolfram functions site. On-line. Wolfram Research. [Online]. Available: http://functions.wolfram.com

[146] V. S. Adamchik and I. O. Marichev, "The algorithm for calculating integrals of hypergeometric type functions and its realization in REDUCE system," in *Proceedings of the 1990 International Symposium on Symbolic and Algebraic Computation*. ACM, Academic Press, 1990, pp. 212–224.

[147] A. P. Prudnikov, U. A. Brychkov, and O. I. Marichev, *Integrals and Series*. Gordon and Breach Science Publishers, 1990, vol. 3: More Special Functions.